June 17, 2024

Design of an experiment to search for neutron oscillations at the European Spallation Source

Linus B. Persson

European Spallation Source

Division of Particle and Nuclear Physics, Department of Physics, Lund University

Supervised by Valentina Santoro
Co-supervised by Matthias Holl and Blahoslav Rataj

Thesis submitted for the degree of Master of Science in Physics

FYSM63, 60 hp (8 months full-time equivalent)

Abstract

This work is aimed at presenting a design for the proposed HIBEAM beamline which seeks to perform neutron oscillation measurements at the European Spallation Source (ESS). The design is informed by beamline simulations performed with PHITS 3.33 and detector simulations performed with both PHITS and Geant4 11.2. The shielding, consisting of 45 cm of steel and 85 cm of heavy concrete at its thickest point, is designed to satisfy the ESS dose rate requirement of 1.5 µSv/h. This work has also demonstrated the applicability of multivariate kernel density estimation for neutron beamline simulations, showing better reproduction of the neutron energy spectrum in the beamline than the source term methodology previously employed at ESS. This work further provides estimates of the spallation background for the HIBEAM detector systems. It illustrates how the addition of LiF cladding to the vacuum pipe reduces the electron background in the time projection chamber by two orders of magnitude, making the background levels manageable for the experiment to proceed.

Publication note

The results from the beam stop simulations in this thesis have been reviewed and approved as report ESS-5286512 [1]. An abbreviated version of the HIBEAM beamline and background simulations have been made public in the arXiv paper listed as Ref. [2]. Publications on the beamline simulation methodology as well as PHITS/Geant4 benchmarking, based partly on this thesis, are under consideration.

Popular abstract

Ordinary matter mainly consists of protons, neutrons and electrons. By colliding particles with each other at high energies, you can also create antiprotons, antineutrons and positrons. These so-called antiparticles have the same properties as their normal counterparts but with the opposite electrical charge. Since the universe treats particles and antiparticles in a similar way, one might ask why there is more matter than antimatter in the Universe. At the time of writing, science has no clear answer to this question. For some reason, the Universe has developed a preference for matter over antimatter, a finding that cannot be explained by the current formulation of the Standard Model of particle physics.

The HIBEAM experiment may be an important puzzle piece in the quest to solve this mystery. The experiment will search for spontaneous oscillations between neutrons and antineutrons. It will also search for oscillations into sterile neutrons, a yet undiscovered particle which, if it exists, interacts very weakly with ordinary matter. The neutron oscillation process is thought to be particularly likely for free neutrons that are not bound in nuclei. To maximise the probability of transitions, we therefore need to study a large number of free-flying neutrons. Fortunately, the European Spallation Source (ESS), situated in Lund, Sweden, will be one of the most powerful neutron sources in the world. By studying the neutrons as they propagate in a long vacuum pipe and placing neutron and/or antineutron detectors at the end of the pipe, it is possible to determine whether oscillation has taken place.

Within this thesis, a geometrical model of a new ESS beamline has been developed. The model has been used to simulate the radiation dose generated by the neutrons and photons in the beamline. This is necessary to determine how much shielding is needed to abide by relevant health and safety regulations. The simulations are performed using Monte Carlo simulation programs, where random numbers are combined with physical models and experimentally evaluated reaction probabilities to determine the fate of the particles as they traverse the model.

It is of utmost importance that the rare neutron oscillations can be distinguished by the detector with high efficiency. We must therefore have a good understanding of the background radiation that reaches the detector. In this thesis, a detailed model of the detector has been developed and the background rates in the detector stemming from the ESS neutron source have been estimated. In addition, it is shown how the addition of a strongly neutron-absorbing material, LiF, inside the vacuum pipe can significantly reduce the background in the detector system.

Acknowledgements

First and foremost, let me express my deepest gratitude to my supervisor, Valentina Santoro, for her excellent supervision and collaboration throughout this last year. Without her passion for the project, I would not have come into contact with the collaboration and the present thesis would not have been realised. Despite her very busy schedule, Valentina has taken time to continuously scrutinise and provide feedback on the results, which has inevitably improved the outcome. I also want to direct special thanks for allowing me to travel and represent the collaboration at the APS April Meeting in Sacramento.

I further thank my co-supervisor Matthias Holl for patiently introducing me to CombLayer and other relevant software programs. He has also been an excellent sounding board for new ideas and debugging which has helped me immensely. I also appreciate the well-working cooperation in developing the Geant4 detector model in the latter stages of the project. I further thank my second co-supervisor Blahoslav Rataj for many cordial chats and fruitful collaboration over the last year.

I also wish to thank Luca Zanini, José Ignacio Marquez Damian, Günter Muhrer, and Douglas DiJulio at ESS for technical assistance and helpful neutronics discussions over the course of the project. I also owe gratitude to Madalin Bartis for his collaborative work on the CAD model. I extend wider thanks to the ESS Spallation Physics Group and the Division of Particle and Nuclear Physics at Lund University for their hospitality.

The author gratefully acknowledges that the work has been supported by funding from the ESS. The PHITS simulations performed in this thesis were enabled by resources provided by the ESS Data Management and Software Centre (DMSC). The Geant4 simulations were enabled by resources provided by The Centre for Scientific and Technical Computing at Lund University (LUNARC).

Contents

List of acronyms

CAD	Computer-aided design
CMB	Cosmic microwave background
CPT	Charge, parity and time
DMSC	Data Management and Software Centre
ESS	European Spallation Source
EGS	Electron-Gamma Shower (simulation code)
FOM	Figure of merit
Geant4	Geometry and tracking 4 (simulation code)
GEM	Generalised Evaporation Model
HIBEAM	High-Intensity Baryon Extraction And Measurement
ILL	Institut Laue-Langevin
INCL	Liège intranuclear cascade (simulation model)
KDE	Kernel density estimation
MCNP	Monte Carlo N-Particle (simulation code)
MCPL	Monte Carlo Particle Lists (particle dump file format)
NBOA	Neutron Beam Optical Assembly
PDF	Probability density function
PHITS	Particle and Heavy Ion Transport code System (simulation code)
PMT	Photomultiplier tube
TPC	Time projection chamber
UCN	Ultracold neutrons
VGM	Virtual Geometry Model (geometry interface)
WASA	Wide Angle Shower Apparatus (electromagnetic calorimeter)

List of figures

List of tables

1 Introduction

The European Spallation Source (ESS) in Lund, Sweden, is poised to become a leading facility for neutron-based research upon completion. The high neutron intensity and unique long pulse length will provide new capabilities not available at existing European facilities [3, 4]. At the time of writing, 15 instruments have been approved for construction geared at, e.g., reflectometry, diffractometry, spectroscopy and small-angle neutron scattering [5]. While these instruments will be used in a variety of fields including materials science, life science and surface science, none of the current beamlines is aimed at particle physics experiments [6].

In light of this gap in capability, the HIBEAM (High-Intensity Baryon Extraction and Measurement) collaboration has emerged, proposing to harness the potential of ESS for fundamental physics to conduct a program of free neutron oscillation searches. These phenomena serve as probes of baryon number violation and contribute to addressing fundamental open questions in modern physics, such as baryogenesis and dark matter [2]. The program involves the first search for free neutron-to-antineutron oscillations in three decades, shown schematically in Figure 1. Anticipated advancements in beam optics, detector design, and the ESS's high neutron intensity could yield up to an order of magnitude increase in sensitivity over the latest comparable experiment at Institut Laue Langevin (ILL) [7]. Additionally, HIBEAM aims to look for oscillations between neutrons and sterile neutrons, a potential dark matter particle. Being electrically neutral and meta-stable particles which can be studied in abundance, neutrons offer a promising avenue for studying various dark matter models [2].

When designing new instruments, ensuring radiological safety and compliance with legal restrictions is essential. Hence, shielding calculations need to be performed which require the construction of a geometric model of the beamline compatible with radiation transport codes such as PHITS [8]. Early consideration of shielding is beneficial not only for recognising engineering constraints but also for ensuring there is no adverse impact on neighbouring instruments. This thesis involved the creation of a new PHITS model of the HIBEAM beamline. Using this model, comprehensive beamline simulations have been performed which have informed the engineering design of the beamline.

Considering the expected rarity of neutron oscillation phenomena, it is critical to have a thorough understanding of the background radiation reaching the detector. This is necessary to quantify the extent of radiation damage as well as to ensure efficient event reconstruction which is not obscured by pile-up (concurrent events) or other background-induced effects. In this work, the sought signals are annihilation events from antineutrons hitting a carbon target foil in the centre of an annihilation detector consisting of a time projection chamber (TPC), the electromagnetic calorimeter WASA [9] and a cosmic veto detector. The background meanwhile stems from the direct beam, scatterings and conversions in beamline components and cosmic rays. Within the scope of this thesis, a model of the detector has been developed in Geant4 [10–12] to investigate the composition of the

spallation background at the detector position, which can help advance the design of the detector systems as well as the development of background rejection algorithms.

As a side project to this work, shielding calculations have been performed for temporary beam stops to be employed at several ESS beamlines [1]. The ESS is expected to have beam on target in mid-2025, at which point neutrons will be extracted into the beamlines. However, not all of them will be fully built by then, meaning that temporary beam stops are necessary to absorb the beam so that the allowed radiation levels are not exceeded.

The thesis is organised as follows. In Section 2, the motivation for baryon number violation is presented, discussing both antineutron and sterile neutron oscillations. A quantum mechanical description of such oscillations is also provided. In addition, a brief overview of the principles of particle transport codes is given. Section 3 explains the experimental background to neutron oscillation searches, starting with a historical overview of previous searches and ending with the most recent engineering designs of the HIBEAM beamline. The methodological procedures in terms of simulation models and data processing are presented in Section 4. The corresponding results are described and analysed in Section 5. The thesis ends with some conclusions and an outlook on future research directions in Section 6.

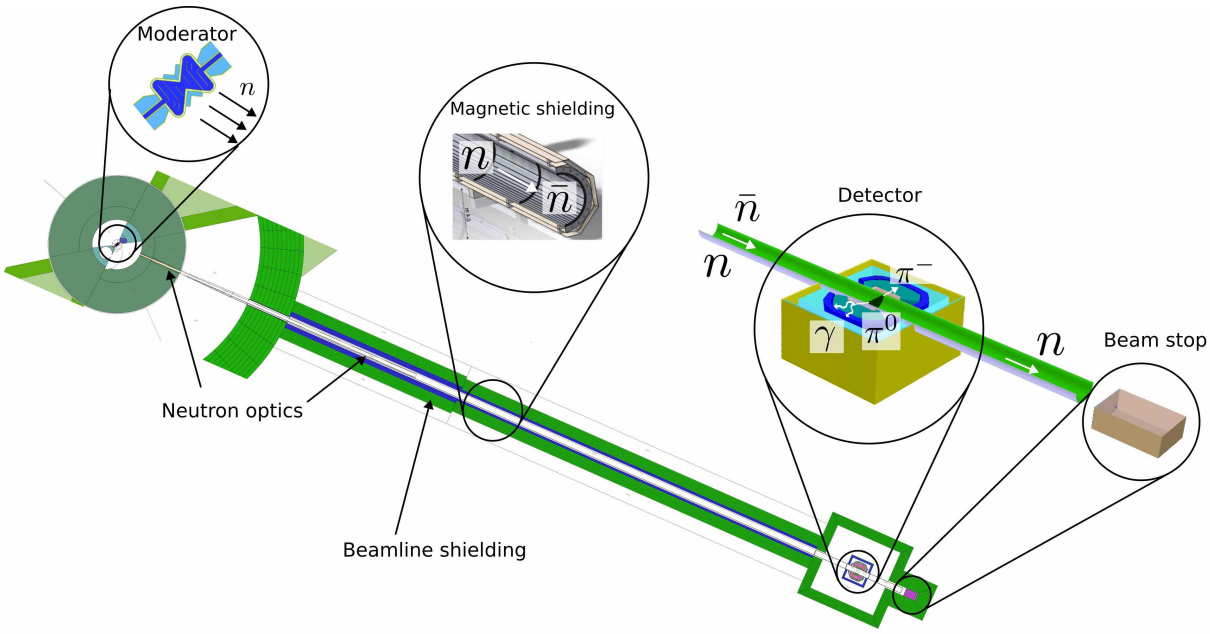

Figure 1: Conceptual overview of one of the proposed experiments to be performed at the HIBEAM beamline, namely neutron-antineutron oscillation searches. Neutrons emanating from the moderator may, in a magnetically shielded beamline, oscillate into antineutrons. Upon annihilation in a carbon foil, a final state of charged pions and photons may be observed in the surrounding detector system. A beam stop absorbs the remaining neutron beam. The figure features the PHITS beamline model and Geant4 detector model, both of which were constructed as a part of this thesis.

2 Theory

2.1 Baryogenesis and the Sakharov conditions

Particles and their corresponding antiparticles exhibit an intriguing symmetry, characterized by identical masses and lifetimes. Given this symmetrical nature, it appears peculiar that our observable universe is predominantly comprised of matter. Is it possible that large regions of antimatter exist elsewhere in the cosmos? This proposition encounters a few obstacles.

Firstly, cosmic rays contain about $\sim 10^4$ times more protons than antiprotons [13]. Even the low occurrence of antiprotons may be explained by secondary production through processes such as $p+p \rightarrow 3p+\bar{p}$ [14, 15]. Secondly, the hypothetical presence of antimatter clusters would result in a significant γ-ray background due to annihilation occurring at the boundaries of these clusters. This would lead to perturbations of the cosmic microwave background (CMB). However, no such deviations in the CMB have been seen to date [16, 17]. In light of this evidence, it is likely that we indeed reside in a baryon asymmetric Universe.

To quantify the extent of baryon asymmetry, one can define the parameter [18]

$$\eta = \frac{n_B - n_{\bar{B}}}{n_\gamma} = 6.12(4) \times 10^{-10}, \tag{1}$$

where n_B, $n_{\bar{B}}$ and n_γ denote the number densities of baryons, anti-baryons, and photons respectively. This value, obtained through CMB measurements, starkly challenges the existing formulations of the Standard Model, leaving the puzzle of baryogenesis—the preference for matter over antimatter—unresolved. In 1967, Andrei Sakharov outlined three prerequisites for baryogenesis [19] shown below.

The Sakharov conditions for baryogenesis

1. Baryon number violation.
2. C violation and CP violation.
3. Interactions out of thermal equilibrium.

Let us briefly consider why each of these conditions is necessary. Unless the universe inherently favoured matter at its inception, there is a need for a process that can change η. Any such process must violate the conservation of baryon number, giving us the first condition. If we find a candidate process which converts anti-baryons into baryons, there should not be an equally probable process which converts baryons into anti-baryons. This

means that charge symmetry must be broken (C-violation). Analogously, charge-parity symmetry stipulates that any process producing a certain number of right-handed baryons must be counterbalanced by an equivalent number of left-handed antibaryons. This would also prevent baryon asymmetry, leading us to the second Sakharov condition [20].

The third condition stems from CPT symmetry. Let the operator Ω represent a CPT transformation (successive application of charge-reversal, parity-reversal and time-reversal operators) and let $\hat{\mathcal{B}}$ denote the baryon number operator. Since baryon number is odd under a CPT transformation (only the charge transformation changes the baryon number of a state), the relation

$$\Omega^{-1}\hat{\mathcal{B}}\Omega = -\hat{\mathcal{B}}, \tag{2}$$

should hold. If the Universe is at thermal equilibrium, then according to statistical mechanics the density matrix of the system is $\rho = e^{-\beta\hat{H}}/Z$ where $\hat{H}$ is the Hamiltonian of the system, β is the thermodynamic beta and Z is the partition function. Let us calculate the ensemble average of the baryon number operator:

$$[\hat{\mathcal{B}}] = \frac{1}{Z}\operatorname{tr}\Big(e^{-\beta\hat{H}}\hat{\mathcal{B}}\Big) = \frac{1}{Z}\operatorname{tr}\Big(\Omega\Omega^{-1}e^{-\beta\hat{H}}\hat{\mathcal{B}}\Big) = \frac{1}{Z}\operatorname{tr}\Big(\Omega^{-1}e^{-\beta\hat{H}}\hat{\mathcal{B}}\Omega\Big), \tag{3}$$

where, in the last step, we used the cyclic property of the trace. By CPT symmetry, the Hamiltonian and its exponential commutes with Ω. We thus conclude using Eq. (2) that

$$[\hat{\mathcal{B}}] = \frac{1}{Z}\operatorname{tr}\Big(e^{-\beta\hat{H}}(\Omega^{-1}\hat{\mathcal{B}}\Omega)\Big) = -\frac{1}{Z}\operatorname{tr}\Big(e^{-\beta\hat{H}}\hat{\mathcal{B}}\Big) = -[\hat{\mathcal{B}}], \tag{4}$$

so $[\hat{\mathcal{B}}] = 0$. This is not compatible with baryon asymmetry, indicating that there must indeed be interactions out of thermal equilibrium [20, 21].

When it comes to the current status of the Sakharov conditions, P violation was discovered in Madame Wu's landmark experiment in 1956 [22]. CP violation was observed in 1964 by studying the decay of neutral kaons [23]. Regarding baryon number conservation, it is generally maintained in all interactions within the Standard Model, except for the chiral anomaly (non-conservation of a chiral current). While this process violates both baryon number $\mathcal{B}$ and lepton number $\mathcal{L}$, it preserves their difference $\mathcal{B} - \mathcal{L}$. This process is insignificant at low temperatures but could become relevant at temperatures approaching the electroweak phase transition $k_B T = \mathcal{O}(160\,\mathrm{GeV})$, prevalent in the early Universe. However, coupled with the Standard Model's CP violation framework, this alone is insufficient to account for the observed baryon asymmetry [24, 25]. Hence, there is growing interest in exploring alternative processes, perhaps beyond the Standard Model, that could violate baryon number conservation. Among these is the neutron oscillation mechanism to be studied by HIBEAM.

2.2 Neutron oscillation formalism

In this section, we shall obtain an understanding of neutron oscillations based on quantum mechanical formalism. In particular, we will deduce what physical parameters influence the probability of detecting neutron oscillations. For simplicity, we confine ourselves to the case of neutron-antineutron oscillations, although the same formalism can be extended to sterile neutrons (see Section 2.3). Consider a ket space spanned by two basis kets for neutron and antineutron states, here denoted $|n\rangle$ and $|\bar{n}\rangle$ respectively. We assume an arbitrary neutron state to be a linear combination of the neutron and antineutron states

$$|\Psi\rangle = n(t)\,|n\rangle + \bar{n}(t)\,|\bar{n}\rangle\,, \tag{5}$$

where $|n(t)|^2$ and $|\bar{n}(t)|^2$ will give the probability of $|\Psi\rangle$ being measured as a neutron or antineutron, respectively, at a given time t. The diagonal elements of the Hamiltonian are the energies of the respective basis states, here denoted E_n and $E_{\bar{n}}$. These are generally not equal but will vary depending on the presence of magnetic and nuclear fields. The transition matrix elements are taken to be a small real number $\langle n|\,\hat{H}\,|\bar{n}\rangle = \langle\bar{n}|\,\hat{H}\,|n\rangle = \alpha$ [24, 25]. The Hamiltonian thus becomes

$$\hat{H} \leftrightarrow \begin{pmatrix} E_n & \alpha \\ \alpha & E_{\bar{n}} \end{pmatrix}. \tag{6}$$

We wish to solve the time-dependent Schrödinger equation, which in this basis takes the form

$$i\hbar\frac{\partial}{\partial t}\begin{pmatrix} n(t) \\ \bar{n}(t) \end{pmatrix} = \begin{pmatrix} E_n & \alpha \\ \alpha & E_{\bar{n}} \end{pmatrix}\begin{pmatrix} n(t) \\ \bar{n}(t) \end{pmatrix}. \tag{7}$$

We begin solving the time-independent Schrödinger equation by diagonalising the Hamiltonian matrix. See Appendix A for a detailed derivation. The resulting eigenenergies are

$$E_{1,2} = \frac{1}{2}\left(E_n + E_{\bar{n}} \pm \sqrt{(\Delta E)^2 + 4\alpha^2}\right), \quad \Delta E = E_n - E_{\bar{n}}, \tag{8}$$

and the corresponding eigenstates, here denoted $|n_1\rangle$ and $|n_2\rangle$ may be expressed as

$$\begin{pmatrix} |n_1\rangle \\ |n_2\rangle \end{pmatrix} = \begin{pmatrix} \cos\theta & \sin\theta \\ -\sin\theta & \cos\theta \end{pmatrix}\begin{pmatrix} |n\rangle \\ |\bar{n}\rangle \end{pmatrix} \implies \begin{pmatrix} |n\rangle \\ |\bar{n}\rangle \end{pmatrix} = \begin{pmatrix} \cos\theta & -\sin\theta \\ \sin\theta & \cos\theta \end{pmatrix}\begin{pmatrix} |n_1\rangle \\ |n_2\rangle \end{pmatrix}, \tag{9}$$

with $\tan 2\theta = 2\alpha/\Delta E$. Let us now determine the oscillation probability. Assume that we are in a pure neutron state $|n\rangle$ at time $t = 0$. Applying the time evolution operator

$\exp\left(-i\hat{H}t/\hbar\right)$, we find that at time t the state has evolved to

$$e^{-iE_1 t/\hbar}\cos\theta\,|n_1\rangle - e^{-iE_2 t/\hbar}\sin\theta\,|n_2\rangle\,. \tag{10}$$

Substituting $|n_1\rangle$ and $|n_2\rangle$ with $|n\rangle$ and $|\bar{n}\rangle$ through the application of Eq. (9) reveals that the state assumes the form

$$n(t)\,|n\rangle + \bar{n}(t)\,|\bar{n}\rangle\,, \tag{11}$$

where

$$n(t) = e^{-iE_1 t/\hbar}\cos^2\theta + e^{-iE_2 t/\hbar}\sin^2\theta, \tag{12}$$

$$\bar{n}(t) = \sin\theta\cos\theta(e^{-iE_1 t/\hbar} - e^{-iE_2 t/\hbar}). \tag{13}$$

We can therefore conclude that the probability of an antineutron oscillation is

$$\begin{aligned} P(n\to\bar{n}) = |\bar{n}(t)|^2 &= \sin^2(2\theta)\sin^2\left(\frac{1}{2\hbar}(E_1-E_2)t\right)e^{-t/\tau} = \\ &= \frac{\alpha^2}{(\Delta E/2)^2+\alpha^2}\sin^2\left(\sqrt{(\Delta E/2)^2+\alpha^2}\,t/\hbar\right)e^{-t/\tau}, \end{aligned} \tag{14}$$

with the added exponential factor accounting for free neutron decay (with mean lifetime $\tau \approx 880\,\mathrm{s}$). In typical experimental conditions, $t \ll \tau$ so this factor can be neglected. In a vacuum environment with low magnetic fields ($\lesssim 5\,\mathrm{nT}$), we enter the so-called quasi-free regime where $\Delta E \cdot t/\hbar \ll 1$. In this case, we may perform a first-order Taylor expansion of the sine function. The resulting expression $(\Delta E/2)^2 + \alpha^2$ cancels out the denominator of the prefactor, leading to a probability of the form

$$P(n\to\bar{n}) \approx \left(\frac{\alpha\cdot t}{\hbar}\right)^2 \equiv \left(\frac{t}{\tau_{n\bar{n}}}\right)^2. \tag{15}$$

Given this expression, it is evident that the appropriate figure of merit (FOM) for neutron oscillation experiments is Nt^2, where N is the number of neutrons, and t is the free flight time. To achieve a high FOM, the neutron source should deliver a high intensity of cold ($\lesssim 25\,\mathrm{meV}$) neutrons. To maximise t, a long, magnetically shielded, beamline under vacuum is required. Optical systems may also be employed to increase the intensity of cold neutrons reaching the detector. Furthermore, a long running time is needed to accumulate enough neutrons to observe such rare processes. The HIBEAM experiment is designed according to these criteria.

2.3 Dark matter and sterile neutrons

Several astronomical observations indicate the existence of matter which we cannot see or otherwise detect, therefore commonly termed *dark matter*. In the 1930s, Knut Lundmark [26] and Fritz Zwicky [27] observed that the velocity dispersion of galaxies in clusters was larger than what could be expected based on the masses of visible objects in the cluster. Around the same time, similar observations were made by Jan Oort regarding the stellar motion in our local galactic neighbourhood [28]. In the 1970s, this was supplemented by Kent Ford and Vera Rubin's measurement of galactic rotation curves [29]. According to Newtonian mechanics, the rotational velocity of an object of mass m orbiting a galactic centre of mass M at radius r should be given by

$$\frac{mv^2}{r} = G\frac{mM}{r^2} \implies v = \sqrt{\frac{GM}{r}} \propto \frac{1}{\sqrt{r}}, \tag{16}$$

assuming the object is sufficiently far from the density distribution of the galactic centre. This is, however, not what is observed in many galaxies. In fact, the observed rotation curves are nearly flat at the edge of the galaxy, with faster rotation than what visible mass can account for. Using various cosmological models, it is possible to fit the dark matter density to photon temperature anisotropies in the CMB. It is found that visible baryonic mass constitutes only around 5 percent of the energy density of the Universe, with 27 percent being dark matter and the remaining 68 percent being *dark energy*, a conceptual energy form driving the accelerating expansion of the Universe [18].

The Standard Model effectively describes the non-gravitational interactions of elementary particles with a theory exhibiting $SU(3)_c \otimes SU(2) \otimes U(1)$ gauge symmetry. It may be described by a Lagrangian $\mathcal{L} = \mathcal{L}_{\text{SM}}$ which depends on the particles and gauge fields [30]. While being a very successful description of a wide range of phenomena, its current formulation does not include dark matter particles. One simple way of incorporating dark matter is to extend the Lagrangian with an additional set of particles and gauge fields, often denoted as a *hidden sector*. Suppose there are additional particles P_i and associated gauge fields G_i. The Lagrangian is then of the form [31]

$$\mathcal{L} = \mathcal{L}_{\text{SM}} + \mathcal{L}_{\text{dark}}(P_i, G_i, \ldots) + \mathcal{L}_{\text{mix}}. \tag{17}$$

The term $\mathcal{L}_{\text{mix}}$ describes any non-gravitational interactions between dark matter and ordinary matter. Due to the expected weakness of such cross-interactions, dark matter particles are often termed *sterile*. The properties of dark matter are heavily dependent on the nature of the hidden sector. For instance, if the gauge bosons in the hidden sector are heavy, then the particles P_i are close to collisionless and often denoted weakly interacting massive particles (WIMPs). Conversely, if the bosons are light or massless, then one may see pronounced self-interactions among the particles [31]. While there is a myriad of dark matter

theories, many feature sterile neutron candidates that may be explored by experimental schemes such as those to be employed by HIBEAM.

To incorporate the possibility of sterile neutron oscillation into the formalism of Section 2.2, the Hamiltonian may be extended into the full $\{|n\rangle, |\bar{n}\rangle, |n'\rangle, |\bar{n}'\rangle\}$ space where the prime ($'$) denotes sterile sector particles. If we consider free neutrons (no influence from nuclear fields), then the energies of the various neutron species are solely determined by their mass (m) and external magnetic fields ($\mathbf{B}$ and its sterile equivalent $\mathbf{B}'$). The Hamiltonian can be written as

$$\hat{H} \leftrightarrow \begin{pmatrix} m_n + \boldsymbol{\mu_n} \cdot \mathbf{B} & \alpha_{n\bar{n}} & \alpha_{nn'} & \alpha_{n\bar{n}'} \\ \alpha_{n\bar{n}} & m_n - \boldsymbol{\mu_n} \cdot \mathbf{B} & \alpha_{n\bar{n}'} & \alpha_{nn'} \\ \alpha_{nn'} & \alpha_{n\bar{n}'} & m_{n'} + \boldsymbol{\mu_{n'}} \cdot \mathbf{B}' & \alpha_{n\bar{n}} \\ \alpha_{n\bar{n}'} & \alpha_{nn'} & \alpha_{n\bar{n}} & m_{n'} - \boldsymbol{\mu_{n'}} \cdot \mathbf{B}' \end{pmatrix}, \tag{18}$$

where $\boldsymbol{\mu}$ denotes the magnetic moments and α the unknown oscillation parameters [24]. Although we shall not endeavour to diagonalise this Hamiltonian, we note by analogy with Section 2.2 that the oscillation probability is maximised when the energy difference between the different states is minimised. If we assume that the mass and magnetic moment of sterile neutrons are the same as their ordinary counterparts, the $n - n'$ oscillation probability is maximised whenever $\mathbf{B} \approx \mathbf{B}'$. The difficulty is that the sterile magnetic field, if it exists, has an unknown magnitude and direction in relation to Earth's ordinary magnetic field. Thus, a complete sterile neutron search must scan a wide magnetic field range [2, 24]. For the HIBEAM beamline, this is realised by a set of adjustable magnetic coils surrounding the vacuum vessel.

2.4 Monte Carlo transport simulations

Monte Carlo simulation is a computational technique widely used in the field of particle transport to model the movement and interactions of particles within a medium. It involves the generation of random numbers to simulate the probabilistic nature of particle interactions. The basic principle is to trace the trajectory of individual particles through the medium, with various physical processes such as scattering, absorption, and emission occurring with a given probability in each time step. The probability distributions are themselves derived from either experimental cross-sections or theoretical models. One critical advantage of Monte Carlo simulation is its ability to handle complex geometries and composite materials where a deterministic treatment is no longer feasible [32]. The complexity of modern particle transport codes does not permit a complete treatment within this thesis, though some particularly relevant aspects will be briefly discussed in the following subsections.

2.4.1 Intranuclear cascade models

To describe the interactions of high-energy hadrons with matter, such as the spallation process at ESS, intranuclear cascade models assume that the interaction may be represented as a series of free-particle binary collisions within the nuclei. The justification for this assumption is that for incident particles in the GeV range, the wavelength is comparable to the internucleon distance ($\sim$ fm). The collisions themselves are considered instantaneous point interactions treated using relativistic kinematics. Since the problem of complex hadronic interactions is broken down into a series of binary collisions, only the free particle cross-section data for nucleon-nucleon and pion-nucleon scattering (elastic and inelastic), charge exchange and pion production are necessary, all of which are well known from experimental data [32].

A successful description of hadronic nuclear interactions necessitates proper initial conditions. The radial density distribution of the target nucleus is typically modelled using a Woods-Saxon distribution of the form

$$\rho(r) = \frac{\rho_0}{1 + \exp((r - R_0)/a)}, \tag{19}$$

with R_0 being the approximate radius of the distribution and a being its diffuseness. The momentum distribution is typically taken to be uniform up to some Fermi momentum p_F. The particles are placed in a potential approximating the nuclear potential, e.g. a square well with momentum-dependent radius (although the exact implementation varies between different codes) [32, 33].

The only quantum mechanical effect included in intranuclear cascades is the Pauli exclusion principle, entailing that no two fermions may occupy the same quantum state, limiting the available phase space for newly formed particles. The simplest way of accounting for this restriction is to neglect any collisions where the energy of any of the collision products falls below the Fermi energy. In more advanced models (e.g. employed by INCL4), the depletion of the Fermi sphere due to prior reactions is accounted for. As the available phase space is dynamically updated during the simulation, this is called dynamical Pauli blocking [33].

2.4.2 Evaporation models

The cascade of collisions described above often leaves the nucleus in a highly excited state. Evaporation models continue the de-excitation process with its associated particle emission. In the commonly employed Weisskopf-Ewing model, the process is viewed in a purely statistical manner, with all possible decay channels satisfying the conservation of energy and angular momentum being occupied with equal probability. As derived already in 1937 by Weisskopf [34], the probability P_j of emitting a particle j with kinetic energy

between ϵ and $\epsilon + \mathrm{d}\epsilon$ (in the centre-of-mass frame) from a parent nucleus i is then given by

$$P_j(\epsilon)\mathrm{d}\epsilon = g_j \frac{m_j}{\pi^2\hbar^2}\sigma_{\mathrm{inv}}(\epsilon)\frac{\rho_d(E-Q-\epsilon)}{\rho_i(E)}\epsilon\mathrm{d}\epsilon, \tag{20}$$

where E is the excitation energy of the parent nucleus, $\rho_{i/d}$ is the level density of the parent/daughter nucleus, $g_j = 2S_j + 1$ is the number of spin states of the emitted particle and $\sigma_{\mathrm{inv}}(\epsilon)$ is the cross-section of the inverse process which can be estimated from geometrical considerations. The Q value can be evaluated from tabulated nuclear masses. The assumed level density distributions and inverse cross-sections vary between different evaporation models, and most models also include fission cross-sections which may compete with evaporation in heavier nuclei. While early evaporation models were restricted to light ejectiles, modern codes allow the treatment of heavier nuclear ejectiles (up to ~ 100 nucleons) and account for the possibility of excitations (which enter Eq. (20) in the form of different Q-values and different spin states leading to different g_j) [32, 35].

The intranuclear cascade and evaporation models described above are often applied for hadron energies ranging from around 20 MeV to several GeV. Below this range, data libraries based on evaluated cross-sections such as ENDF [36] and JENDL [37] are typically used to determine the statistical probability of various processes in the Monte Carlo simulation. A closer description of the models applied in this thesis can be found in Sections 4.4 and 4.5.

2.4.3 Supermirror physics

Neutrons, being electrically neutral, are not influenced by electromagnetic fields and therefore cannot be focused by magnetic systems. To address this fact, one may instead employ neutron supermirrors to focus neutron beams. Typically consisting of alternating layers of materials with differing neutron scattering lengths, neutron supermirrors exploit the constructive interference between the different layers to maximize reflection. This is illustrated in Figure 2(a). In several particle transport codes including PHITS [38] and the neutron ray-tracing program McStas [39], the reflectivity R is described by the empirical formula

$$R = \begin{cases} R_0, & \text{if } Q \leq Q_c. \\ \frac{1}{2}R_0\left(1 - \tanh\left(\frac{Q-mQ_c}{W}\right)\right)\left(1 - \alpha(Q-Q_c)\right), & \text{if } Q > Q_c. \end{cases} \tag{21}$$

with Q being the scattering vector (in $\mathrm{\AA}^{-1}$), defined as

$$Q = \frac{4\pi\sin\theta}{\lambda}, \tag{22}$$

where 2θ is the angle between the incident and outgoing wave vectors and λ is the wavelength. Eq. (21) tells us that the reflectivity is constant up to Q_c which is the critical

scattering vector for a single mirror layer. At higher values of Q, the reflectivity drops almost linearly with slope α before reaching a cutoff at $Q = mQ_c$ with width W as seen in Figure 2(b). The value of m, often used to characterise supermirror performance, is determined by the chosen sequence of bilayer materials and the number of bilayers [38, 39].

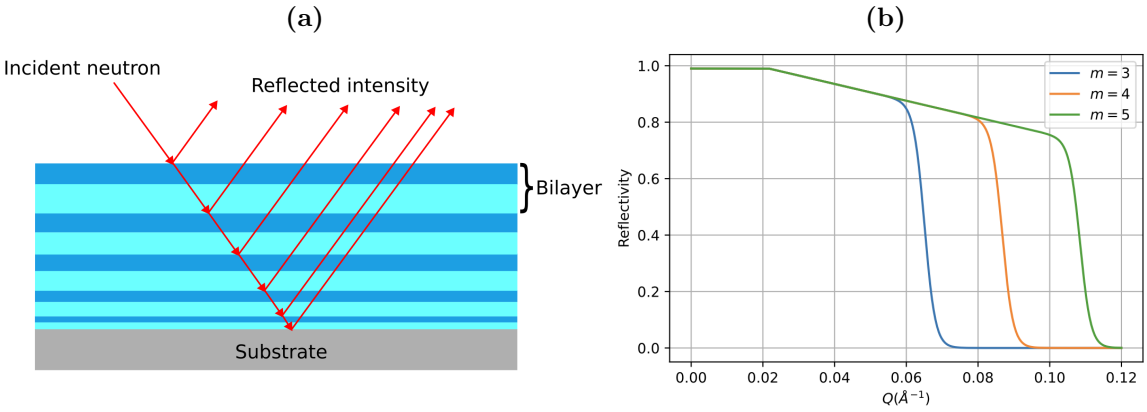

Figure 2: Panel (a): Schematic of a bilayer neutron supermirror. **Panel (b)**: The reflectivity described by Eq. (21) with the McStas default parameters $R_0 = 0.99$, $Q_c = 0.0217\,\text{Å}^{-1}$, $\alpha = 3\,\text{Å}$ and $W = 0.003\,\text{Å}^{-1}$ for different values of m.

3 Experimental background

3.1 Previous and concurrent searches

3.1.1 Antineutron oscillation searches

Neutron oscillation searches can be grouped into two categories, namely those using free and bound neutrons, respectively. The most recent large-scale free neutron oscillation experiment was performed during 1989-1991 at ILL [7]. The experiment utilised a 58 MW high-flux nuclear reactor moderated by 25 K liquid deuterium. The neutrons were transported through a bent neutron guide leading out of direct sight to reduce the background from γ rays and fast neutrons. The guide led into a 33.6 m long focussing reflector inside a 95 m long vacuum pipe, of which 81 m were magnetically shielded so that antineutron oscillation may occur. The neutrons proceeded to hit a 1.1 m diameter carbon annihilation target. This setup is shown in Figure 3. As no antineutron was observed, the experiment provides a lower limit on the neutron-antineutron oscillation time of $\tau_{n\bar{n}} \geq 8.6 \times 10^7\,\text{s}$ at 90% confidence level. The FOM obtained by the experiment (recall Section 2.2) is $1.5 \times 10^9\,\text{n} \cdot \text{s}$ over a full operational year. Since it is expected that the ESS will have fewer operational hours than ILL (due to a greater prevalence of long shutdowns), one ILL unit is taken to be $2.0 \times 10^9\,\text{n} \cdot \text{s}$. The goal of the HIBEAM experiment is to achieve an order of magnitude improvement over this value, while for the subsequent NNBAR experiment, an improvement of at least three orders of magnitude is envisioned [40].

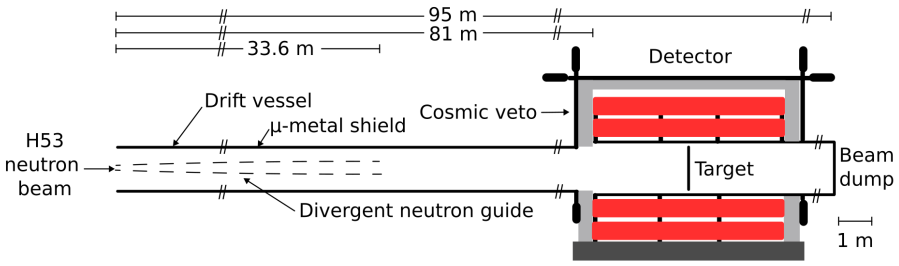

Figure 3: Experimental setup employed for the antineutron oscillation search performed at ILL around 1990 (see the text for further details). Based on Figure 1 of Ref. [7].

As will be described in Section 3.3, the strategy of the HIBEAM project is in many ways analogous to that of the ILL experiment. However, a very different technique is possible, which is to study neutrons bound in nuclei. One issue with this approach is that the strong nuclear field introduces an energy difference between neutrons and antineutrons on the order of tens of MeV. As evident from Eq. (14), this drastically reduces the oscillation probability. To counteract this deficit, sensitive searches are made possible using large-volume detectors such as Super-Kamiokande [41] and SNO [42] with future experiments planned for DUNE [43] and Hyper-Kamiokande [44]. While this approach enables the reuse of existing experimental setups (typically designed for neutrino observation experiments), atmospheric backgrounds, as well as intranuclear scattering effects in the large detector volume, complicate event identification. Caution should be exercised when comparing free and bound neutron searches due to the unknown mechanism of neutron oscillation, although a heuristic estimate of the $n \to \bar{n}$ conversion time T in a given nucleus is

$$T = R\tau_{n\bar{n}}^2, \tag{23}$$

where $R \sim 10^{22}\,\mathrm{s}^{-1}$ is a nuclear suppression factor that depends on the nucleus and the chosen nuclear structure model. With this relation, the strongest limit on the oscillation time has been obtained by Super-Kamiokande for neutrons bound in ^{16}O at $\tau_{n\bar{n}} > 4.7 \times 10^8\,\mathrm{s}$ [41].

3.1.2 Sterile neutron oscillation searches

One can envision three different approaches to sterile neutron searches, pictured schematically in Figure 4. In disappearance measurements, neutron fluxes are carefully measured at the beginning and end of a long beamline. If there is an abnormal loss of neutrons at the end, this may be explained by neutrons oscillating into sterile neutrons, evading detection in the second neutron counter. To perform disappearance measurements with high sensitivity, the neutron counters must be sensitive to very small changes in the neutron flux. A variant of this strategy is to instead trap neutrons in an ultracold neutron (UCN) bottle and to detect any disappearance over time.

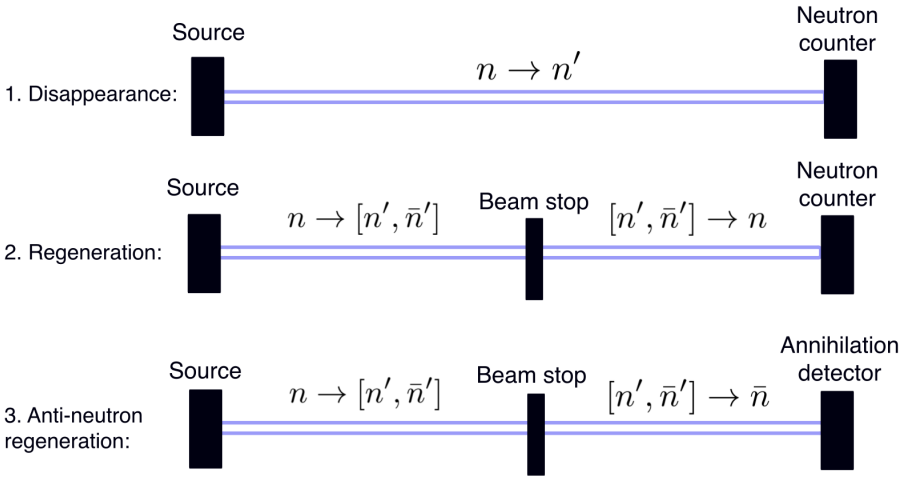

Figure 4: Three approaches in searching for sterile neutrons. In disappearance measurements, neutron fluxes are measured at either end of a long beamline to see if any neutrons have oscillated into undetectable sterile neutrons. In regeneration experiments, a beam stop is placed along the beamline, allowing only sterile neutrons to pass. On the other end, a neutron counter or annihilation detector is placed to detect if the sterile neutron has oscillated back into a neutron or antineutron, respectively.

For regeneration searches, a beam stop is placed in the middle of the beamline. This removes the background from the direct beam, only allowing sterile neutrons to pass. If the sterile neutrons oscillate back into neutrons in the second half of the beamline, they can be detected in a neutron counter. Besides ensuring that the beam stop is sufficiently big, it is essential to have a complete understanding of the neutron background at the detector so that the rare signal events can be distinguished.

A related third option is to look for sterile neutrons which oscillate into antineutrons after the beam stop. This approach has the distinct advantage of being the least background-sensitive due to the comparatively unique signature of antineutron annihilation, combined with the absence of spallation background owing to the beam stop. For this approach, it is also possible to reuse parts of the same detector system as for direct antineutron oscillation searches. It's important to note that this experimental approach is not sensitive to the neutron-antineutron and neutron-sterile neutron oscillation times separately, but rather the product $\tau_{nn'}\tau_{n'\bar{n}}$ [2, 24].

Only disappearance measurements have been undertaken in the past, mostly using UCN bottles. As described in Section 2.3, the exclusion limits will depend on what external magnetic field is being applied, corresponding to the unknown sterile magnetic field. A compilation of the currently excluded oscillation times is shown in Figure 5 [2].

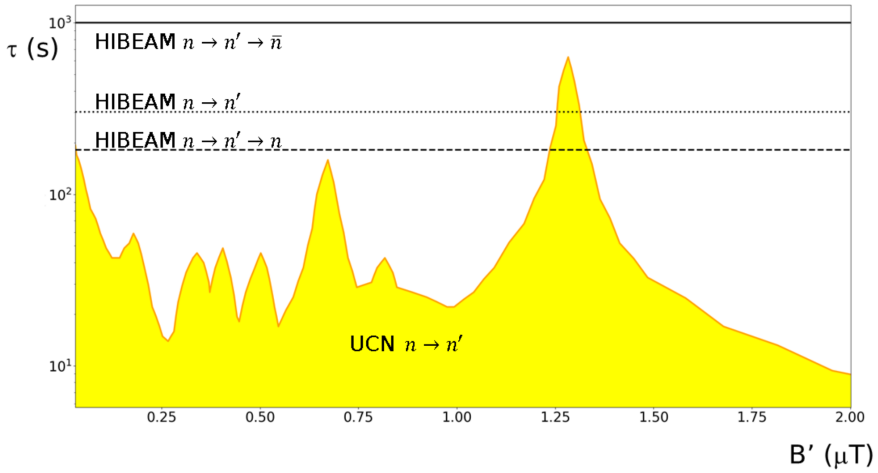

Figure 5: The shaded yellow area denotes oscillation times $\tau_{nn'}$ which have been excluded by UCN measurements for various magnitudes of the sterile magnetic field $\mathbf{B}'$. The dashed and dotted lines show the expected exclusion limits achieved by HIBEAM after one year of operations for regeneration and disappearance measurements, respectively. The solid line indicates the expected exclusion limit in $\sqrt{\tau_{nn'}\tau_{n'\bar{n}}}$ from an antineutron regeneration setup. Figure obtained from Ref. [2].

3.2 The European Spallation Source

ESS is a neutron facility under construction in Lund, Sweden that strives to become one of the world's leading research centres for neutron science. It is a European Research Infrastructure Consortium with 13 member states. The data collected by ESS will be stored and analysed at the Data Management and Software Centre (DMSC) in Copenhagen, making Sweden and Denmark joint host nations.

An overview of the neutron production process at ESS is shown in Figure 6. An ion source generates protons which are accelerated by a set of normal-conducting and later superconducting radiofrequency cavities in a 602.5 m long accelerator tunnel, reaching a final energy of 800 MeV. The ESS is committed to delivering 2 MW by 2028, with a future proposed upgrade enabling 5 MW operation (2 GeV proton energy). The proton pulse length is 2.86 ms with an operating frequency of 14 Hz. The accelerated protons collide with a tungsten target initiating a spallation process where inelastic nuclear reactions break apart the nuclei into smaller fragments, emitting a large number of neutrons in the process. To reduce radiation damage and ensure sufficient cooling, several tungsten target segments are mounted on a rotating wheel in a stainless steel frame. The wheel is cooled by a helium gas system interfaced with a secondary water system [3, 4].

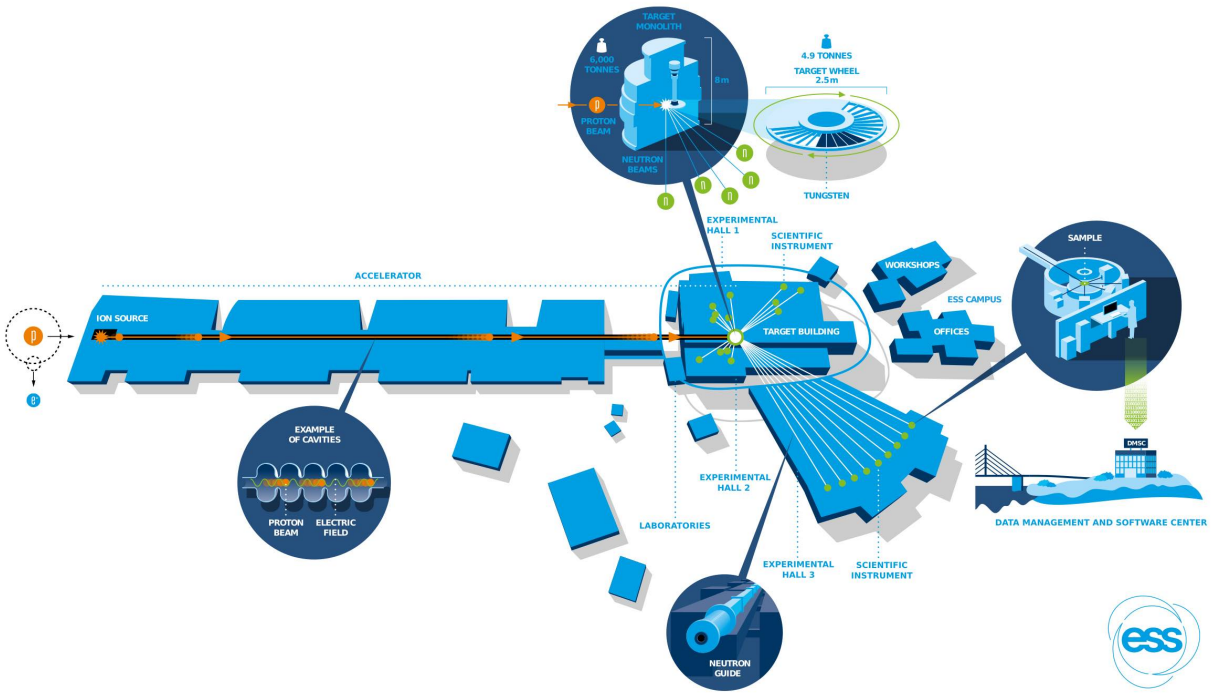

Figure 6: Overview of the European Spallation Source. Protons are generated in the ion source and accelerated in a 602.5 m long accelerator before striking a rotating tungsten target. Neutrons released from the spallation reaction are slowed down in the moderator and transported through neutron guides to various scientific instruments. The recorded data is transmitted to the Data Management and Software Centre in Copenhagen. Figure courtesy of ESS [45].

Situated 13.7 cm above the spallation target, a moderator slows down the emitted neutrons through a series of predominantly elastic collisions. The moderator, shown in Figure 7(a), is called low-dimensional due to its height of only 3 cm. It provides a bispectral neutron beam with units of light water and 20 K parahydrogen giving thermal and cold neutrons, respectively [46]. The moderator and a reflector are enclosed in a plug that can be rotated such that it sits above the target. The whole setup is contained within a monolith structure, shown in Figure 7(b), shielding the surroundings from the ionising radiation produced during the spallation process.

The monolith has room for 42 openings known as beam ports, although only 17 will be opened in the initial stage. Through the use of choppers, optical systems and polarizers, neutrons tuned for the different experiments can be obtained. Outside the monolith, there is a second shielding structure made of heavy (magnetite-based) concrete called the bunker through which the beamlines pass. Outside the bunker, experimental stations are placed [3, 4].

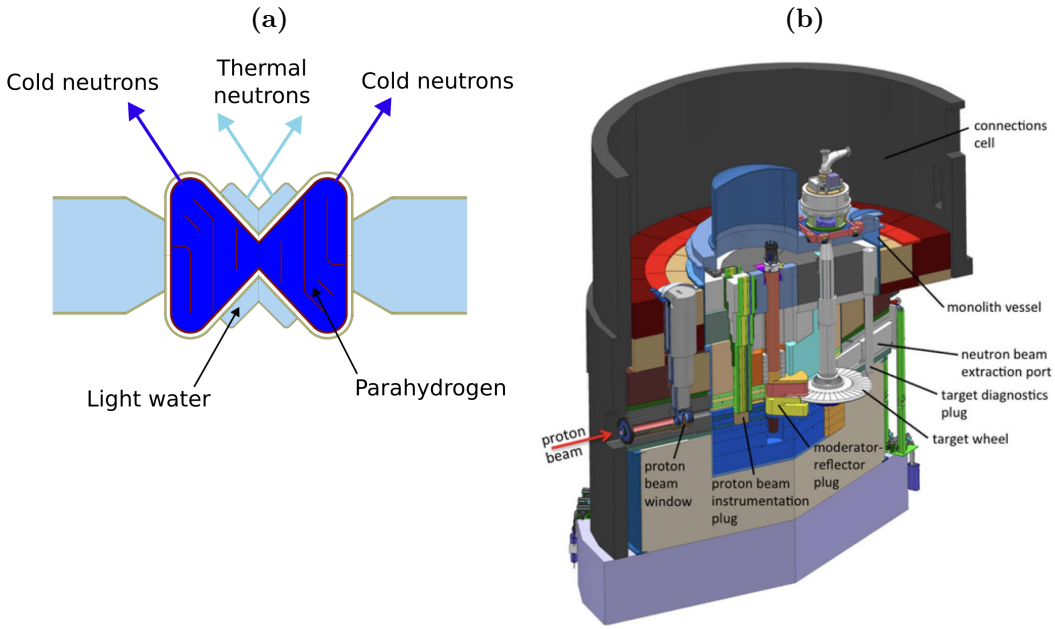

Figure 7: Panel (a): The ESS moderator located above the spallation target. The light and dark blue arrows indicate beam extraction configurations for thermal and cold neutrons, respectively. **Panel (b)**: The target monolith showing the target wheel, the moderator-reflector plug (rotatable above the target) and an extraction port. The monolith itself is predominantly made of steel. Figure courtesy of ESS.

3.3 The HIBEAM beamline

3.3.1 General beamline description

HIBEAM is a proposed particle physics beamline at ESS, envisioned to use the E6 beam port in the eastern sector of ESS. A CAD drawing of the positioning of the beamline in the ESS instrument hall is provided in Figure 8. The beamline will serve two main purposes. Firstly, it will perform searches for sterile neutrons using each of the three strategies described in Section 3.1.2. Secondly, it will perform neutron-antineutron oscillation searches with a sensitivity surpassing that of the 1990 ILL experiment. This will serve as a proof-of-concept and provide for research and development opportunities ahead of the future NNBAR experiment, which is envisioned to make use of the Large Beam Port at ESS, occupying the space of three ordinary beam ports, and a 200 m long beamline [40].

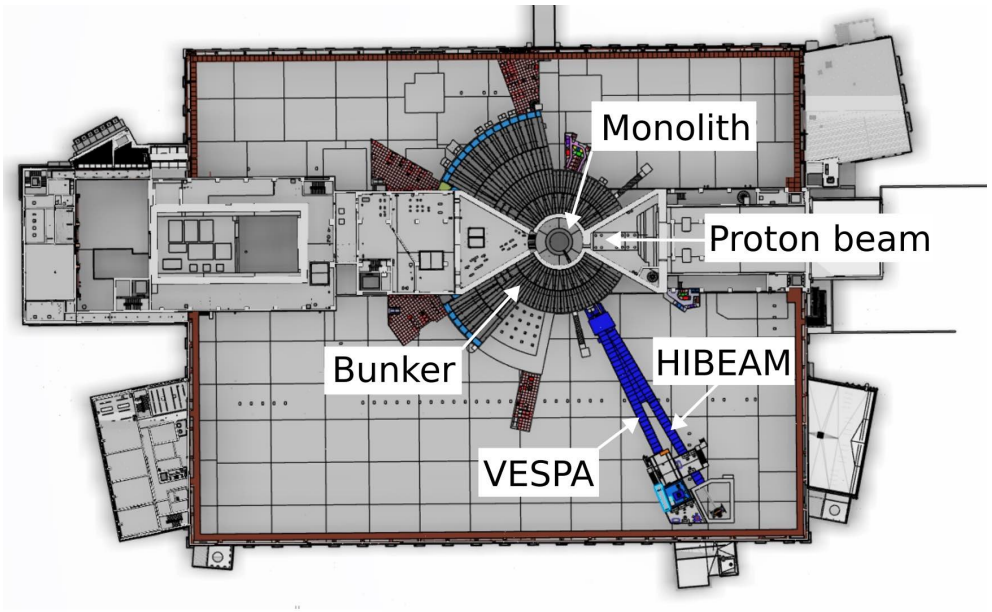

Figure 8: A CAD drawing showing the location of the proposed HIBEAM beamline with its neighbour VESPA within the main experimental hall of ESS. The proton beam comes from the right and hits the spallation target inside the monolith. The CAD model was produced by M. Bartis under consultation with the author and B. Rataj.

The HIBEAM beamline consists of a long straight vacuum pipe that proceeds to a detector system placed 65 m from the moderator. To transport the highest possible flux of cold neutrons, two neutron supermirror systems will be installed. The first is called the Neutron Beam Optics Assembly (NBOA) and will be situated within an insert installed in the monolith, located between 2 m and 5.5 m from the moderator. The second optical system is 20 m long and begins inside the bunker at 6.2 m from the moderator. The current design, optimised to maximise the FOM mentioned in Section 2.2, features elliptical $m = 4$ neutron supermirrors [47, 48]. For this thesis, a Ni/Ti surface on a copper substrate is assumed.

After leaving the bunker, the neutrons enter a magnetically controlled area. This can be achieved by surrounding the vacuum pipe with a magnetic shield made of mu-metal, a nickel-iron alloy with very high permeability. The shield provides a low-reluctance path for the magnetic flux to pass, effectively shielding the inside from external fields. As described in Section 2.3, sterile neutron searches necessitate the ability to generate adjustable longitudinal and transverse magnetic fields. Longitudinal fields can be achieved using solenoids wound axially along the vacuum pipe. The transverse fields can be generated by so-called cosine-theta coils, which achieve a constant dipole field by arranging the current density on a cylindrical surface according to a $\cos\theta$ distribution [2].

Outside the bunker and around the detector, it is necessary to install radiological shielding. This thesis has provided shielding estimates which have informed the engineering design of the beamline. A CAD drawing of this conceptual design is shown in Figure 9.

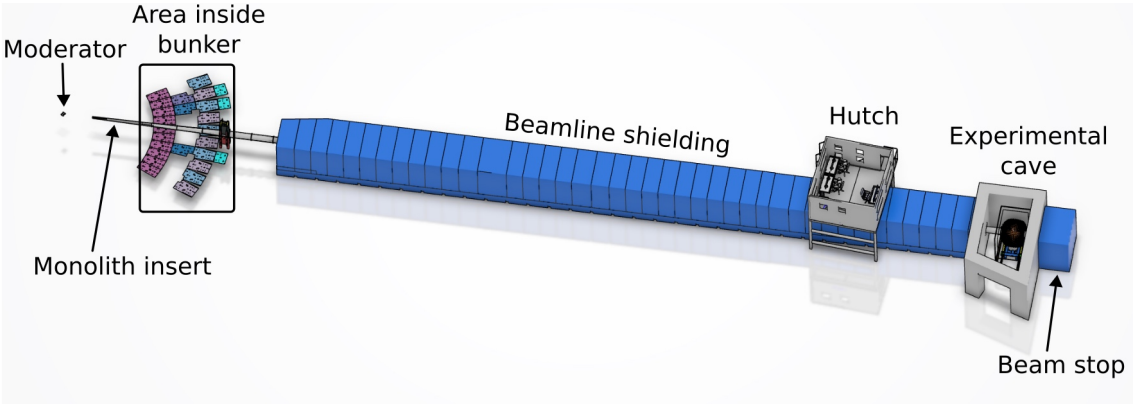

Figure 9: A conceptual design of HIBEAM with relevant components marked. The CAD model was produced by M. Bartis under consultation with the author and B. Rataj.

3.3.2 Detector description

There are two main types of detectors being used at the HIBEAM beamline, neutron counters and an annihilation detector. The neutron counters, necessary for disappearance and regeneration searches (see Section 3.1.2), do not yet have a final design concept and were not modelled in this thesis. The reader is thus referred to Ref. [2] for further details.

The annihilation detector system, shown schematically in Figure 10, contains a carbon foil target. When antineutrons strike this foil, a multipion state is formed with three to five charged pions and photons from the π^0 decay. The detailed composition has been estimated by simulations and existing experimental data sets for $\bar{p}^{12}$C reactions [24, 49]. It is important that the detector system can identify charged pions and reconstruct the π^0 over a wide momentum range. The detector consists of three parts, the time projection chamber (TPC), the WASA calorimeter and a cosmic veto detector. The purpose of the TPC is to provide 3D tracking of charged particles. The TPC is a gas-filled cylinder with gas electron multiplier stacks at the end. When a charged particle passes through the TPC, the gas is ionised and the resulting ion-electron pairs are separated by an electric field. The electric signal is amplified by the multipliers such that it can be measured with conventional electronics. Based on the track's 2D projection, combined with timing information and the drift velocity, the 3D location of the track can be determined [2].

The WASA calorimeter will measure the energies of photons and charged particles to perform invariant mass reconstruction. The calorimeter consists of about 1000 modules of CsI(Na) scintillation crystals with slightly varying dimensions. The crystals are surrounded by an iron yoke. The scintillation light produced by the crystals is converted into electric signals by photomultiplier tubes (PMTs) passing through the yoke. The calorimeter has previously been used at CELSIUS in Uppsala [9], COSY at Jülich [50] and is currently at GSI/FAIR in Darmstadt [51].

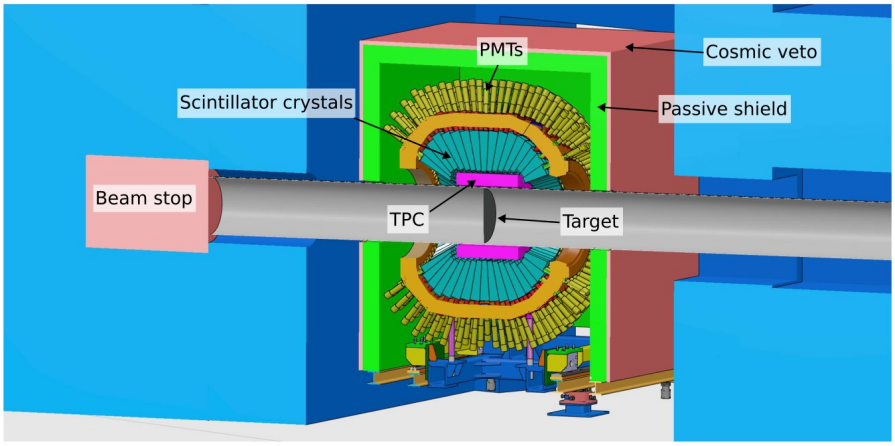

Figure 10: A conceptual design of the HIBEAM detector with relevant components marked. The CAD model was produced by M. Bartis under consultation with the author.

Since cosmic rays are energetic enough to constitute possible signal candidates, a cosmic veto detector consisting of scintillator bars will surround the calorimeter. Events coincident with signals in the cosmic veto will be discarded. A passive shield between WASA and the cosmic veto is present to prevent self-inhibition from annihilation pions. Cosmic events created by neutral particles can be rejected by noting the absence of interaction vertices in the carbon foil. The frequency of background events caused by cosmic events can also be studied by closing the beamline shutter [2]. For $n - \bar{n}$ searches, a beam stop must be placed behind the detector to ensure absorption of the remaining neutron beam. This is the configuration shown in Figure 10. In $n - n'$ searches, a beam stop is instead placed in the middle of the beamline, removing the requirement for a beam stop behind the detector. In this case, it is possible to place a TPC endcap and additional scintillator crystals in the forward direction to improve angular coverage.

4 Methodology

4.1 Overview

This thesis has had two primary objectives, namely to perform shielding calculations for the full HIBEAM beamline and to study the spallation background in detector simulations. This has resulted in the application of several sets of simulation software and data analysis tools. An overview of the process is shown in Figure 11. Firstly, a simulation of the spallation process and the subsequent neutron moderation was performed in PHITS. The simulation was carried out using a source of monoenergetic protons with a $12 \times 4\,\mathrm{cm}^2$ cross-section directed towards the centre of one segment of the tungsten target. The geometry of all PHITS simulations was defined using CombLayer [52, 53], a C++-based code to create complex geometries compatible with simulation codes like MCNP and PHITS. CombLayer already features a model of the spallation target and moderator configuration as well as

pre-existing classes for a variety of common components such as vacuum pipes, neutron guides, and shielding blocks. A closer description of the PHITS geometry construction is presented in Section 4.2.1.

Running simulations from a proton source quickly becomes computationally intensive given that only very few of the produced neutrons will enter the relevant beam port and even fewer make it through the monolith to where the beamline shielding begins. To achieve statistics with sufficiently low statistical uncertainty across the whole beamline, millions of neutrons entering the correct beam port with small angular divergence are required. This is not computationally feasible at the current time, especially for repeated simulations for optimisation of various parameters. For this reason, the neutrons entering the relevant beam port (2 m from the moderator) were recorded in an MCPL file, a file format containing the position, direction, energy and statistical weights of simulated particles [54]. Two different methods to proceed were considered. The first involved extracting the energy and polar angle distributions (with respect to the beamline axis) and creating an analytical neutron source term at the beam port opening. The second made use of KDSource [55, 56], a software package that generates arbitrarily large MCPL files of particles approximating the original distribution using kernel density estimation. These two approaches are described further in Section 4.3.

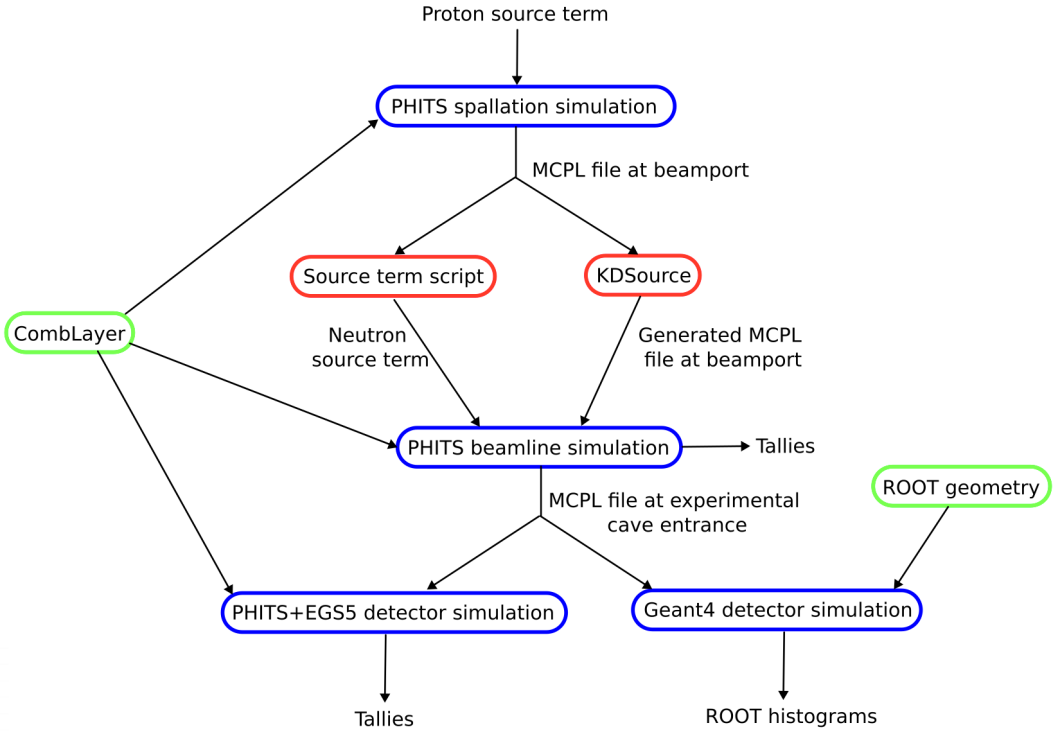

Figure 11: Flowchart illustrating the geometry construction (green), simulations (blue) and other data processing tools (red) applied in this thesis. A description of the steps is found in the text.

Using these two methods, beamline simulations were performed for the HIBEAM beamline. The shielding was designed to satisfy a 1.5 µSv/h dose rate threshold on all shielding surfaces. Further details on how the dose rates are calculated, as well as variance reduction methods, are provided in Section 4.4.

During beamline simulations, an MCPL file was extracted at the entrance of the experimental cave, located 61 m from the moderator. This file was used as input for detector simulations in both PHITS and Geant4. The PHITS detector simulations were now used in combination with EGS5, a code enabling the coupled transport of photons and electrons. The Geant4 simulations were performed with a detailed detector model developed using ROOT's geometry classes [57]. Further details on the Geant4 model are presented in Section 4.5.

4.2 PHITS geometry construction

4.2.1 HIBEAM beamline geometry

A new HIBEAM beamline model was constructed starting from the E6 beam port of the ESS. An overview of the beamline model is shown in Figure 12.

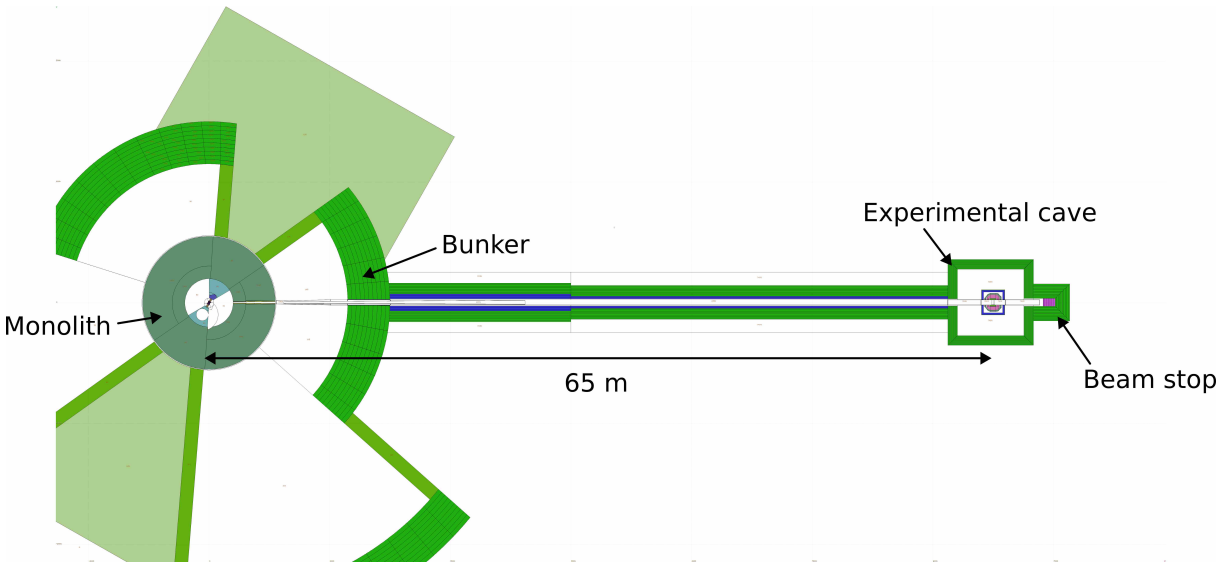

Figure 12: Overview of the PHITS/MCNP geometric model of the HIBEAM beamline.

A more detailed view of the geometry inside the bunker is provided in Figure 13. It starts with a monolith insert containing the NBOA with a 4 µm thick Ni/Ti coating on a copper substrate. After the monolith, a tapered 5 mm thick aluminium vacuum pipe extends up to 43 cm in diameter at a distance of 10 m from the moderator. A straight pipe then leads all the way to the detector position at 65 m from the moderator. Starting 6.2 m from the moderator and extending 20 m, a second optical guide is located. Both guide systems are asymmetrically tapered according to the specifications of Ref. [47], although the guide surfaces are straight in this model. The positioning of the guides necessitates that the detector system be placed 50 cm below the moderator height and 40 cm away from the beam port axis towards the E7 beam port. The rotational orientation of the beamline outside the monolith was adjusted to fulfil this criterion. An $m = 4$ supermirror surface, with the McStas default parameters indicated in Figure 2(b), was defined between the Ni/Ti coating and the copper substrate.

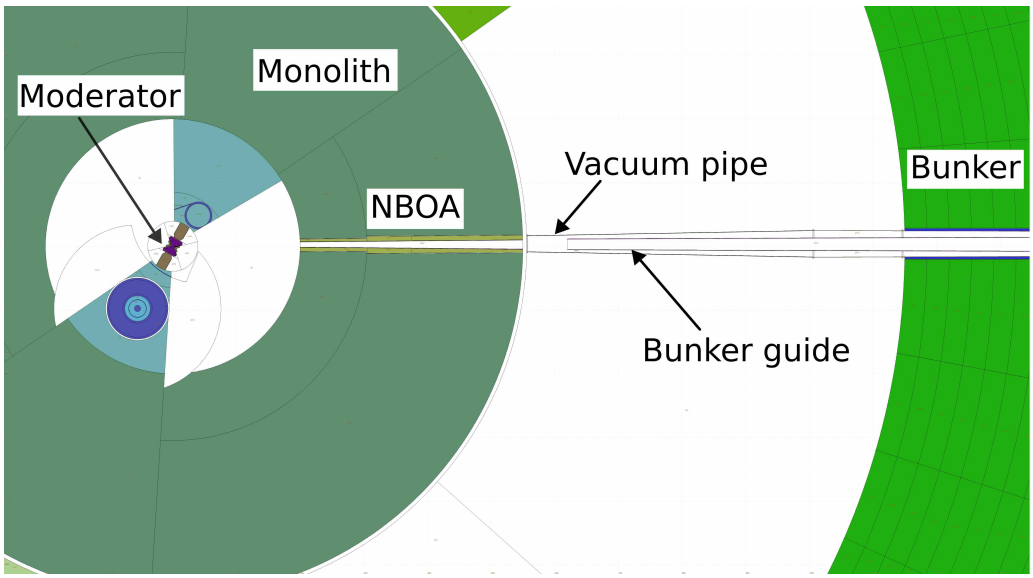

Figure 13: Illustration of the PHITS/MCNP geometry inside the bunker.

Outside the bunker, the pipe is surrounded by steel and heavy concrete as indicated by Figure 14. The experimental cave, containing a simplified detector model, is shown in greater detail in Figure 15. The walls of the cave are made of heavy concrete. The detector was based on CAD drawings of the WASA calorimeter with its CsI(Na) scintillator crystals. Inside the calorimeter, an 80 % Ar/20 % CO_2 gas mixture representing the TPC is placed. Outside WASA, an iron yoke, a steel passive shield and a polystyrene cosmic veto detector are modelled (see Section 3.3.2 for further details). The detector is situated in an experimental cave made of heavy concrete. Behind the annihilation target, a beam stop is made from copper which is coated on its front surface with 2.5 mm of B_4C.

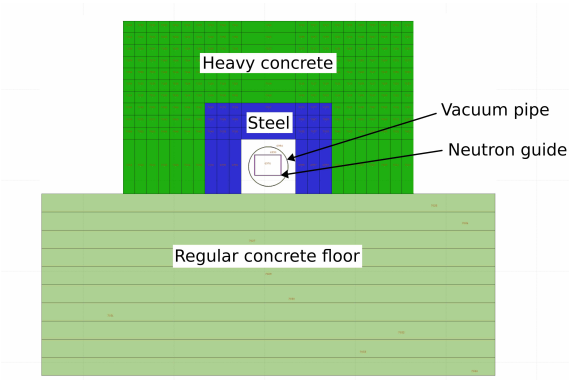

Figure 14: Cross-sectional view of the beamline just outside the bunker, showing the usage of steel and heavy concrete around the vacuum pipe.

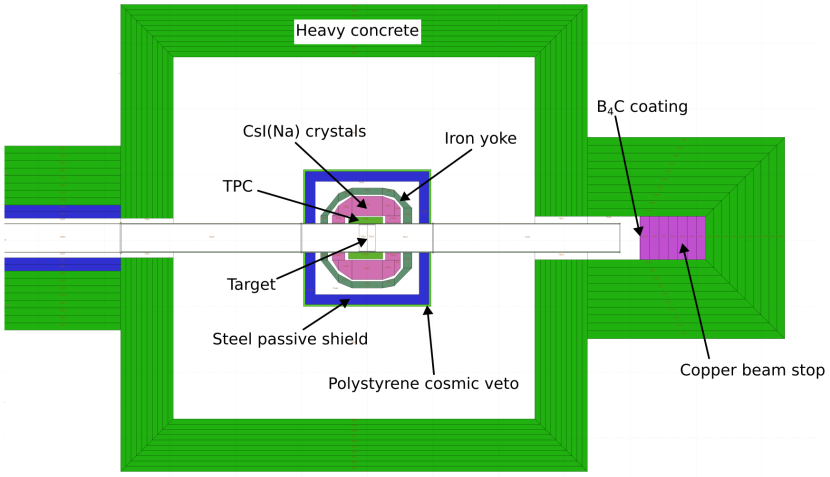

Figure 15: Illustration of the experimental cave in the PHITS/MCNP geometry, showing different components of the detector and beam stop.

4.2.2 Beam stop geometry

While the primary focus of this thesis has been on beamline simulations for the HIBEAM beamline, beam stop simulations have also been performed for a generic setup being used for beamlines that are not complete when ESS becomes operational. In these simulations, the monolith insert has the dimensions of the MAGiC instrument [5] on the W6 beamline. Several configurations were studied, one of which is shown in Figure 16. Here, the exit of the monolith guide is covered with 5 mm of B_4C. A 5 mm thick aluminium pipe proceeds from the monolith to the bunker insert. Outside the bunker is a beam stop made of steel and heavy concrete, the outer dimensions of which were adjusted to meet the dose rate requirements (see Section 4.4). This is all sitting on top of the regular concrete floor of the facility. A 1 cm gap is assumed between the beam stop and the bunker due to the

imperfect flatness of the shielding blocks, necessitating the usage of an extra 10 cm rim of steel in the gap to prevent streaming.

Beyond the configuration of Figure 16, the impact of removing the vacuum pipe and moving the B_4C layer 3 m downstream was investigated. In addition, it was determined how much the beam stop dimensions could be reduced upon installation of heavy concrete plugs in the bunker. Two plugs were considered, with lengths of 1.76 m and 1.74 m in the upstream or downstream feedthrough, respectively. A 1.5 cm gap is assumed on all sides of the plug to the feedthrough. For the beam stop simulations, a pre-existing neutron source term for the CSPEC beamline [5] (considered a worst-case scenario due to its location with respect to the incident proton beam) was converted from MCNP to PHITS. A reduced beam power of 0.5 MW is assumed as this will be the initial operating power during beam on target.

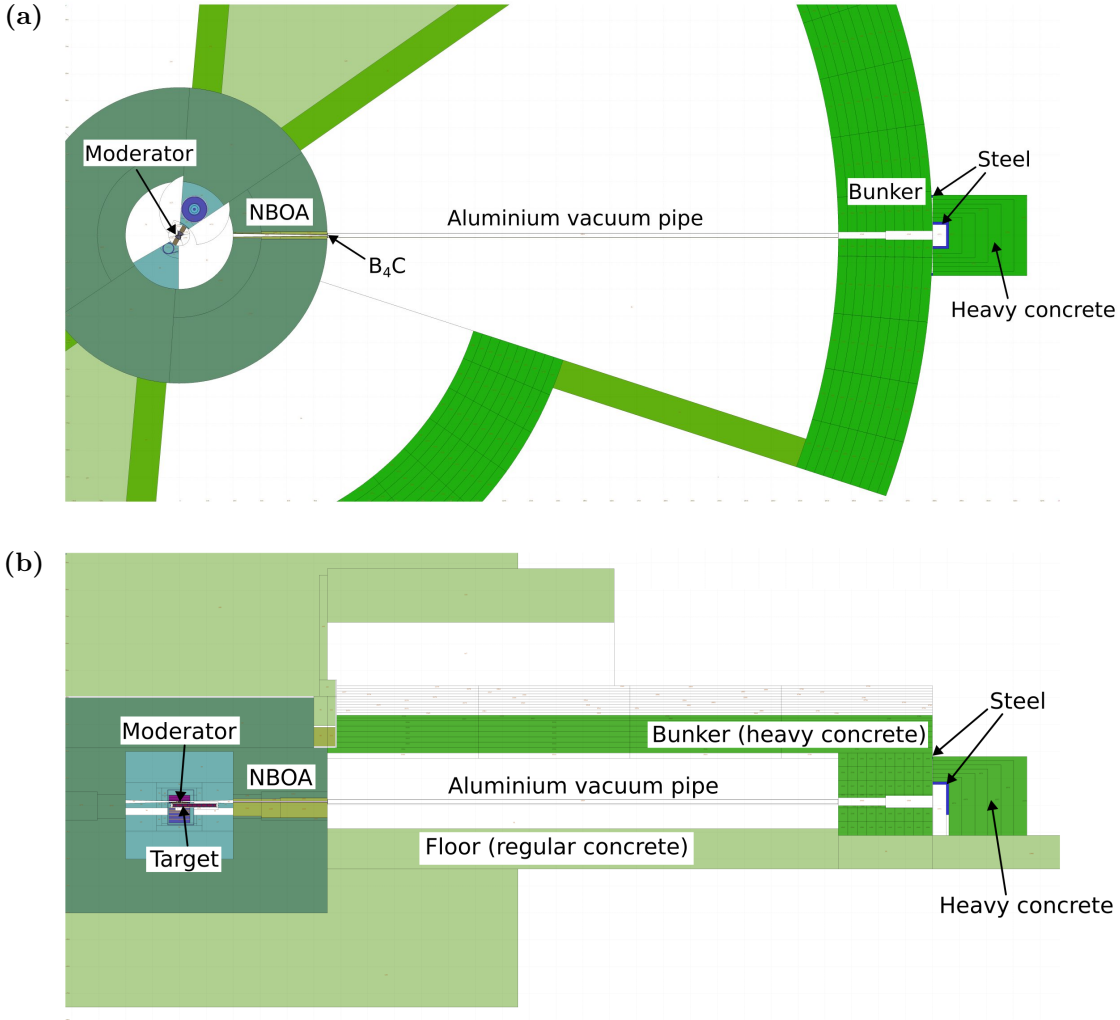

Figure 16: Overview of the beam stop geometry model used for simulations. Panel (a) shows a horizontal projection and Panel (b) shows a vertical projection along the centre of the beamline. Further information is in the text.

4.3 Neutron source construction

In this section, we discuss how neutron sources were constructed to allow for high-statistics beamline simulations. As mentioned in Section 4.1, a surface fluence tally at the beam port opening recorded all particles entering the E6 beam port. In total, about 6.4×10^5 neutrons were recorded in this way. To proceed, two different approaches were considered. The first was to use the measured energy and polar angle distributions to define a PHITS source term at the beam port surface. The second was to use an adaptive multivariate kernel density estimator to generate a density distribution from which an arbitrary number of particles can be obtained. These two methods are covered in the following sections.

4.3.1 PHITS source term

The method from Ref. [58], which has been employed extensively for radiation shielding calculations at ESS, was used. The polar angle θ of each neutron with respect to the beamline axis (here called the x-axis) was calculated from

$$\cos\theta = \frac{v_x}{\sqrt{v_x^2 + v_y^2 + v_z^2}}, \tag{24}$$

where v is the neutron velocity. Energy spectra (weighted by the statistical particle weights) were determined for neutrons in angular bins of 1° in the range $0° < \theta < 5°$. This restriction in polar angle is motivated by the fact that the vast contribution to the dose outside the bunker comes from neutrons in this range. The polar angle distribution is further subdivided into bins of 0.1° width. By sampling from these energy and polar angle spectra, a virtual rectangular neutron source was defined at the position of the monolith insert opening. The neutrons are generated uniformly on the surface of the source.

The normalisation factor was determined as follows. Throughout this thesis, it is assumed that ESS will operate at 5 MW (2 GeV proton energy) as required for instrument shielding simulations. The average proton current is expected to be 2.5 mA, meaning that the number of incident protons on target per second is

$$\frac{2.5 \times 10^{-3}\,\mathrm{C/s}}{1.602 \times 10^{-19}\,\mathrm{C/p}} \approx 1.56 \times 10^{16}\,\mathrm{p/s}, \tag{25}$$

which is the normalisation factor applied for runs using the proton source. By noting that 300 million incident protons were required to create the MCPL file which contains neutrons with a total statistical weight of 1.97×10^5 in the $0° < \theta < 5°$ angular range, we calculate

$$\frac{1.97 \times 10^5}{3 \times 10^8}\mathrm{n/p} \cdot 1.56 \times 10^{16}\,\mathrm{p/s} \approx 1.02 \times 10^{13}\,\mathrm{n/s}, \tag{26}$$

as the normalisation for runs using the neutron source term.

4.3.2 Kernel density estimation

Multivariate kernel density estimation (KDE) is a method used to estimate a joint probability density function (PDF). Suppose there are D variables following a joint PDF $f(x_1, x_2, \dots x_D)$. Suppose further there are N observations of these variables, denoted here as D-dimensional vectors of the phase space $\mathbf{p}_i = ((p_i)_1, (p_i)_2, \dots (p_i)_D)$, $i = 1, \dots N$. Since the variables can have different units and vary across several orders of magnitude, it is useful to rescale them by dividing by their standard deviations. The resulting variables are dimensionless, and the rescaled observations are denoted $\widetilde{\mathbf{p}}_i, i = 1, \dots N$. The KDE method approximates the original distribution by placing a given kernel function at the exact positions of each observation and summing these functions over all data points. The estimator to the joint PDF $f(x_1, x_2, \dots x_D)$ is thus obtained as

$$\hat{f}(x_1, x_2, \dots x_D) = \sum_{i=1}^{N} w_i \left\{ \prod_{j=1}^{D} \frac{1}{h} K\left(\frac{x_j - (\widetilde{p}_i)_j}{h} \right) \right\}, \tag{27}$$

where $\frac{1}{h} K\left(\frac{x_j - (\widetilde{p}_i)_j}{h}\right) \equiv K_h(x_j, (\widetilde{p}_i)_j)$ is the kernel function and $w_i, i = 1, \dots N$ are a set normalised weights that can assign higher importance to certain observations if desired. While any positive definite and normalised function can be used as a kernel, the Gaussian is used in this thesis. The hyper-parameter h is called the bandwidth and may be considered akin to the standard deviation of the kernel function. If h is too small, the estimator will contain statistical noise while too large h will over-smoothen the distribution. In the more general approach called adaptive KDE, individual bandwidths h_i are applied for each data point. The selection of h_i is done in two steps. Firstly, seed bandwidths are generated for each data point using the k-nearest neighbours algorithm. The resulting vector $\mathbf{h}$ is then multiplied by a scale factor which is optimised using Maximum-Likelihood Cross-Validation. Further description of these methods can be found in Ref. [55]. Once the estimator is determined, an arbitrary number of particles can be sampled.

This thesis made use of KDSource [56] which features an implementation of adaptive KDE with an MCPL interface. The variables that are optimised in this thesis are taken to be

$$\mathbf{x} = (u, y, z, d_x, d_y, d_z), \tag{28}$$

where $u = \lg(E_0/E)$ is the lethargy, $E_0 = 10^3\,\mathrm{MeV}$ is a reference energy, and d_i are the fractional velocities in the Cartesian directions. One can assign higher importance to certain variables during bandwidth optimisation. In this work, the importances of the variables are set to be $(3, 0.1, 0.1, 3, 1, 1)$. The lethargy and d_x distributions were prioritised as these have the largest impact on the shielding (with d_x determining the polar angle with respect to the beamline axis which decides how far down the beamline the neutrons can propagate). The spatial distributions were deprioritised since the neutron flux is comparatively uniform on the beam port opening.

To assess the normalisation, it is useful to know how physical quantities are measured in PHITS. As an example, the volumetric flux F_i in a cell i is obtained as the weighted sum of all tracks ℓ_j inside the cell divided by its volume V_i, i.e.

$$F_i = \frac{\sum_{\ell_j \in i} w_j \ell j}{W V_i}, \tag{29}$$

where w_j is the weight of particle j and W is the total simulated weight. Since the proton source used $N = 3 \times 10^8$ protons, each of which has a weight of unity, fluxes in the proton run are given by

$$F_{\text{proton}} = \frac{L}{N V_i}, \tag{30}$$

where $L = \sum_{\ell_j \in i} w_j \ell j$. Suppose the original MCPL file contains a total simulated weight of W_1 and that the generated MCPL file contains M particles, each with a weight of unity. Then, assuming that the number of tracks scales with the simulated weight, the flux in a run from the generated MCPL file becomes

$$F_{\text{MCPL}} = \frac{L \cdot M/W_1}{M V_i} = \frac{L}{W_1 V_i}. \tag{31}$$

Hence, we can conclude that a factor W_1/N is required to rescale the normalisation to that of the proton run. Since $W_1 = 3.87 \times 10^5$, the normalisation becomes

$$1.56 \times 10^{16}\,\text{s}^{-1} \cdot \frac{3.87 \times 10^5}{3.0 \times 10^8} \approx 2.01 \times 10^{13}\,\text{s}^{-1}. \tag{32}$$

It was validated that this choice of normalisation indeed leads to equal neutron currents at the beam port opening. Finally, to investigate the validity of both the source term and the KDE source, the neutron fluxes were compared to those from a proton run. Comparisons were made at the monolith guide exit (5.5 m from the moderator) and the exit of the bunker guide (26 m from the moderator).

4.4 PHITS beamline simulation

The beamline simulations presented in this thesis have been performed with PHITS version 3.33. For neutron energies above 20 MeV, the intranuclear cascade model INCL-4.6 [59] is combined with the evaporation model GEM [35]. Below 20 MeV, nuclear data libraries from ENDF/B-VIII.0 [36] are used. Photon reactions are also modelled based on ENDF/B-VIII.0.

The first step before running the simulation is to define what information the software should record as the simulation progresses. In PHITS, this information is done using

so-called tallies. Perhaps the most important information to extract is dose maps of the full beamline. A volume fluence tally which records the particle flux in units of particles/(cm^2 · s) is therefore defined. This is done for cubic cells of volume $20 \times 20 \times 20$ cm^3. To calculate the radiation dose, it is necessary to convert the neutron and photon fluxes to an effective dose rate. Consistent with ESS guidelines [60], this thesis employs the whole-body conversion coefficients of ICRP 116 [61], assuming the worst-case irradiation geometry for each energy bin. These coefficients are shown in Figure 17(a). At ESS, the guidelines are such that the radiation dose rate on the surface of the shielding outside the bunker may not exceed 3 µSv/h (in so-called *supervised areas*) [62]. A safety factor of 2 is applied to account for systematic uncertainties in the Monte Carlo simulations, leading to an ultimate limit of 1.5 µSv/h [60].

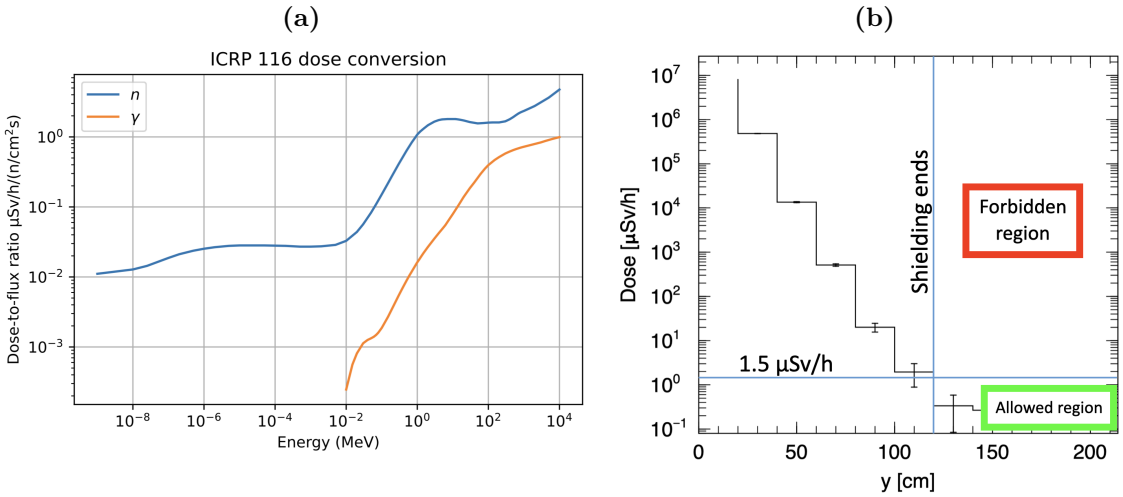

Figure 17: Panel (a): Worst-case flux-to-dose conversion coefficients of ICRP 116 for neutrons and photons. **Panel (b)**: A dose map projection at $x = 50$ m from the moderator. The relevant dose rate limit is indicated by the horizontal blue line.

Besides the full dose maps, calculated in the xy- and xz-planes (recall that x is the beamline direction and z is the height), one-dimensional projections of these maps were also computed at different points along the beamline. The critical point is then that the first $20 \times 20 \times 20$ cm^3 cell outside the shielding must be below the 1.5 µSv/h threshold. This principle is illustrated in Figure 17(b), showing a projection at $x = 50$ m for a simulation of the HIBEAM beamline.

Even with the neutron sources of Section 4.3, achieving low statistical uncertainties at the end of a long beamline and outside thick shielding layers remains computationally expensive. There is thus a need for further variance reduction techniques. This thesis has primarily applied a simple method known as geometry splitting. It is a way of increasing the relative computational effort in certain parts of the geometry. If a particle goes from a cell of importance I_1 to a cell of importance I_2, the incident particle is split, on average,

into I_2/I_1 particles (each carrying a fraction of the original statistical weight). If $I_2 < I_1$, a portion of the incident particles are removed from the simulation according to the same ratio. The geometry splitting technique allows the simulation to more quickly explore rare events, such as neutrons travelling through extensive shielding. In the simulations presented in Section 5.3, the shielding was divided into 10 layers, with each layer gaining an additional factor in importance. For the simulations with the source term, a factor of 2.5 was used. A slightly higher factor of 3.0 was used with the kernel density estimation to compensate for a lower number of input particles.

4.5 Geant4 detector simulation

To estimate the spallation background of various particle species in the detector, a surface tally was placed at the entrance to the experimental cave in the PHITS geometry and all crossing particles were dumped into an MCPL file. This file was used as direct input to a more detailed detector model in Geant4.

The Geant4 model used in this thesis was developed by the author and M. Holl and is shown in Figure 18. The geometry is constructed using the `TGeo` classes of ROOT [57] and converted into Geant4 objects with the Virtual Geometry Model (VGM) conversion tool [63]. Each of the over 1000 CsI(Na) scintillator crystals is individually modelled. Their dimensions and that of the iron yoke were obtained from a previous model developed for the WASA-FRS experiment [64]. The annihilation target was modelled as a 100 µm thick, 40 cm diameter circular graphite foil which is contained in a 5 mm thick aluminium vacuum vessel. The TPC was modelled as a cylindrical shell with an 80% Ar/20% CO_2 gas mixture surrounding the beampipe. The passive shield and cosmic veto were given the same dimensions and material composition as in PHITS. Geant4 models were developed for both $n - \bar{n}$ and $n - n'$ oscillation configurations and are shown in Figures 18(a) and 18(b), respectively. However, this thesis focuses on the former case as there should ideally be no spallation background in the latter.

The main physics list used for the simulation is `G4HadronPhysicsINCLXX` with the Neutron-HP package turned on. This means that INCL is used at high energies (> 20 MeV) while evaluated cross-sections are used below 20 MeV, similar to the PHITS configuration. The Geant4 default nuclear library G4NDL4.7 [65] is used. The electromagnetic interactions are simulated using the `G4EmStandardPhysics_option4` list. The `G4EmExtraPhysics` list is also activated to treat photonuclear reactions [66].

Using the Geant4 model, the flux of neutrons, photons, electrons and positrons in the TPC and calorimeter can be estimated. To score the flux in arbitrary volumes, a calculation was implemented mimicking that of PHITS (consult Eq. (29) in Section 4.3.2). An important remark is that the information on the total simulated weight W is not known from the MCPL file alone and therefore must manually be recorded from the PHITS simulation for proper normalisation.

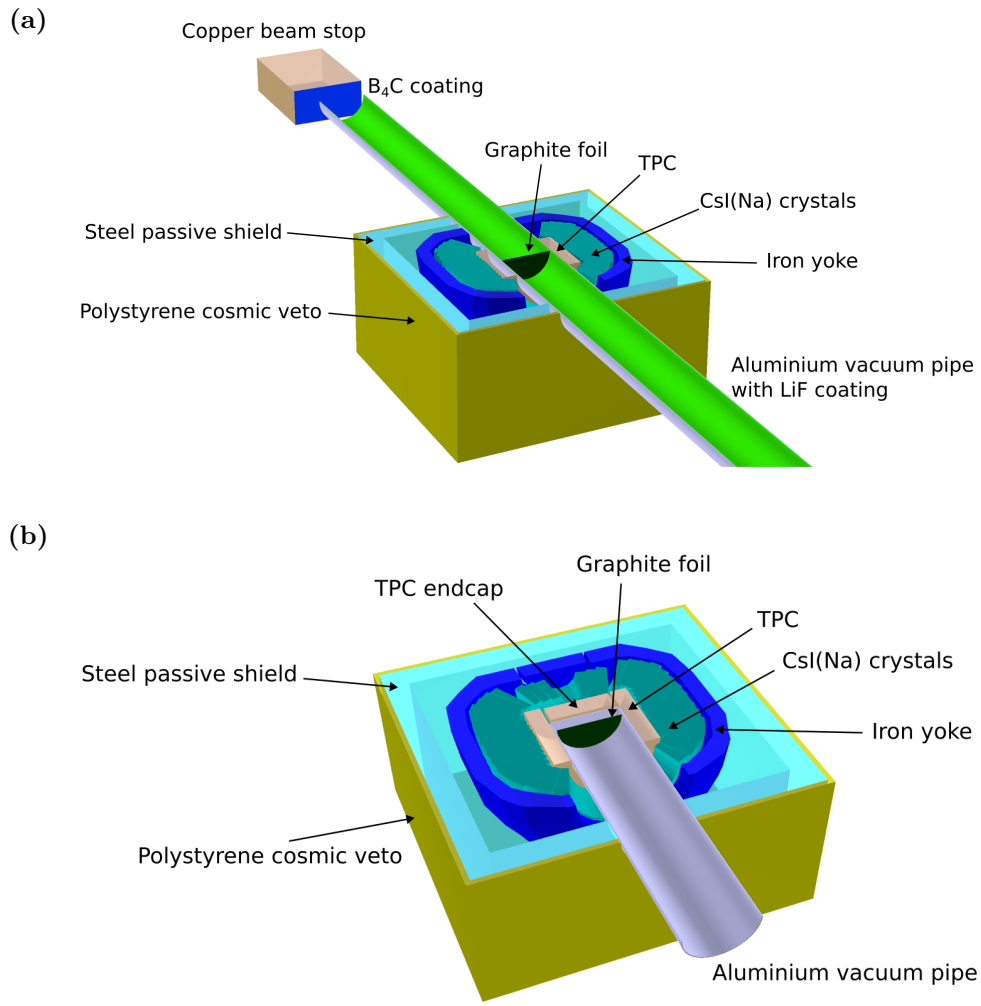

Figure 18: Geometric detector models built using ROOT's `TGeo` classes which are used as input for the Geant4 simulation. Panel (a) shows a setup for $n - \bar{n}$ oscillations while Panel (b) shows a setup for $n - n'$ oscillations.

In addition to the flux, the energy and time distribution of the particles were extracted for the annihilation target, TPC and WASA calorimeter and outputted in the form of ROOT histograms. The potential application of a LiF cladding layer was investigated. Analogous simulations were also performed in PHITS with the EGS5 [67] option turned on, enabling the coupled transport of electrons and photons. This allowed for rudimentary benchmarking of the two codes. For the PHITS simulations, please note that an energy cut-off of 10^{-2} MeV and 10^{-3} MeV is applied for electrons/positrons and photons, respectively.

5 Results and analysis

5.1 Neutron source construction

In this section, the results from the production and validation of the source term and KDE particle generator are presented. As described in Section 4.3, all neutrons entering the monolith insert were written to an MCPL file. The (statistically weighted) energy and polar angle with respect to the beamline axis were determined for each neutron. The resulting distributions are indicated in Figures 19(a) and 19(b). Shown in the same plot are the distributions obtained from the KDE particle generator.

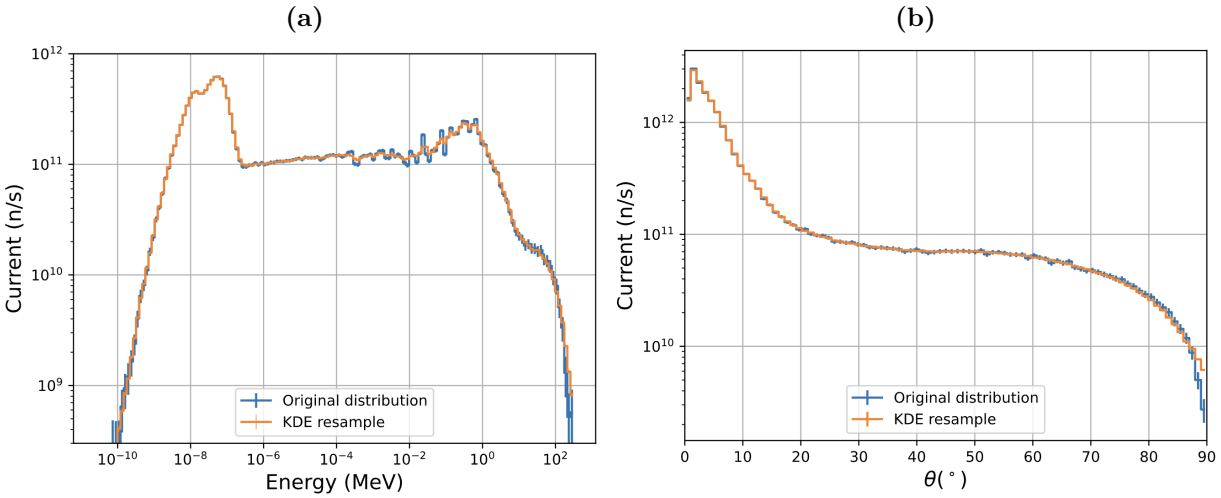

Figure 19: Spectra showing the neutron currents at the HIBEAM beam port, 2 m from the moderator. **Panel (a)**: Energy spectrum. **Panel (b)**: Angular spectrum in terms of the polar angle with respect to the beamline axis.

The energy spectrum shows one peak in the thermal region (1 Å or 8×10^{-8} MeV) and another in the cold region (around 2.5 Å or 1.3×10^{-8} MeV). This is expected, as these peaks come from the light water and parahydrogen moderators, respectively (see Section 3.2). The spectrum is relatively constant for intermediate-energy neutrons, with a smaller peak in the MeV region before dropping off at a little above 10^2 MeV. Considering the high-energy region of the spectrum is what gives the largest dose contribution, it is interesting to compare it with results obtained for other beamlines at the ESS in Ref. [58]. Such comparison indicates that the HIBEAM spectrum is softer than that of the NMX, CSPEC and DREAM beamlines. This can be explained by the fact that these beamlines are in the forward direction, opposite from where the proton beam hits. On the other hand, the spectrum measured here closely matches that of LOKI, which is on the N7 beamline (equivalent to E7 but in the north sector). This follows from the similar positioning relative to the incident proton beam.

The KDE resample follows the original distribution very closely across a wide range of energies and polar angles. Some differences can be noted where the original distribution has sudden changes, such as in the energy region 10 keV - 1 MeV, where the KDE resample tends to average out over these fluctuations. Importantly for the shielding calculations, very good agreement in the high-energy region (1 MeV - 100 MeV) is seen. Some deviations can also be noted at the tail of the distribution, where the KDE resample tends to slightly overestimate the distribution although not by much more than the statistical uncertainty of the original distribution. A similar observation can be made at polar angles close to 90° but this does not affect the shielding since these neutrons will not travel far into the beamline. Such boundary effects are a known problem of KDE resampling, though mitigating efforts such as the application of finite support kernels are possible (see Ref. [68]).

The correlations between energy and polar angle for the original distribution are indicated in Figure 20(a). One interesting feature of the histogram is that the cold neutrons only seem to contribute significantly at small polar angles ($\theta \lesssim 5°$). The likely explanation for this is that these neutrons have been slowed down by the moderator and therefore cannot enter the monolith at large polar angles due to the spatial extent of the moderator. Looking more closely at the small polar angles in Figure 20(b), we can see that the cold peak is most pronounced around 0° and 4°, corresponding to neutrons from the far and close wings of the moderator (see Figure 7(a)). On the other hand, thermal and high-energy neutrons can scatter in the target-moderator system and the monolith itself before finally entering the beam port, thus explaining the much wider polar-angle distribution.

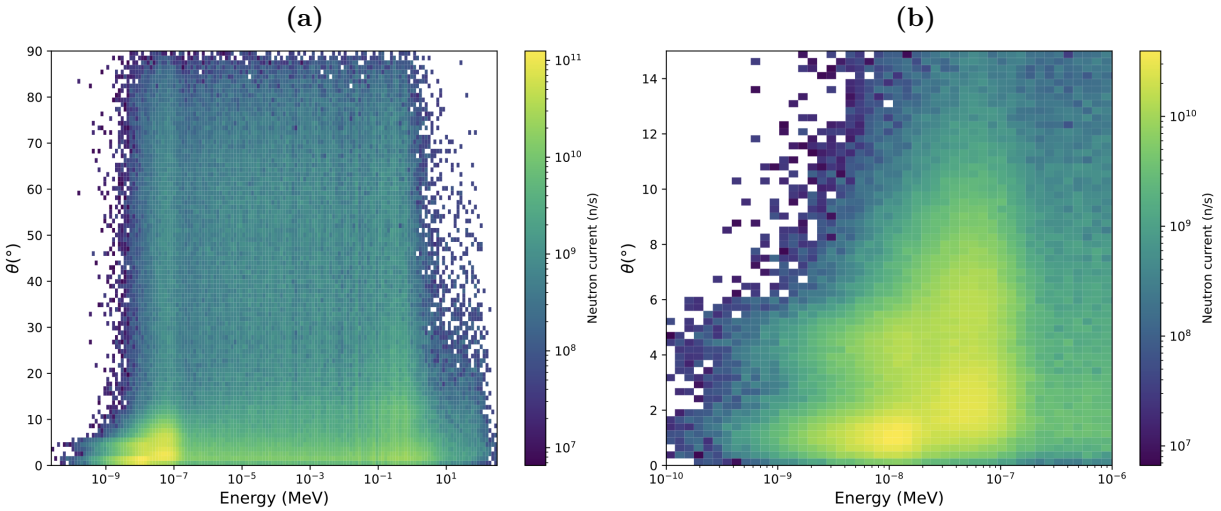

Figure 20: A 2D histogram showing correlations between neutron energy and the polar angle with respect to the beamline axis sampled at the HIBEAM beam port. **Panel (a)**: Full spectrum. **Panel (b)**: Enlarged view of low-energy neutrons at small polar angles.

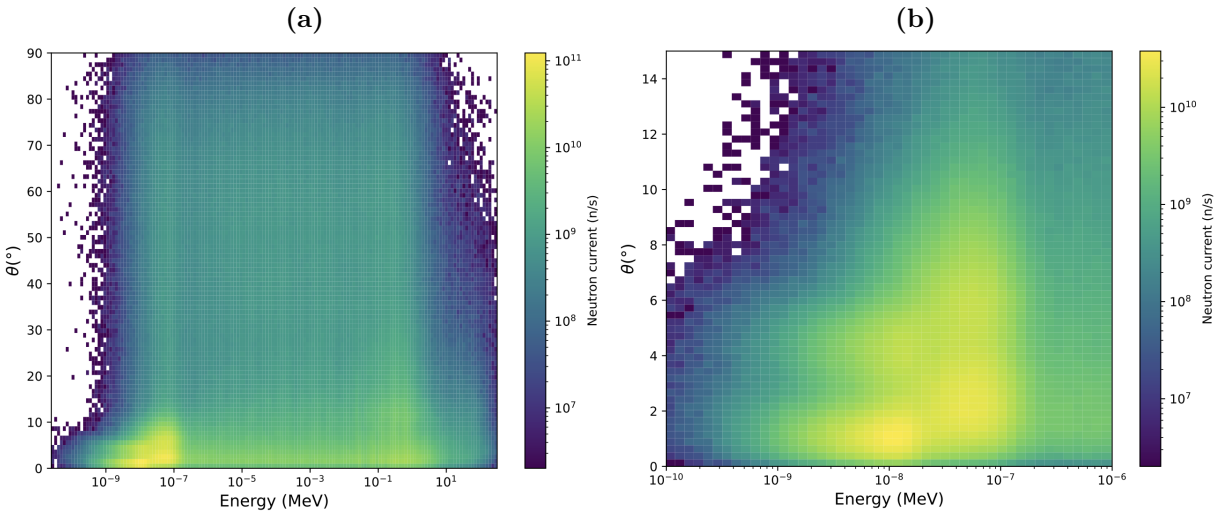

Figure 21: A 2D histogram showing correlations between neutron energy and the polar angle with respect to the beamline axis obtained from KDE resampling. **Panel (a)**: Full spectrum. **Panel (b)**: Enlarged view of low-energy neutrons at small polar angles.

Figure 21 shows the corresponding energy-angle distribution obtained from KDE resampling. No notable differences, besides the overall higher statistics in the KDE resampling, are evident, suggesting that the method faithfully reproduces the original distribution. The KDE resampling and the PHITS source term were further validated by considering the surface flux at two points along the beamline, namely the exit of the monolith guide (5.5 m from the moderator) and the exit of the bunker guide ($\sim$ 26 m from the moderator). These fluxes, along with those from the original proton source run, are indicated in Figures 22 and 23. The ratios with respect to the proton run are also indicated below the flux histograms.

It is seen that the KDE method faithfully reproduces the neutron flux spectrum observed in the proton run. Meanwhile, the source term methodology overestimates the flux of neutrons above thermal energies, particularly at 5.5 m from the monolith exit. This is likely caused by the geometrical simplifications of the source term. For example, the source term assumes that the neutron flux is azimuthally symmetric around the beamline axis. This is not strictly true due to the shape of the moderator giving an asymmetric distribution of low-energy neutrons in the horizontal plane, as well as the spallation target placed below the moderator giving an asymmetric distribution of high-energy neutrons in the vertical plane. The study of the LOKI source term (on the similarly placed N7 beamline) in Ref. [58] also indicates an overestimation of the neutron fluxes at this distance, although for that beamline the overestimation was seen across the full energy range. It is probable that the agreement seen in this work for the cold and thermal neutrons is a consequence of the neutron supermirrors which significantly increase the angular acceptance of neutrons in this energy range, reducing the sensitivity to azimuthal anisotropies.

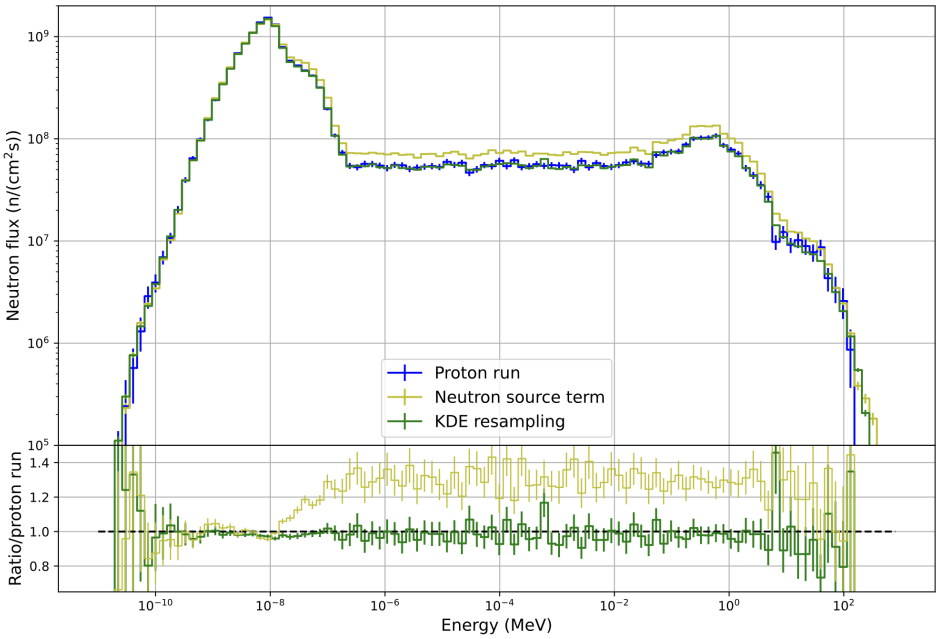

Figure 22: Neutron fluxes obtained from runs employing a proton source, the neutron source term and KDE resampling. The fluxes are measured at the exit of the monolith guide, 5.5 m from the moderator.

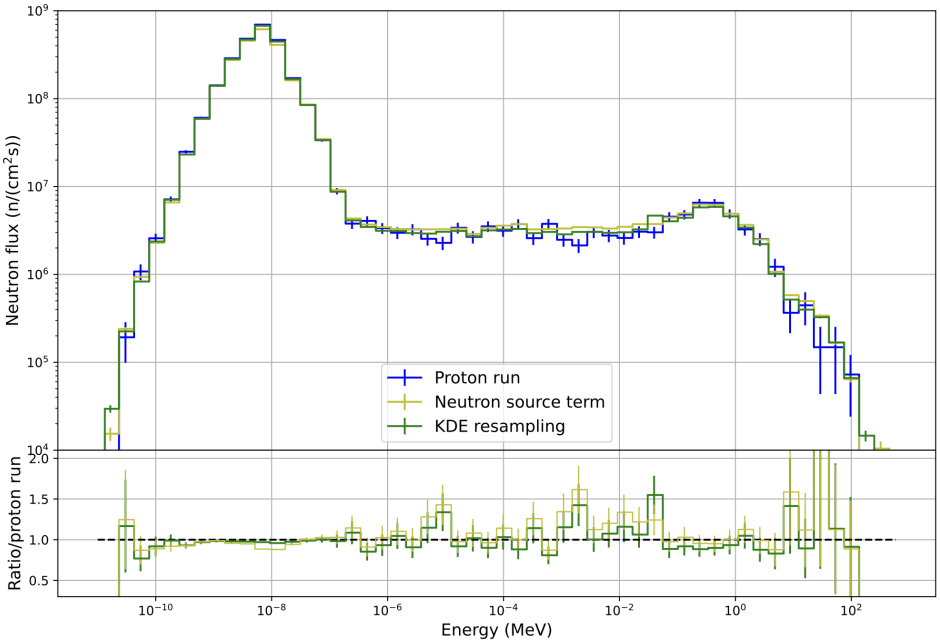

Figure 23: Neutron fluxes obtained from runs employing a proton source, the neutron source term and KDE resampling. The fluxes are measured at the exit of the bunker guide, 26 m from the moderator.

Historically, correction factors have been applied such that the high-energy neutron fluxes from the source term agree with that from the proton run. While a correction factor of 0.8 could be applied to the source term to make the fluxes agree at 5.5 m, this seems to give too low fluxes at 26 m (around which the beamline shielding is placed). To be conservative, no correction factor is applied. With the KDE method, no correction factor is deemed necessary, as the agreement is satisfactory at both distances.

5.2 Beam stop shielding simulations

In this section, a brief overview of the beam stop shielding simulation results is provided. Further results are given in Appendix B and in report ESS-5286512 [1]. Shown here are the results corresponding to Figure 16. The dose maps along with their associated statistical uncertainties are shown in Figures 24 and 25 for the xy- and xz-planes, respectively. The plotted contours correspond to 10^4 µSv/h, 10^3 µSv/h, 10^2 µSv/h, 10^1 µSv/h, 1.5 µSv/h (in red) and 10^{-1} µSv/h.

As is evident from Figures 24 and 25, this shielding configuration, with outer beam stop dimensions of $3.5 \times 3.0 \times 2.93\,\mathrm{m}^3$ (length × width × height), satisfies the 1.5 µSv/h dose rate threshold on all shielding surfaces. This investigation was repeated for all other beam stop configurations, shown in Appendix B. One conclusion is that the radiological worst-case scenario corresponds to a configuration without any vacuum pipe. This is not surprising, since a vacuum pipe restricts the solid angle that can be occupied by the beam, in effect leading to scattering inside the bunker which reduces the number of neutrons reaching the beam stop. Furthermore, it was found that moving the B_4C layer downstream had minimal impact on the observed dose rates on the shielding surface. This is likely because B_4C primarily stops the low-energy neutrons which anyhow give only a minor contribution to the dose.

It was further determined that the installation of shielding plugs in the bunker enabled a significant reduction in the size of the beam stop. For a configuration with a downstream bunker plug only, reduction to outer dimensions of $1.8 \times 3.0 \times 2.83\,\mathrm{m}^3$ is possible, while for simulations with both downstream and upstream plugs, further reduction to $1.2 \times 1.8 \times 2.53\,\mathrm{m}^3$ can be allowed.

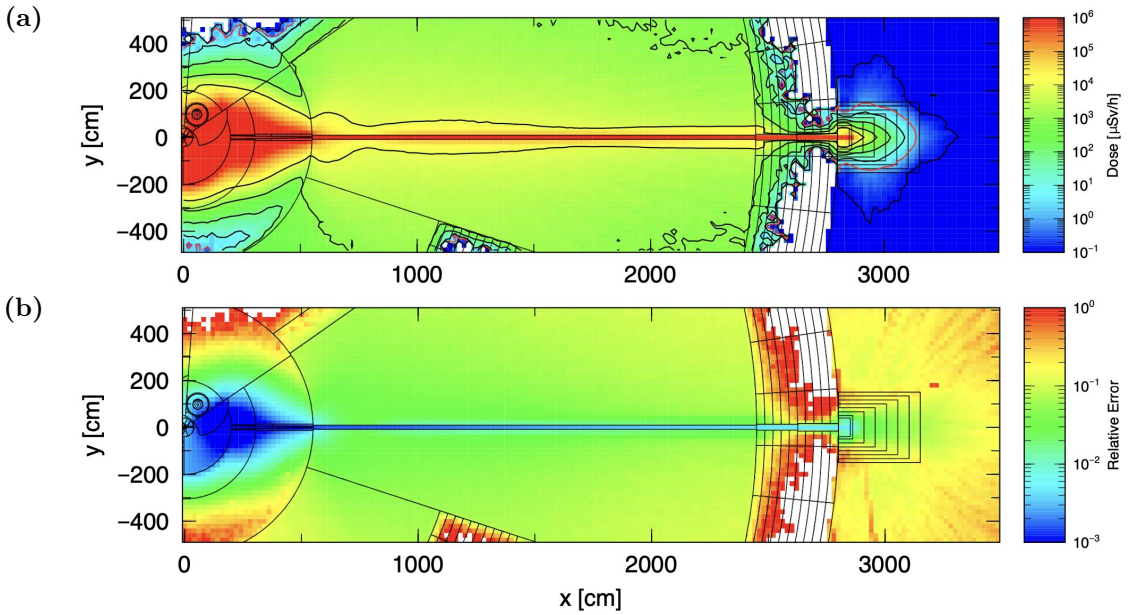

Figure 24: Panel (a): Dose map in the xy-plane for the temporary beam stop configuration corresponding to Figure 16. The 1.5 μSv/h dose rate threshold is indicated by a red contour. The simulation employs the CSPEC source term at 0.5 MW. **Panel (b)**: Statistical uncertainties associated with Panel (a).

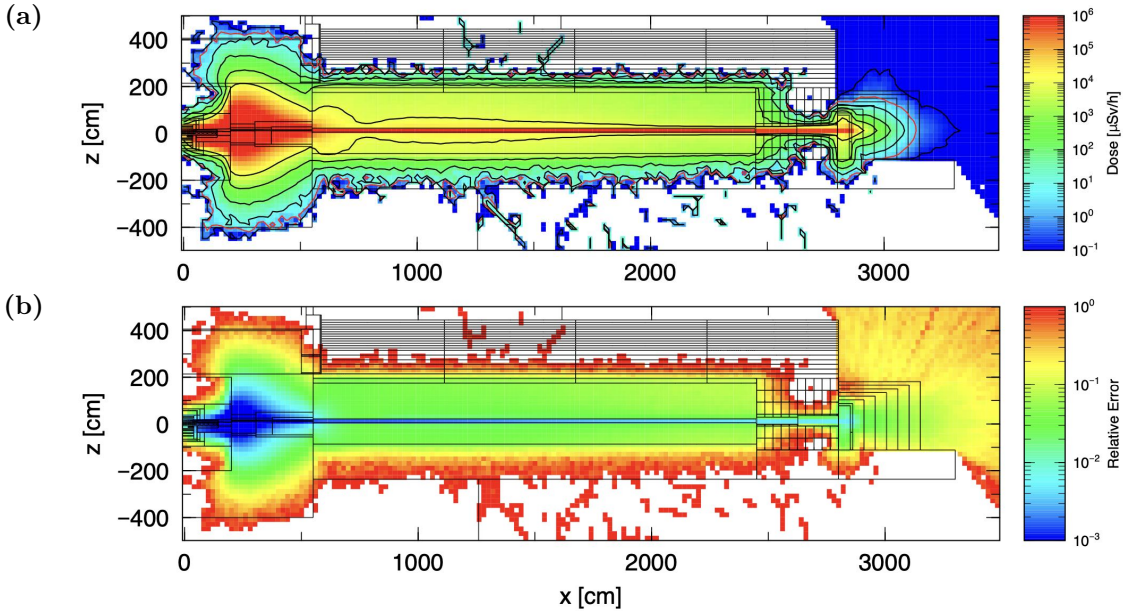

Figure 25: Panel (a): Dose map in the xz-plane for the temporary beam stop configuration corresponding to Figure 16. The 1.5 μSv/h dose rate threshold is indicated by a red contour. The simulation employs the CSPEC source term at 0.5 MW. **Panel (b)**: Statistical uncertainties associated with Panel (a).

5.3 HIBEAM beamline shielding simulations

In this section, results from the HIBEAM beamline simulations are provided. We commence with a brief description of the impact of neutron focussing, simulated here using supermirror surfaces in the neutron guides. The guide greatly amplifies the fluxes of cold neutrons, as evident from Figure 26, showing the neutron flux inside the annihilation target without and with the supermirror surface activated, in blue and yellow respectively. In these two cases, a pure copper substrate is assumed. Note that the KDE source is used unless otherwise noted. As can be seen in the figure, the flux of cold neutrons inside the target increases by over one order of magnitude with the supermirror surface. In the third configuration shown in green, 2 µm of Ni and 2 µm of Ti are placed outside the supermirror surface. This marginally reduces the cold flux due to neutron capture in the thin coating (the impact of such thin layers has also been experimentally observed, see e.g. Ref. [69]).

Let us move on to the consequences of the guides for the shielding. While the guide only had a slight impact on the required shielding close to the bunker (where the high-energy neutrons are the dominant dose contributor), the guide substantially increased the dose rates around the cave. The largest difference was seen in the dose rate from γ rays, which stems primarily from capture reactions of the cold neutrons in the aluminium vacuum pipe. In fact, the guides make the γ rays the dominant contributor to the dose rates outside the cave. Figure 27 shows a comparison of the γ-ray dose rates observed around the experimental cave for simulation with and without the supermirror surface being activated. It is evident that the effect of the guides needs to be considered to not underestimate the required amount of shielding.

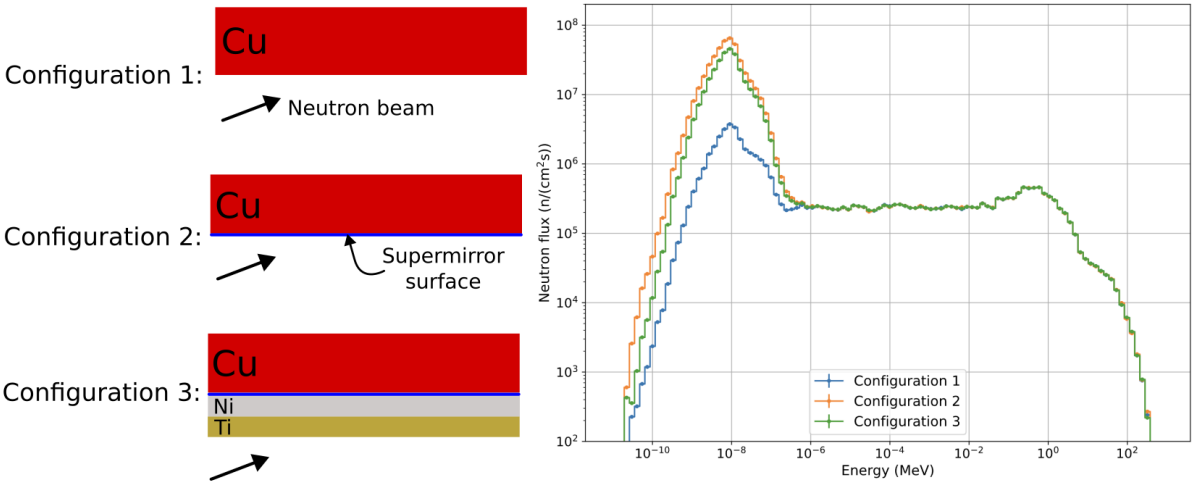

Figure 26: Neutron fluxes in the annihilation target with and without the neutron supermirror surface, as well as with an added Ni/Ti layer outside the supermirror surface. The thickness of the Ni/Ti layer is exaggerated for clarity.

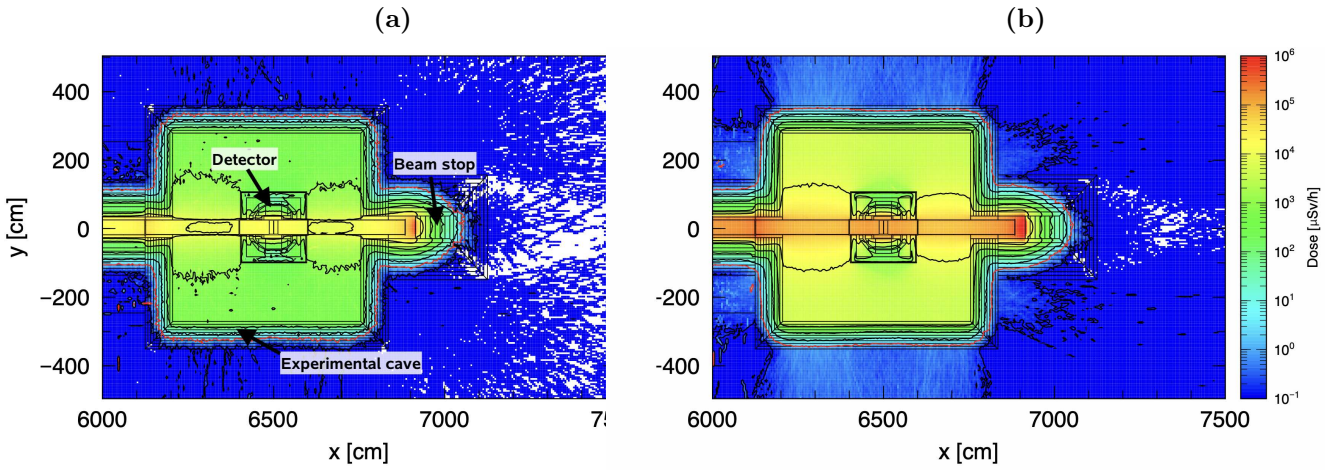

Figure 27: Dose rates from γ rays in the experimental cave as obtained (a) without and (b) with the supermirror surface activated. This corresponds to Configurations 1 and 2 in Figure 26.

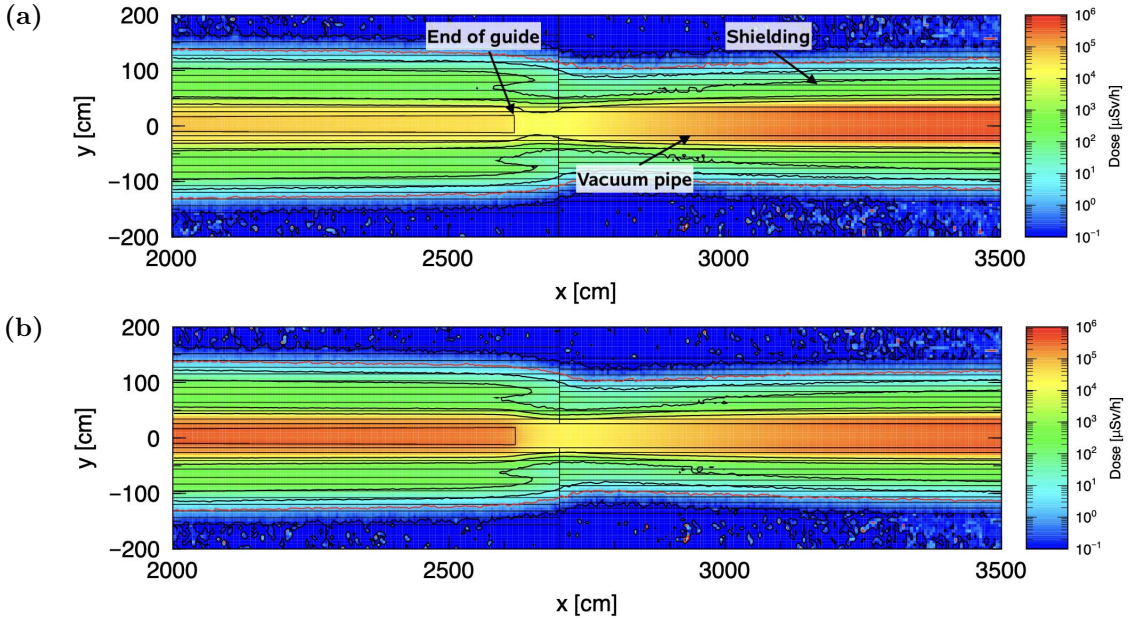

Figure 28: Dose rates from γ rays in the central part of the beamline as obtained (a) without and (b) with Ni/Ti coating outside the supermirror surface. This corresponds to Configurations 2 and 3 in Figure 26.

As was seen in Figure 26, the thin Ni/Ti coating on the guide leads to a non-negligible absorption of low-energy neutrons. Figure 28 shows a comparison of the γ-ray doses in the central part of the beamline (around the end of the bunker guide) with and without the presence of the Ni/Ti layer. In both cases, the supermirror surface is activated. The

neutron absorption in the Ni/Ti layer is reflected by the increased dose rates around the guide. However, the overall need for shielding is unaffected as the dose contribution from high-energy neutrons is dominant in this part of the beamline. Another interesting observation from Figure 28(b) is that while the γ-ray dose rate decreases after the guide, it begins to increase further down the beamline. In this case, the explanation is that neutrons which are not focussed onto the target instead hit the inner surface of the vacuum pipe, again leading to neutron capture.

Let us now turn to discuss the full simulation results, which are presented in the following pages. The configuration considered here features 45 cm of steel and 85 cm of heavy concrete in the first 12 m outside the bunker. In the remaining section up to the experimental cave, it is reduced to 30 cm of steel and 80 cm of heavy concrete. The heavy concrete walls of the experimental cave have a thickness of 80 cm. The beam stop has a length of 1 m of copper with the heavy concrete walls behind the copper having 1.1 m thickness and the walls on the side 1.2 m thickness.

Note that in all simulations, the configuration with supermirror surfaces and Ni/Ti coating is used. Figures 29 and 30 show the total dose rates (neutrons and photons) in the xy- and xz-planes, respectively, obtained from runs employing the neutron source term. Figures 31 and 32 show the corresponding results obtained using KDE resampling. The dose maps separating the neutron and γ-ray contributions are provided in Appendix C.

Both sets of simulations indicate that the present configuration is sufficient to pass the 1.5 µSv/h dose rate threshold on all shielding surfaces. There are still some statistical fluctuations marginally exceeding the dose rate threshold, but given the dose rate in the neighbouring regions, these will likely disappear when running with even higher statistics. Currently, the source term simulation uses around 5 billion events, while the KDE resampling uses 1 billion events (a higher importance gradient is used for the latter as compensation). Besides the long computation times, one thing hindering using more primary particles for the KDE resampling is file size limitations. For context, 1 billion particles take up around 25 GB in MCPL format, and over 100 GB as PHITS dump files.

On average, the two simulations indicate very similar radiation levels in the whole beamline. It seems however that the source term predicts slightly higher average dose rates (on the order of $\sim 10\%$), especially close to the bunker. This is likely a direct consequence of the flux overestimation relative to the KDE method described by Figure 22 in Section 5.1.

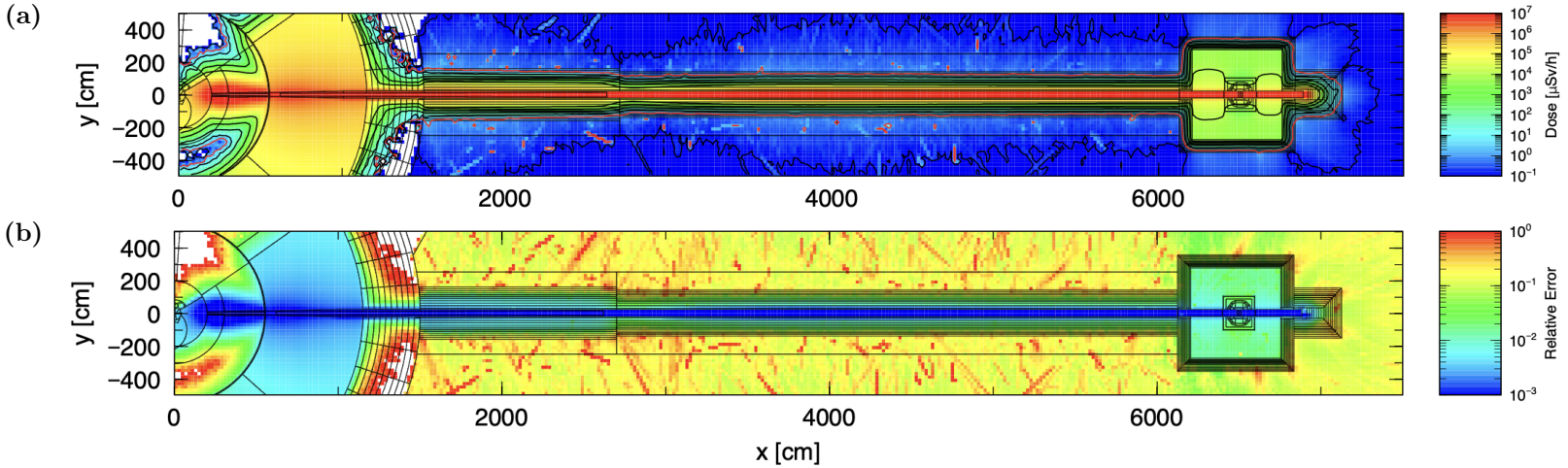

Figure 29: Panel (a): HIBEAM beamline simulation in the xy-plane with the neutron source term. **Panel (b)**: Statistical uncertainty associated with Panel (a).

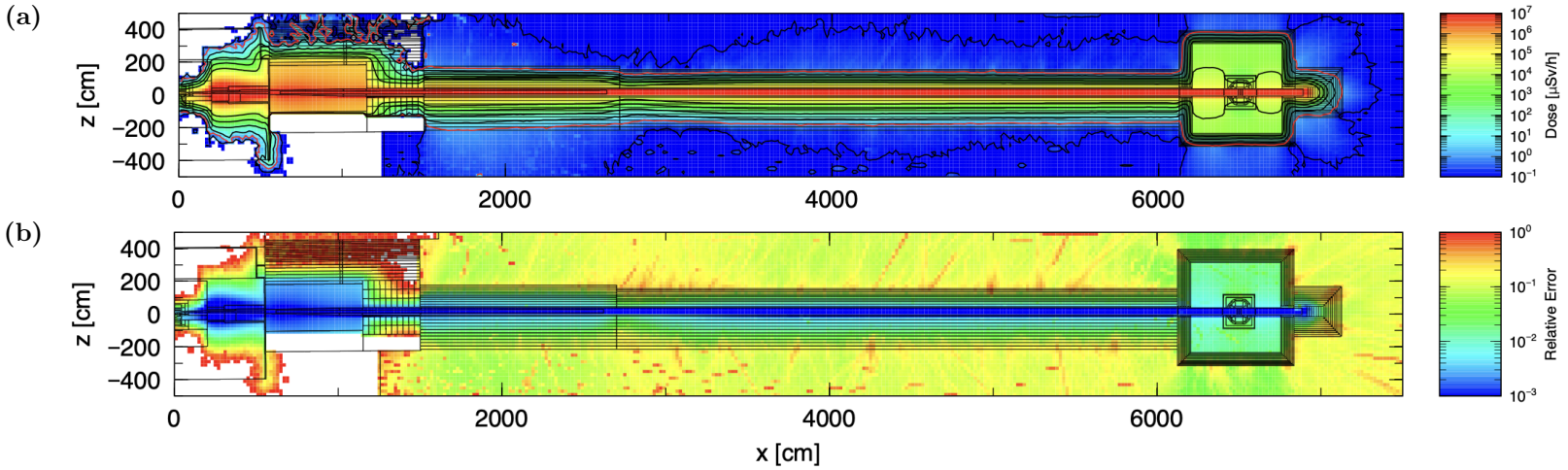

Figure 30: Panel (a): HIBEAM beamline simulation in the xz-plane with the neutron source term. **Panel (b)**: Statistical uncertainty associated with Panel (a).

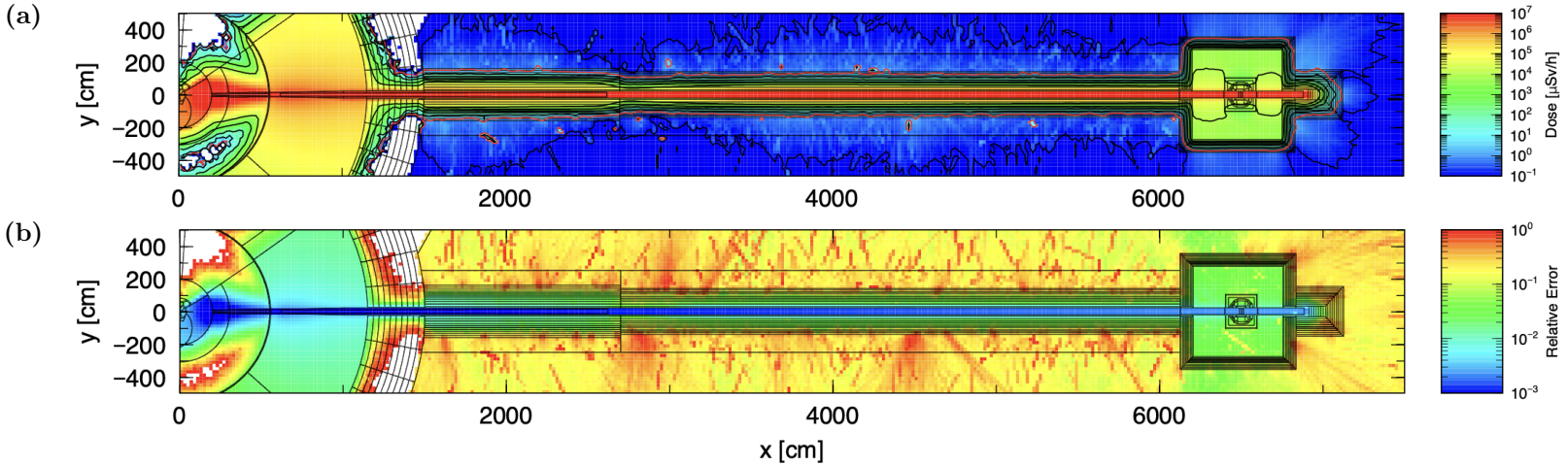

Figure 31: Panel (a): HIBEAM beamline simulation in the xy-plane with KDE resampling. **Panel (b)**: Statistical uncertainty associated with Panel (a).

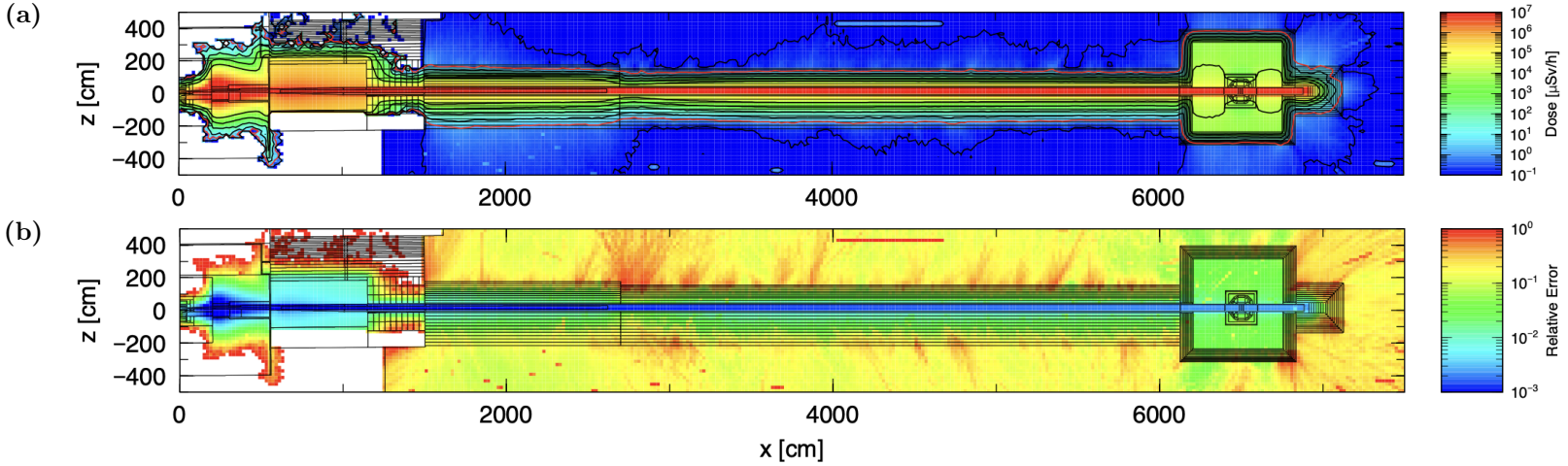

Figure 32: Panel (a): HIBEAM beamline simulation in the xz-plane with KDE resampling. **Panel (b)**: Statistical uncertainty associated with Panel (a).

5.4 Detector simulations

As outlined in Section 4.5, the fluxes of neutrons, photons, electrons and positrons were calculated within the annihilation target, TPC and WASA calorimeter. One simulation made use of PHITS with the EGS5 option turned on, while the other made use of the Geant4 detector model. In both cases, the MCPL file generated at the experimental cave entrance was used as the particle source (with around 2.5×10^8 particles). We begin by presenting results for the baseline configuration with a 5 mm aluminium vacuum vessel. The fluxes obtained from the two simulation codes in the annihilation target, TPC and WASA calorimeter are shown in Figures 33-35. The integrated fluxes are listed in Table 1.

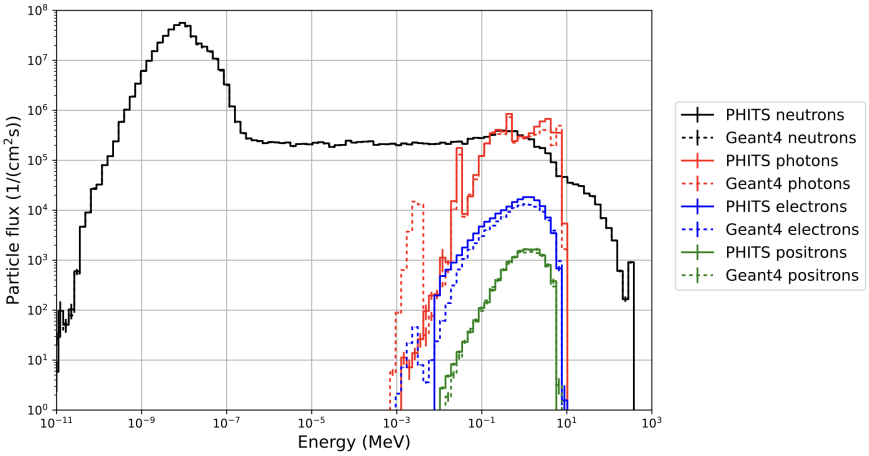

Figure 33: Neutron, photon, electron and positron flux due to spallation background in the annihilation target, as calculated by PHITS and Geant4, in a configuration with a 5 mm aluminium vacuum vessel. The neutron fluxes coincide across the energy spectrum.

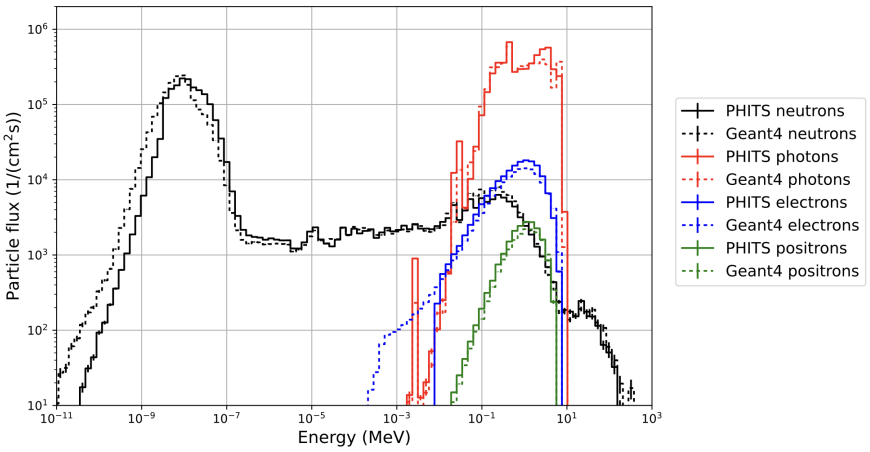

Figure 34: Neutron, photon, electron and positron flux due to spallation background in the TPC, as calculated by PHITS and Geant4, in a configuration with a 5 mm aluminium vacuum vessel.

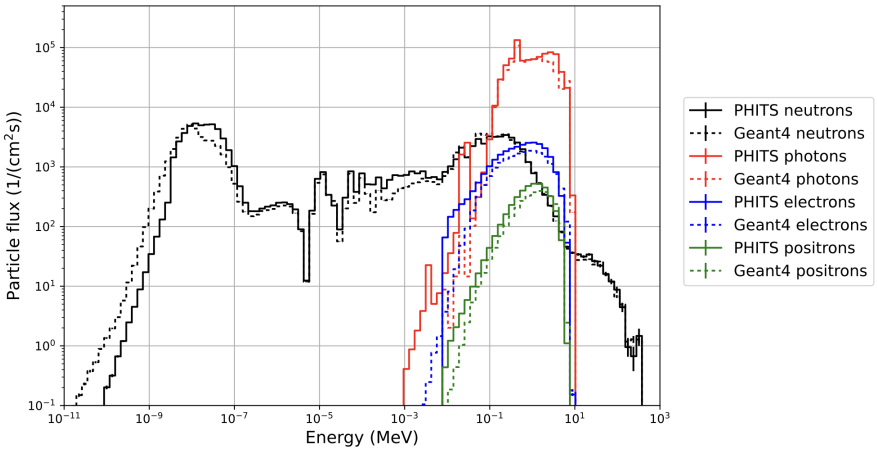

Figure 35: Neutron, photon, electron and positron flux due to spallation background in the WASA calorimeter, as calculated by PHITS and Geant4, in a configuration with a 5 mm aluminium vacuum vessel.

Table 1: Integrated particle fluxes, in units of particles/(cm$^2\cdot$ s), as calculated by PHITS and Geant4, in different detector subsystems. The average and sample standard deviation are also indicated. The statistical uncertainties of the simulations are negligible ($< 1\%$) in relation to systematic uncertainty. The vacuum vessel consists of 5 mm of aluminium.

Volume	Simulation	n	γ	e^-	e^+
Target	PHITS	4.13×10^8	6.2×10^6	1.7×10^5	1.27×10^4
	Geant4	4.07×10^8	5.2×10^6	1.2×10^5	1.17×10^4
	Average	$4.10(5) \times 10^8$	$5.7(7) \times 10^6$	$1.4(3) \times 10^5$	$1.22(7) \times 10^4$
TPC	PHITS	1.81×10^6	5.3×10^6	1.7×10^5	1.9×10^4
	Geant4	1.83×10^6	4.8×10^6	1.4×10^5	1.6×10^4
	Average	$1.82(2) \times 10^6$	$5.1(3) \times 10^6$	$1.6(2) \times 10^5$	$1.8(2) \times 10^4$
WASA	PHITS	9.9×10^4	8.6×10^5	2.7×10^4	3.9×10^3
	Geant4	8.9×10^4	7.0×10^5	2.0×10^4	3.0×10^3
	Average	$9.4(7) \times 10^4$	$7.8(11) \times 10^5$	$2.3(5) \times 10^4$	$3.5(6) \times 10^3$

Firstly, we note that the neutron spectra seen in the annihilation target are nearly identical for the two simulations. This is expected since the neutrons hitting the target are mainly coming from the direct beam and thus not affected by the simulation specifications. It also indicates that the normalisation procedure is correct. The photon, electron and positron spectra agree fairly well between the two codes, though some differences can be noted. Firstly, we see a significant number of keV-range photons in Geant4 which are absent in PHITS. These photons stem from inelastic neutron scattering in the B_4C layer in the beam stop, a production channel which is evidently not described by the PHITS libraries. Another difference can be seen in the treatment of low-energy electrons. In both the target and WASA, the low-energy electron fluxes calculated by PHITS are slightly higher

than those of Geant4 (recall that the cut-off at 1×10^{-2} MeV for PHITS is caused by the simulation settings). In the TPC, the two simulations agree well for all particle types, although some difference can be noted in the cold neutron tail where Geant4 estimates a higher flux. A similar trend can be seen for the WASA calorimeter. This may be caused by the usage of different nuclear data libraries.

The energy-time correlations of the different particle species, where the time is measured from the neutrons entering the beam port (see Section 4.3), are indicated in Figure 36 for the WASA calorimeter. As expected, the high-energy neutrons arrive much earlier than the cold neutrons. We see that the large background contribution of photons, electrons and positrons is associated with the cold peak and thus arrives after around ∼0.1 s. While the flux contribution per bin is relatively constant at earlier times, this is due to the logarithmic time bins. If considering the instantaneous flux, it is highest after around 1 µs. It can also be interesting to study the physical origin and physics processes which contribute to the particle flux in the detector systems. Of particular importance, owing to pile-up sensitivity, are the electrons in the TPC and the photons in the WASA calorimeter. The flux contributions, subdivided into originating volume and originating physics process, are shown in Figure 37. For the electrons in the TPC, the largest contribution comes from Compton scattering in the vacuum pipe, closely followed by Compton scattering in the calorimeter (which is further away from the beam but has a much greater volume). Meanwhile, we can see that the large contribution to the photon flux comes from neutron capture, with some contribution also from positron annihilation and bremsstrahlung.

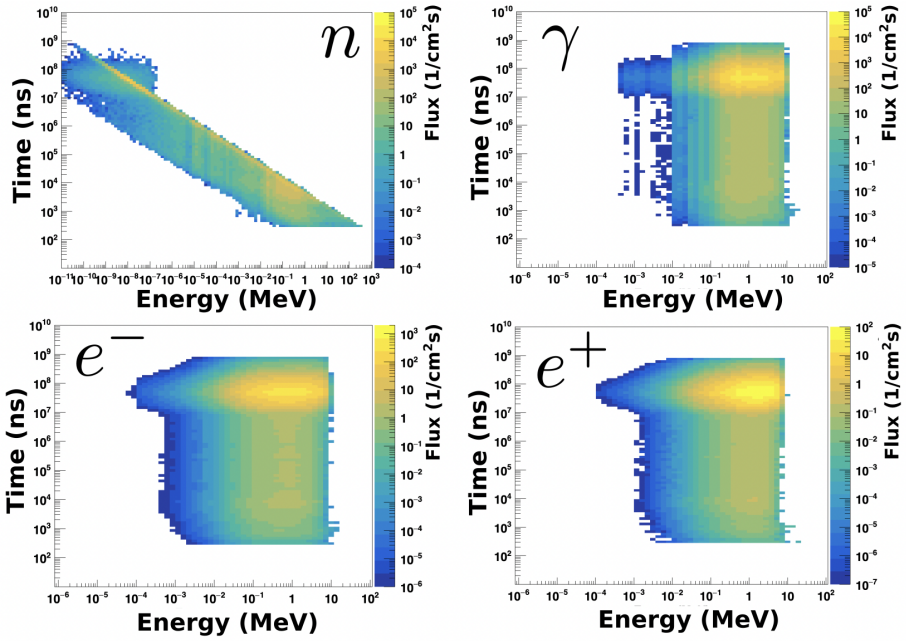

Figure 36: Energy-time correlations of the spallation background in WASA for a 5 mm Al vacuum vessel. Results are obtained from Geant4 simulation.

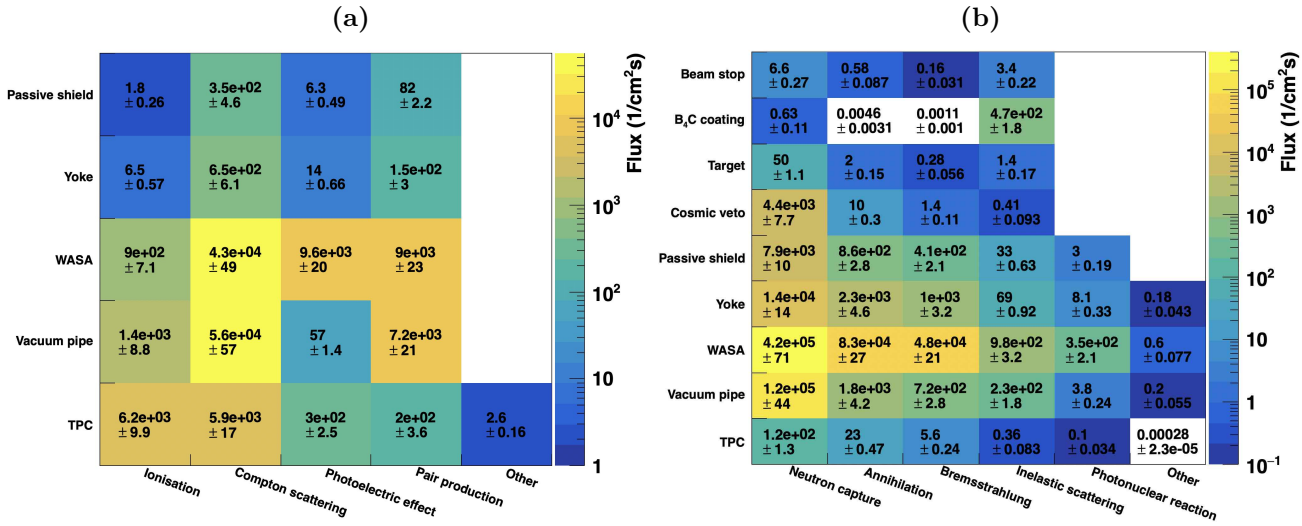

Figure 37: The particle flux in particles/(cm^2· s), subdivided into originating volume on the vertical axis and originating physics process on the horizontal axis. The results are obtained from Geant4 simulation. The shown uncertainties are statistical. **Panel (a):** For electrons in the TPC. **Panel (b):** For photons in the WASA calorimeter.

Already from these results, it is clear that cold neutrons are being captured in the vacuum pipe or scattering into the detector. This results in a high flux of photons which also yield electrons through secondary electromagnetic interactions. One possible solution to counteract this effect is to cover the inner surface of the vacuum vessel with a neutron poison such as LiF. Figures 38-39 show corresponding fluxes in the TPC and WASA with an added 5 mm layer of LiF, again featuring a comparison of the results obtained from PHITS and Geant4. The integrated fluxes are given in Table 2. The energy-time correlations in WASA are provided in Figure 40, where the same colour scale is used as for the previous configuration in Figure 36 for easier comparison.

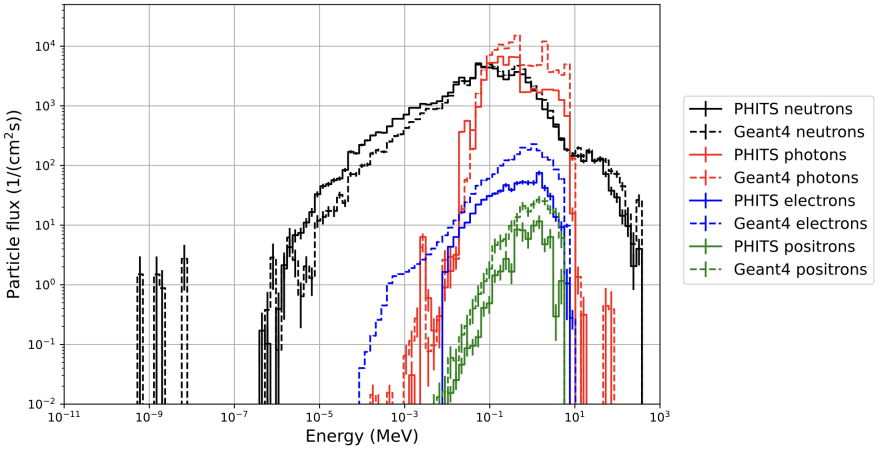

Figure 38: Neutron, photon, electron and positron flux due to spallation background in the TPC, as calculated by PHITS and Geant4, in a configuration with a 5 mm aluminium vacuum vessel and 5 mm LiF cladding.

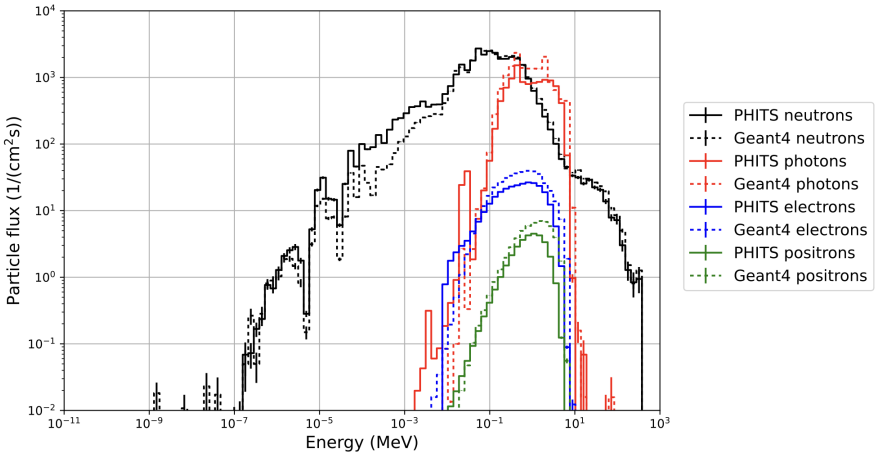

Figure 39: Neutron, photon, electron and positron flux due to spallation background in the WASA calorimeter, as calculated by PHITS and Geant4, in a configuration with a 5 mm aluminium vacuum vessel and 5 mm LiF cladding.

Table 2: Integrated particle fluxes, in units of particles/(cm^2· s), as calculated by PHITS and Geant4, in different detector subsystems. The average and sample standard deviation are also indicated. The statistical uncertainties of the individual simulations are stated when non-negligible ($> 1\%$) and included in the overall error for the average (added in quadrature). The vacuum vessel consists of 5 mm of aluminium and 5 mm of LiF.

Volume	Simulation	n	γ	e^-	e^+
Target	PHITS	4.11×10^8	4.6×10^5	$6.6(1) \times 10^3$	$1.2(1) \times 10^3$
	Geant4	4.05×10^8	5.7×10^5	$8.8(1) \times 10^3$	$8(2) \times 10^2$
	Average	$4.08(5) \times 10^8$	$5.2(7) \times 10^5$	$7.7(15) \times 10^3$	$1.0(3) \times 10^3$
TPC	PHITS	6.8×10^4	5.5×10^4	6.6×10^2	$6.5(6) \times 10^1$
	Geant4	7.0×10^4	1.1×10^5	2.0×10^3	$2.0(1) \times 10^2$
	Average	$6.9(1) \times 10^4$	$9(4) \times 10^4$	$1.4(10) \times 10^3$	$1.3(9) \times 10^2$
WASA	PHITS	3.3×10^4	1.0×10^4	2.9×10^2	3.2×10^1
	Geant4	3.1×10^4	1.6×10^4	4.1×10^2	5.5×10^1
	Average	$3.23(8) \times 10^4$	$1.3(4) \times 10^4$	$3.5(9) \times 10^2$	$4.4(16) \times 10^1$

We can see how the LiF almost eliminates the cold part of the neutron spectra in both the TPC and WASA calorimeter. This also results in a decrease in the flux of electrons and positrons by around two orders of magnitude. Looking at Figure 40, we note that the flux reduction comes primarily at late times, which is expected since this is when the cold neutrons enter the detector region. We see that while PHITS and Geant4 agree reasonably well for the WASA fluxes, some more prominent differences can be seen in the TPC. What is particularly notable is that PHITS predicts a higher flux of intermediate-energy neutrons than Geant4 while it predicts lower fluxes of other particle species. This may indicate that

Geant4 features more reaction channels or a higher cross-section in the existing reaction channels.

The background rates given in Table 2 correspond to around $\sim 1 \times 10^7$ electrons entering the TPC per second. Preliminary Geant4 simulations (which, as Table 2 establishes, estimate higher electron rates than PHITS) indicate that the track rate may be more than halved to around $\sim 4 \times 10^6\,\mathrm{s}^{-1}$ by also adding LiF around the cosmic veto. These rates should be manageable with current technology. For instance, the original ALICE TPC was designed to cope with 2×10^4 tracks per central Pb-Pb collision in the central pseudorapidity range $|\eta| < 0.9$ [70]. The cylinder defined by this pseudorapidity range has a half-length of 86 cm and an inner surface area of $9 \times 10^4\,\mathrm{cm}^2$ (assuming an 84 cm inner radius). With a drift velocity of 2.5 cm/µs and a drift length of 86 cm, the track rate density can be estimated to be $6 \times 10^3\,/(\mathrm{cm}^2 \cdot \mathrm{s})$ which may be compared with an inner TPC surface of $7 \times 10^3\,\mathrm{cm}^2$ and resulting track rate density of $6 \times 10^2\,/(\mathrm{cm}^2 \cdot \mathrm{s})$ for HIBEAM. This observation, combined with early prototype testing, indicates that track identification should be possible at these rates [71].

The origin process and volume of the remaining electron flux in the TPC and photon flux in WASA are shown in Figure 41. It is seen that the main sources of the background remain the same as before (although at much lower overall fluxes), but some differences may be noted. For instance, the relative contribution to the photon flux from the outer parts of the detector (passive shield and cosmic veto) is greater. This contribution likely

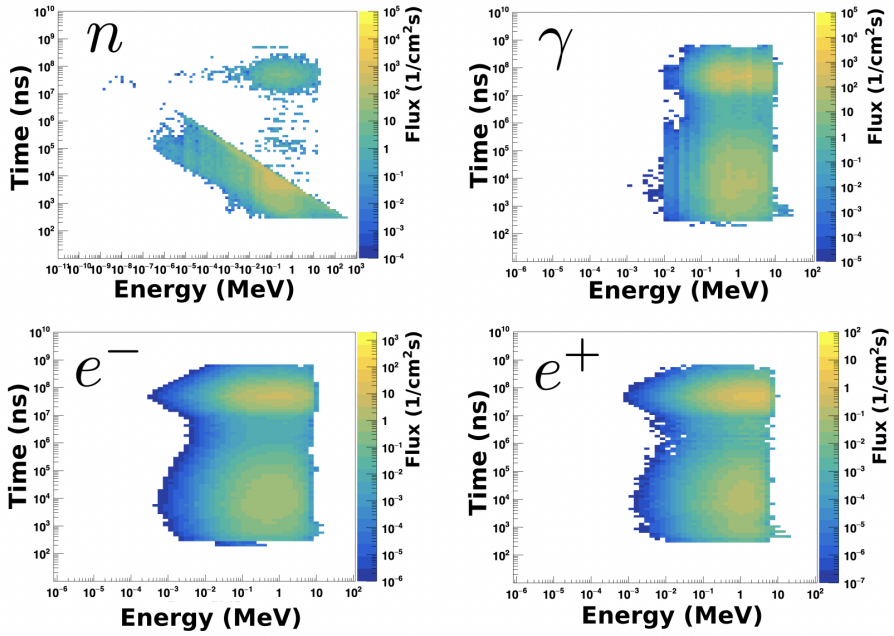

Figure 40: Energy-time correlations of the spallation background in WASA for a 5 mm Al vacuum vessel with 5 mm LiF cladding. Results are obtained from Geant4 simulation.

comes from higher-energy neutrons, not being captured by the LiF, which are slowed down in the detector material and undergoing subsequent capture. Some contribution also stems from neutrons which enter the experimental cave outside the vacuum pipe and thus do not need to pass the LiF.

One notable feature of Figure 40, which shall now be discussed in some detail, is the emergence of high-energy neutrons which arrive at significantly later times than the direct beam. This is clearly seen in Geant4, yet the PHITS simulation features no neutrons with $t > 10^7$ ns. From Geant4, it can be determined that the origin of these neutrons is inelastic triton reactions in the LiF layer. It is caused by the reaction channel $n + {}^6\mathrm{Li} \rightarrow {}^4\mathrm{He} + t$, $Q = 4.785\,\mathrm{MeV}$. This is followed by secondary triton-induced reactions yielding high-energy photons and neutrons such as $t + {}^6\mathrm{Li} \rightarrow {}^9\mathrm{Be} + \gamma$, $Q = 17.7\,\mathrm{MeV}$ or $t + {}^6\mathrm{Li} \rightarrow {}^8\mathrm{Be} + n \rightarrow 2\,{}^4\mathrm{He} + n$, $Q = 16.1\,\mathrm{MeV}$. These reaction channels of Geant4 have previously been described and compared to experimental data in Ref. [72].

We conclude this section with a plot showing the spatial origin in the transverse plane of the neutrons resulting from triton scattering in Figure 42(a). The energy spectrum of these neutrons, as observed in the TPC, is indicated in Figure 42(b). Firstly, we see that the large majority of the relevant neutrons emanate from a circle with a radius of 21 cm, consistent with the position of the LiF layer. The few events not on the circle are coming from triton scattering in the annihilation target. The energy spectrum shown here is consistent with that of Ref. [72] and clearly shows the presence of neutron energies up to 18 MeV.

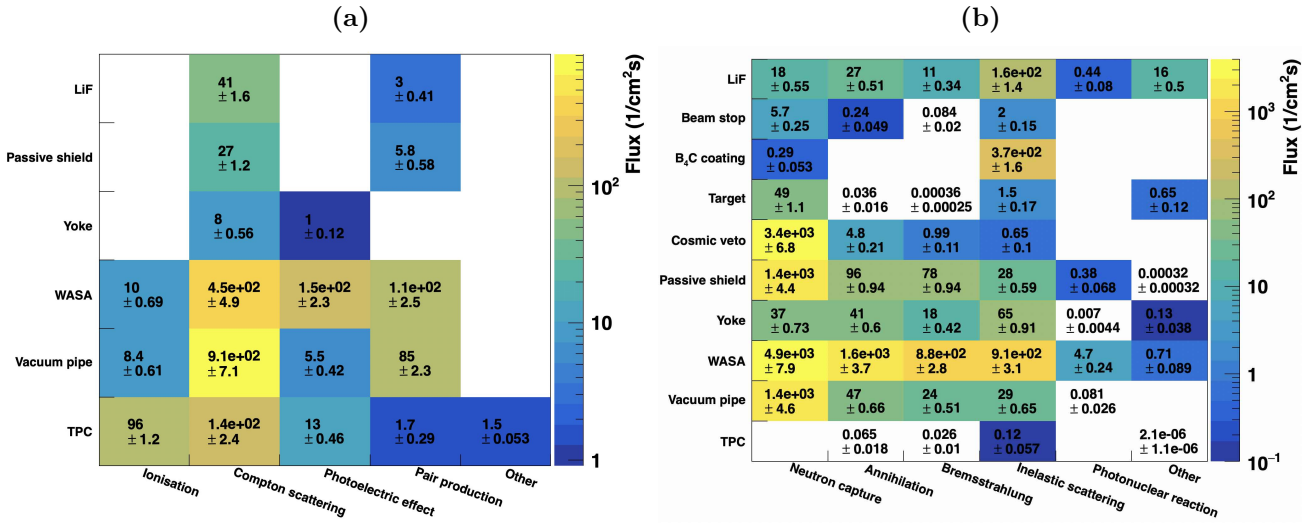

Figure 41: The particle flux in particle/(cm^2· s), subdivided into originating volume on the vertical axis and originating physics process on the horizontal axis with the added LiF layer. The results are obtained from Geant4 simulation. The shown uncertainties are statistical. **Panel (a):** For electrons in the TPC. **Panel (b):** For photons in the WASA calorimeter.

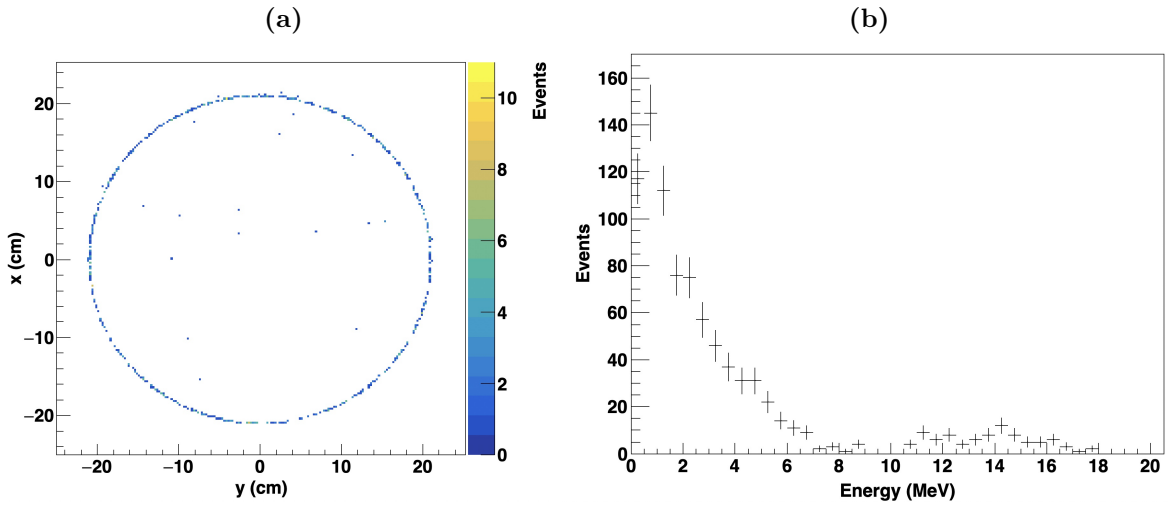

Figure 42: Panel (a): Distribution in the transverse plane of the spatial origins of neutrons stemming from triton scattering. **Panel (b)**: Energy distribution of neutrons originating from triton scattering.

6 Conclusions and outlook

This thesis has led to the development of shielding designs for both the HIBEAM beamline as well as the temporary beam stops at ESS. These designs satisfy the required dose rate limits established by ESS. While doing so, the traditional neutron source term used for ESS shielding calculations has been probed and compared with a new method based on kernel density estimation. The conclusion is that kernel density estimation can better reproduce the neutron spectrum from the spallation process. The main challenge at the time of writing is the extensive file size of the dump files and particle lists that need to be produced to perform large-scale simulations. However, combined with suitable variance reduction techniques, reasonable results can still be obtained with limited resources, even for extended neutron beamlines as demonstrated by this thesis. One option is to repeat the resampling procedure further down in the beamline (e.g., at the bunker wall) as this will mean that more of the stored particles are contributing to the flux outside the beamline shielding, thereby improving statistics without increasing the file size. Another possible development is to investigate the performance of other kernel functions than the Gaussian, as well as the use of different optimisation variables (e.g. spherical coordinates).

Previous neutron oscillation measurements have used reactor sources and bent beamlines where the high-energy background is heavily reduced compared to what is expected from a straight beamline at a high-power spallation source such as ESS. This work provides the first quantifiable measurements of the spallation background which indicate that the experiment can proceed to the implementation stage. However, additional measures can still be taken to further suppress the background. The background arising from the cold

part of the spectrum could be reduced by optimising the choice of neutron poison as well as its placement and thickness. Meanwhile, the background due to fast neutrons may be suppressed using timing cuts. Setting the timing cut late will eliminate more of the background from intermediate-energy neutrons (which may not be fully absorbed by the neutron poison). Setting it too late will, however, lower the obtained FOM so finding an optimal value is not trivial.

With the detector simulations performed in both PHITS and Geant4, this work has enabled some comparisons between the two codes. While the codes have provided similar results for the given detector geometry, some interesting differences could be noted, most notably in the interaction with the neutron poisons B_4C and LiF. To further isolate and investigate these effects, a natural next step is to simplify the geometry and use identical geometries in PHITS and Geant4. Supplementing the results with those of MCNP is also under consideration. Such benchmarking studies, combined with further investigation into the applied models and data libraries, ideally in combination with experimental data, could aid in the further development of these codes.

While this thesis has exclusively focussed on the spallation background in the detector, it is necessary to study signal events, where antineutrons are incident on the annihilation target. For instance, it is important to ensure that the vacuum pipe does not obscure event identification, e.g. from scattering leading to incorrect vertexing. Preliminary studies have already been performed for the NNBAR beamline [73], and performing similar studies for HIBEAM is easily achievable using the model developed in this thesis. Closer studies of the background contribution from cosmic rays are also necessary, as cosmic events could potentially look similar to signal events. Such studies have recently been performed for the NNBAR geometry using the CRY cosmic-shower library [74] and can be transferred to the HIBEAM geometry developed here.

References

1. Persson, L. B. & Santoro, V. Temporary Beamstop Shielding Calculation. **ESS-5286512** (2024).
2. Santoro, V. *et al.* The HIBEAM program: search for neutron oscillations at the ESS. arXiv:2311.08326 [physics.ins-det]. doi:10.48550/arXiv.2311.08326 (2023).
3. ESS Technical Design Report (ed Peggs, S.) https://europeanspallationsource.se/sites/default/files/downloads/2017/09/TDR_online_ver_all.pdf (2013).
4. Garoby, R. *et al.* The European Spallation Source Design. *Physica Scripta* **93,** 014001. ISSN: 0031-8949, 1402-4896. doi:10.1088/1402-4896/aa9bff (2018).
5. Andersen, K. H. *et al.* The instrument suite of the European Spallation Source. *Nuclear Instruments and Methods in Physics Research Section A: Accelerators, Spectrometers, Detectors and Associated Equipment* **957,** 163402. ISSN: 0168-9002. doi:10.1016/j.nima.2020.163402 (2020).
6. Abele, H. *et al.* Particle physics at the European Spallation Source. *Physics Reports* **1023,** 1–84. ISSN: 0370-1573. doi:10.1016/j.physrep.2023.06.001 (2023).
7. Baldo-Ceolin, M. *et al.* A new experimental limit on neutron-antineutron oscillations. *Zeitschrift für Physik C Particles and Fields* **63,** 409–416. ISSN: 1431-5858. doi:10.1007/BF01580321 (1994).
8. Sato, T. *et al.* Recent improvements of the particle and heavy ion transport code system – PHITS version 3.33. *Journal of Nuclear Science and Technology* **61.** Publisher: Taylor & Francis, 127–135. ISSN: 0022-3131. doi:10.1080/00223131.2023.2275736 (2024).
9. Bargholtz, C. *et al.* The WASA detector facility at CELSIUS. *Nuclear Instruments and Methods in Physics Research Section A: Accelerators, Spectrometers, Detectors and Associated Equipment* **594,** 339–350. ISSN: 0168-9002. doi:10.1016/j.nima.2008.06.011 (2008).
10. Allison, J. *et al.* Recent developments in Geant4. *Nuclear Instruments and Methods in Physics Research Section A: Accelerators, Spectrometers, Detectors and Associated Equipment* **835,** 186–225. ISSN: 0168-9002. doi:10.1016/j.nima.2016.06.125 (2016).
11. Agostinelli, S. *et al.* Geant4—a simulation toolkit. *Nuclear Instruments and Methods in Physics Research Section A: Accelerators, Spectrometers, Detectors and Associated Equipment* **506,** 250–303. ISSN: 0168-9002. doi:10.1016/S0168-9002(03)01368-8 (2003).
12. Allison, J. *et al.* Geant4 developments and applications. *IEEE Transactions on Nuclear Science* **53,** 270–278. ISSN: 1558-1578. doi:10.1109/TNS.2006.869826 (2006).

13. AMS Collaboration *et al.* Antiproton Flux, Antiproton-to-Proton Flux Ratio, and Properties of Elementary Particle Fluxes in Primary Cosmic Rays Measured with the Alpha Magnetic Spectrometer on the International Space Station. *Physical Review Letters* **117.** Publisher: American Physical Society, 091103. doi:10.1103/PhysRevLett.117.091103 (2016).

14. Luque, P. D. L. T. Combined analyses of the antiproton production from cosmic-ray interactions and its possible dark matter origin. *Journal of Cosmology and Astroparticle Physics* **2021.** Publisher: IOP Publishing, 018. ISSN: 1475-7516. doi:10.1088/1475-7516/2021/11/018 (2021).

15. Gusev, A. A. *et al.* Antiproton radiation belt produced by cosmic rays in the Earth magnetosphere. *Geophysical Research Letters* **30.** ISSN: 1944-8007. doi:10.1029/2002GL016146 (2003).

16. Von Ballmoos, P. Antimatter in the Universe: constraints from gamma-ray astronomy. *Hyperfine Interactions* **228,** 91–100. ISSN: 1572-9540. doi:10.1007/s10751-014-1024-9 (2014).

17. Kawasaki, M., Nakatsuka, H., Nakayama, K. & Sekiguchi, T. Revisiting CMB constraints on dark matter annihilation. *Journal of Cosmology and Astroparticle Physics* **2021.** Publisher: IOP Publishing, 015. ISSN: 1475-7516. doi:10.1088/1475-7516/2021/12/015 (2021).

18. Aghanim, N. *et al.* Planck 2018 results - VI. Cosmological parameters. *Astronomy & Astrophysics (A&A)* **641,** A6. doi:10.1051/0004-6361/201833910 (2020).

19. Sakharov, A. D. Violation of CP invariance, C asymmetry, and baryon asymmetry of the universe. *Soviet Physics Uspekhi* **34.** Publisher: IOP Publishing, 392. ISSN: 0038-5670. doi:10.1070/PU1991v034n05ABEH002497 (1991).

20. Riotto, A. & Trodden, M. Recent Progress in Baryogenesis. *Annual Review of Nuclear and Particle Science* **49,** 35–75. doi:10.1146/annurev.nucl.49.1.35 (1999).

21. White, G. A. in *A Pedagogical Introduction to Electroweak Baryogenesis* chap. The Sakharov conditions (Morgan & Claypool Publishers, 2016). doi:10.1088/978-1-6817-4457-5ch2.

22. Wu, C. S., Ambler, E., Hayward, R. W., Hoppes, D. D. & Hudson, R. P. Experimental Test of Parity Conservation in Beta Decay. *Physical Review* **105.** Publisher: American Physical Society, 1413–1415. doi:10.1103/PhysRev.105.1413 (1957).

23. Christenson, J. H., Cronin, J. W., Fitch, V. L. & Turlay, R. Evidence for the 2π Decay of the K_2^0 Meson. *Physical Review Letters* **13.** Publisher: American Physical Society, 138–140. doi:10.1103/PhysRevLett.13.138 (1964).

24. Addazi, A. *et al.* New high-sensitivity searches for neutrons converting into antineutrons and/or sterile neutrons at the HIBEAM/NNBAR experiment at the European Spallation Source. *Journal of Physics G: Nuclear and Particle Physics* **48.** Publisher: IOP Publishing, 070501. ISSN: 0954-3899. doi:10.1088/1361-6471/abf429 (2021).

25. Phillips, D. G. *et al.* Neutron-antineutron oscillations: Theoretical status and experimental prospects. *Physics Reports* **612,** 1–45. ISSN: 0370-1573. doi:10.1016/j.physrep.2015.11.001 (2016).

26. Lundmark, K. Über die Bestimmung der Entfernungen, Dimensionen, Massen und Dichtigkeit fur die nächstgelegenen anagalacktischen Sternsystem. *Meddelanden fran Lunds Astronomiska Observatorium Series I* **125,** 1–13. https://ui.adsabs.harvard.edu/abs/1930MeLuF.125....1L/abstract (1930).

27. Zwicky, F. Republication of: The redshift of extragalactic nebulae. *General Relativity and Gravitation* **41,** 207–224. ISSN: 1572-9532. doi:10.1007/s10714-008-0707-4 (2009).

28. Oort, J. H. The force exerted by the stellar system in the direction perpendicular to the galactic plane and some related problems. *Bulletin of the Astronomical Institutes of the Netherlands* **6,** 249. https://ui.adsabs.harvard.edu/abs/1932BAN.....6..249O (1932).

29. Rubin, V. C. & Ford W. Kent, J. Rotation of the Andromeda Nebula from a Spectroscopic Survey of Emission Regions. *Astrophysical Journal* **159,** 379. doi:10.1086/150317 (1970).

30. Kane, G. *Modern Elementary Particle Physics: Explaining and Extending the Standard Model.* 2nd ed. (Cambridge University Press, 2017).

31. Foot, R. Mirror dark matter: Cosmology, galaxy structure and direct detection. *International Journal of Modern Physics A* **29.** Publisher: World Scientific Publishing Co., 1430013. ISSN: 0217-751X. doi:10.1142/S0217751X14300130 (2014).

32. Filges, D. & Goldenbaum, F. *Handbook of Spallation Research: Theory, Experiments and Applications* doi:10.1002/9783527628865 (Wiley-VCH, 2009).

33. Boudard, A., Cugnon, J., Leray, S. & Volant, C. Intranuclear cascade model for a comprehensive description of spallation reaction data. *Physical Review C* **66,** 044615. ISSN: 0556-2813, 1089-490X. doi:10.1103/PhysRevC.66.044615 (2002).

34. Weisskopf, V. Statistics and Nuclear Reactions. *Physical Review* **52,** 295–303. ISSN: 0031-899X. doi:10.1103/PhysRev.52.295 (1937).

35. Furihata, S., Niita, K., Meigo, S.-i., Ikeda, Y. & Maekawa, F. *The GEM code. A simulation program for the evaporation and the fission process of an excited nucleus* tech. rep. JAERI-Data/Code–2001-015 (Japan, 2001). http://inis.iaea.org/search/search.aspx?orig_q=RN:33006007.

36. Brown, D. *et al.* ENDF/B-VIII.0: The 8th Major Release of the Nuclear Reaction Data Library with CIELO-project Cross Sections, New Standards and Thermal Scattering Data. *Nuclear Data Sheets* **148.** Special Issue on Nuclear Reaction Data, 1 –142. ISSN: 0090-3752. doi:https://doi.org/10.1016/j.nds.2018.02.001 (2018).

37. Iwamoto, O. *et al.* Japanese evaluated nuclear data library version 5: JENDL-5. *Journal of Nuclear Science and Technology* **60.** Publisher: Taylor & Francis, 1–60. ISSN: 0022-3131. doi:10.1080/00223131.2022.2141903 (2023).

38. *PHITS User's Manual Ver 3.31.* 2024. https://phits.jaea.go.jp/manual/manualE-phits.pdf (Mar. 16, 2024).

39. Willendrup, P., Farhi, E., Knudsen, E., Filges, U. & Lefmann, K. *Component Manual for the neutron ray-tracing package McStas.* 2022. https://www.mcstas.org/documentation/manual/mcstas-3.2-components.pdf (Mar. 16, 2024).

40. Santoro, V. *et al.* HighNESS conceptual design report: Volume II. The NNBAR experiment. *Journal of Neutron Research* **25.** Publisher: IOS Press, 315–406. ISSN: 1477-2655. doi:10.3233/JNR-230951 (2023).

41. Super-Kamiokande Collaboration. Neutron-antineutron oscillation search using a 0.37 megaton-years exposure of Super-Kamiokande. *Physical Review D* **103.** Publisher: American Physical Society, 012008. doi:10.1103/PhysRevD.103.012008 (2021).

42. SNO Collaboration. Search for neutron-antineutron oscillations at the Sudbury Neutrino Observatory. *Physical Review D* **96.** Publisher: American Physical Society, 092005. doi:10.1103/PhysRevD.96.092005 (2017).

43. Abi, B. *et al.* Deep Underground Neutrino Experiment (DUNE), Far Detector Technical Design Report, Volume II: DUNE Physics. arXiv:2002.03005 [hep-ex]. doi:10.48550/arXiv.2002.03005 (2020).

44. Abe, K. & Tanaka, H.-K. Hyper-Kamiokande construction status and prospects. *Frontiers in Physics* **12.** Publisher: Frontiers. ISSN: 2296-424X. doi:10.3389/fphy.2024.1378254 (2024).

45. *ESS Media Bank.* https://europeanspallationsource.se/media-bank (Mar. 25, 2024).

46. Zanini, L. *et al.* Design of the cold and thermal neutron moderators for the European Spallation Source. *Nuclear Instruments and Methods in Physics Research Section A: Accelerators, Spectrometers, Detectors and Associated Equipment* **925,** 33–52. ISSN: 0168-9002. doi:10.1016/j.nima.2019.01.003 (2019).

47. Kolevatov, R., Bentley, P. M., Santoro, V. & Holl, M. E6 Neutron Beam Optic Assembly Technical Specification. **ESS-5313916** (2024).

48. Björk, L. Development of a guide system for free neutron oscillation searches at the European Spallation Source. http://lup.lub.lu.se/student-papers/record/9126666 (2023).

49. Barrow, J. L., Botvina, A. S., Golubeva, E. S. & Richard, J.-M. New model of intranuclear neutron-antineutron transformations in ${}^{16}_{8}$O. *Physical Review C* **105.** Publisher: American Physical Society, 065501. doi:10.1103/PhysRevC.105.065501 (2022).

50. WASA-at-COSY Collaboration. Search for the η mesic ^{3}He in the $pd \to dp\ \pi^0$ reaction with the WASA-at-COSY facility. *Physical Review C* **102.** Publisher: American Physical Society, 044322. doi:10.1103/PhysRevC.102.044322 (2020).

51. Saito, T. R. *et al.* The WASA-FRS project at GSI and its perspective. *Nuclear Instruments and Methods in Physics Research Section B: Beam Interactions with Materials and Atoms* **542,** 22–25. ISSN: 0168-583X. doi:10.1016/j.nimb.2023.05.042 (2023).

52. Ansell, S. CombLayer - A fast parametric MCNP(X) model constructor. *Proceedings of the 21st meeting of the international collaboration on advanced neutron sources (ICANS-21).* JAEA-Conf–2015-002, 148–154. doi:10.11484/jaea-conf-2015-002 (2016).

53. Ansell, S. *SAnsell/CombLayer.* https://github.com/SAnsell/CombLayer (2024).

54. Kittelmann, T. *et al.* Monte Carlo Particle Lists: MCPL. *Computer Physics Communications* **218,** 17–42. ISSN: 0010-4655. doi:10.1016/j.cpc.2017.04.012 (2017).

55. Schmidt, N. S. *et al.* KDSource, a tool for the generation of Monte Carlo particle sources using kernel density estimation. *Annals of Nuclear Energy* **177,** 109309. ISSN: 0306-4549. doi:10.1016/j.anucene.2022.109309 (2022).

56. Abbate, O. I. *et al. KDSource, a tool for the generation of Monte Carlo particle sources using kernel density estimation.* https://github.com/KDSource/KDSource (2023).

57. Brun, R. & Rademakers, F. ROOT — An object oriented data analysis framework. *Nuclear Instruments and Methods in Physics Research Section A: Accelerators, Spectrometers, Detectors and Associated Equipment. New Computing Techniques in Physics Research V* **389,** 81–86. ISSN: 0168-9002. doi:10.1016/S0168-9002(97)00048-X (1997).

58. Santoro, V., Di Julio, D., Bentley, P. & Zanini, L. Source term for shielding design of bunker and beamlines at the ESS. **ESS-0416080** (2019).

59. Boudard, A., Cugnon, J., David, J.-C., Leray, S. & Mancusi, D. New potentialities of the Liege intranuclear cascade model for reactions induced by nucleons and light charged particles. *Physical Review C* **87.** Publisher: American Physical Society, 014606. doi:10.1103/PhysRevC.87.014606 (2013).

60. Muhrer, G. ESS Procedure for designing shielding for safety. **ESS-0019931.** Rev. 6 (2023).

61. Clement, C. *et al.* Conversion Coefficients for Radiological Protection Quantities for External Radiation Exposures. *Annals of the ICRP* **40.** Publisher: SAGE Publications Ltd, 1–257. ISSN: 0146-6453. doi:10.1016/j.icrp.2011.10.001 (2010).

62. Johansson, L. ESS Handbook for Radiation Protection Chapter 2. General Radiation Protection Rules. **ESS-0239718.** Rev. 12 (2024).

63. Hřivnáčová, I. The Virtual Geometry Model. *EPJ Web of Conferences* **245.** Publisher: EDP Sciences, 02014. ISSN: 2100-014X. doi:10.1051/epjconf/202024502014 (2020).

64. Rappold, C. *ChristopheRappold/G4SolenoidSuperFRS.* https://github.com/ChristopheRappold/G4SolenoidSuperFRS (2017).

65. Mendoza, E. & Cano-Ott, D. *Update of the Evaluated Neutron Cross Section Libraries for the Geant4 Code* tech. rep. (IAEA Nuclear Data Section, 2018). doi:10.61092/iaea.5knd-4xdd.

66. Geant4 Collaboration. *Guide For Physics Lists.* 2023. https://geant4-userdoc.web.cern.ch/UsersGuides/PhysicsListGuide/fo/PhysicsListGuide.pdf (Jan. 22, 2024).

67. Hirayama, H., Namito, Y., Bielajew, A. F., Wilderman, S. J. & Nelson, W. R. *The EGS5 code system* tech. rep. KEK–2005-8 (Japan, 2005), 432. http://inis.iaea.org/search/search.aspx?orig_q=RN:38045743.

68. Yang, J.-Y. Exact Boundary Correction Methods for Multivariate Kernel Density Estimation. *Symmetry* **15.** Publisher: Multidisciplinary Digital Publishing Institute, 1670. ISSN: 2073-8994. doi:10.3390/sym15091670 (2023).

69. DiJulio, D. D. *et al.* Measurements of the neutron absorption in supermirror coatings. *Nuclear Instruments and Methods in Physics Research Section A: Accelerators, Spectrometers, Detectors and Associated Equipment* **1025,** 166088. ISSN: 0168-9002. doi:10.1016/j.nima.2021.166088 (2022).

70. Arslandok, M., Hellbär, E., Ivanov, M., Münzer, R. H. & Wiechula, J. Track Reconstruction in a High-Density Environment with ALICE. *Particles* **5,** 84–95. ISSN: 2571-712X. doi:10.3390/particles5010008 (2022).

71. Oskarsson, A. Private Communication. Lund University. 2024.

72. Santoro, V., DiJulio, D. D. & Bentley, P. M. MeV Neutron Production from Thermal Neutron Capture in ^{6}Li Simulated With Geant4. *Journal of Physics: Conference Series* **746.** Publisher: IOP Publishing, 012012. ISSN: 1742-6596. doi:10.1088/1742-6596/746/1/012012 (2016).

73. Eriksson, H. Design of the HIBEAM/NNBAR Vacuum System at the European Spallation Source. Lund University, MSc thesis, not yet published (2024).

74. Hagmann, C., Lange, D. & Wright, D. *Cosmic-ray shower generator (CRY) for Monte Carlo transport codes* in *2007 IEEE Nuclear Science Symposium Conference Record* **2** (2007), 1143–1146. doi:10.1109/NSSMIC.2007.4437209.

A Derivation of the eigenenergies and eigenvectors of neutron oscillation

Starting from Eq. (6), it is useful to rewrite the Hamiltonian as

$$\hat{H} \leftrightarrow \begin{pmatrix} \frac{1}{2}(E_n + E_{\bar{n}}) & 0 \\ 0 & \frac{1}{2}(E_n + E_{\bar{n}}) \end{pmatrix} + \begin{pmatrix} \frac{\Delta E}{2} & \alpha \\ \alpha & -\frac{\Delta E}{2} \end{pmatrix} = \frac{1}{2}(E_n + E_{\bar{n}})I + \frac{1}{2}\Delta E\, K, \tag{33}$$

where $\Delta E = E_n - E_{\bar{n}}$, I is the identity matrix and K is given by

$$K = \begin{pmatrix} 1 & \frac{2\alpha}{\Delta E} \\ \frac{2\alpha}{\Delta E} & -1 \end{pmatrix} = \begin{pmatrix} 1 & \tan 2\theta \\ \tan 2\theta & -1 \end{pmatrix}, \tag{34}$$

where we define $\tan 2\theta = \frac{2\alpha}{\Delta E}$. Let us denote the eigenvalues of K by κ. They are given by the solution of

$$0 = \det(K - \kappa I) = \begin{vmatrix} 1-\kappa & \tan 2\theta \\ \tan 2\theta & -1-\kappa \end{vmatrix} = \kappa^2 - 1 - \tan^2 2\theta, \tag{35}$$

which are

$$\kappa_{1,2} = \pm\sqrt{1 + \tan^2 2\theta} = \pm\frac{1}{\cos 2\theta} = \pm\frac{\sqrt{(\Delta E)^2 + 4\alpha^2}}{\Delta E}. \tag{36}$$

As for the eigenvectors $\mathbf{x}$ of K, we need to solve the eigenvalue equation $(K - \kappa I)\mathbf{x} = 0$. For $\kappa = 1/\cos(2\theta)$, we obtain an augmented matrix

$$\left[\begin{array}{cc|c} 1 - 1/\cos(2\theta) & \tan(2\theta) & 0 \\ \tan 2\theta & -1 - 1/\cos(2\theta) & 0 \end{array}\right] \sim \left[\begin{array}{cc|c} \cos(2\theta) - 1 & \sin(2\theta) & 0 \\ \sin 2\theta & -\cos(2\theta) - 1 & 0 \end{array}\right] \sim$$

$$\left[\begin{array}{cc|c} -2\sin^2\theta & 2\sin\theta\cos\theta & 0 \\ 2\sin\theta\cos\theta & -2\cos^2\theta & 0 \end{array}\right] \sim \left[\begin{array}{cc|c} -\sin\theta & \cos\theta & 0 \\ \sin\theta & -\cos\theta & 0 \end{array}\right]. \tag{37}$$

through application of trigonometric identities. It is now clear that $\mathbf{x} = (\cos\theta, \sin\theta)$ is the sought eigenvector in the $\{|n\rangle, |\bar{n}\rangle\}$ basis. Similarly, we find that the eigenvector belonging to $\kappa = -1/\cos 2\theta$ is $\mathbf{x} = (-\sin\theta, \cos\theta)$. Finally, we remark that the eigenvalue of the identity matrix is unity with any vectors being eigenvectors. We can thus conclude from Eq. (33) that the eigenvalues and eigenvectors of the full Hamiltonian are indeed given by Eqs. (8) and (9), respectively.

B Extended beam stop shielding simulation results

The following five configurations were considered:

- **Configuration 1:** A 5 mm thick B_4C layer is placed at the Neutron Beam Optical Assembly (NBOA) exit, 5.5 m from the moderator. No components are simulated in the bunker. The beam stop has outer dimensions of $3.5\times3.0\times2.93$ m^3.
- **Configuration 2:** A 5 mm thick B_4C layer is placed at the NBOA exit, 5.5 m from the moderator. An aluminium vacuum pipe with a radius of 80 mm and a thickness of 5 mm is simulated from the NBOA exit at 5.5 m to the bunker. The beam stop has outer dimensions of $3.5\times3.0\times2.93$ m^3.
- **Configuration 3:** An aluminium vacuum pipe with a radius of 80 mm and a thickness of 5 mm is simulated from the monolith insert exit at 5.5 m to the bunker. A 5 mm thick B_4C layer is placed 3 m from the monolith insert exit at 8.5 m and occupies the full cross-section of the vacuum pipe. The beam stop has outer dimensions of $3.5\times3.0\times2.93$ m^3.
- **Configuration 4:** Same as Configuration 1 but with the downstream bunker feedthrough filled with a heavy concrete plug. 1.5 cm distance is assumed on all sides of the plug to the feedthrough walls. The beam stop has outer dimensions of $1.8\times3.0\times2.83$ m^3.
- **Configuration 5:** Same as Configuration 1 but with both downstream and upstream feedthroughs filled with heavy concrete plugs. 1.5 cm distance is assumed on all sides of the plugs to the feedthrough walls. The beam stop has outer dimensions of $1.2\times1.8\times2.53$ m^3.

The results from Configuration 2 were presented in the main text, see Section 5.2. The remaining four configurations were also briefly discussed. In this appendix, the results from these configurations are presented in detail. A more thorough discussion may be found in Ref. [1].

Configuration 1

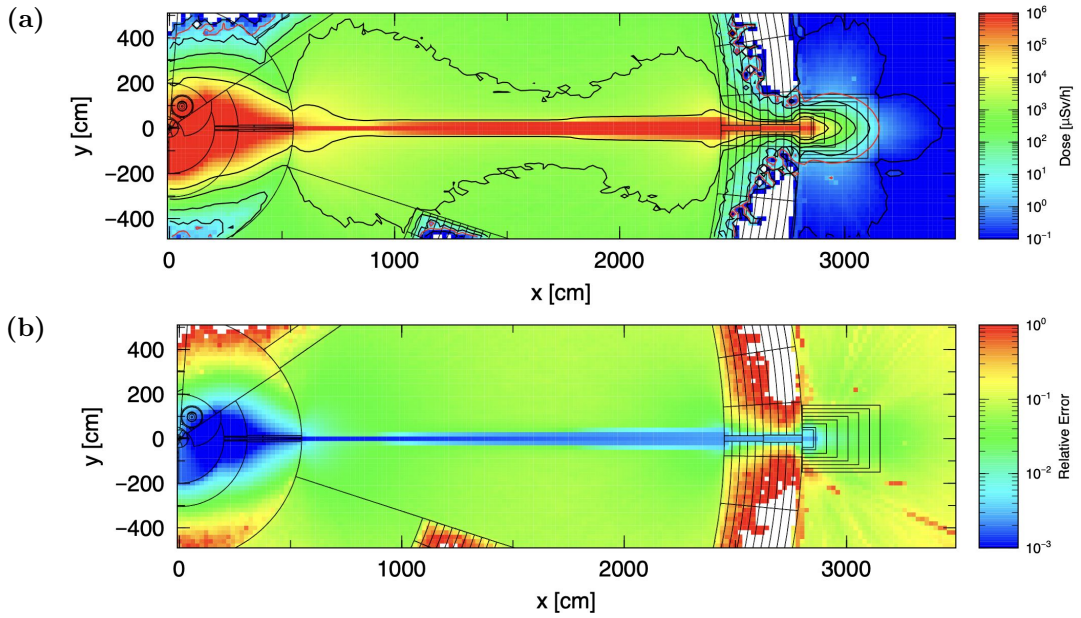

Figure 43: Panel (a): Dose map in the xy-plane for Configuration 1. The 1.5 µSv/h dose rate threshold is indicated by a red contour. **Panel (b)**: Statistical uncertainties associated with Panel (a).

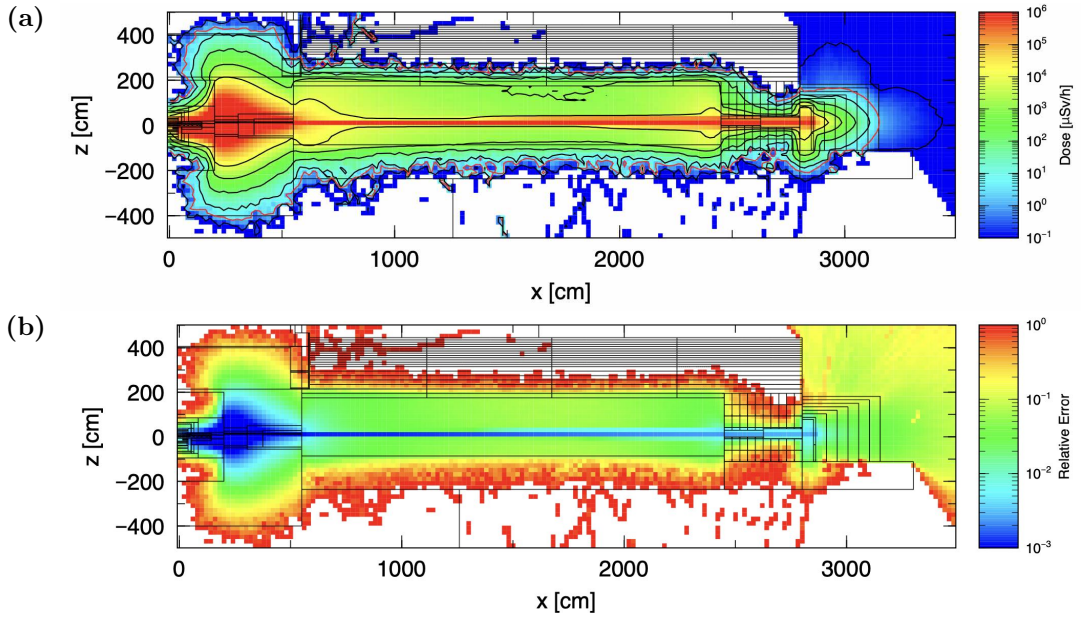

Figure 44: Panel (a): Dose map in the xz-plane for Configuration 1. The 1.5 µSv/h dose rate threshold is indicated by a red contour. **Panel (b)**: Statistical uncertainties associated with Panel (a).

Configuration 3

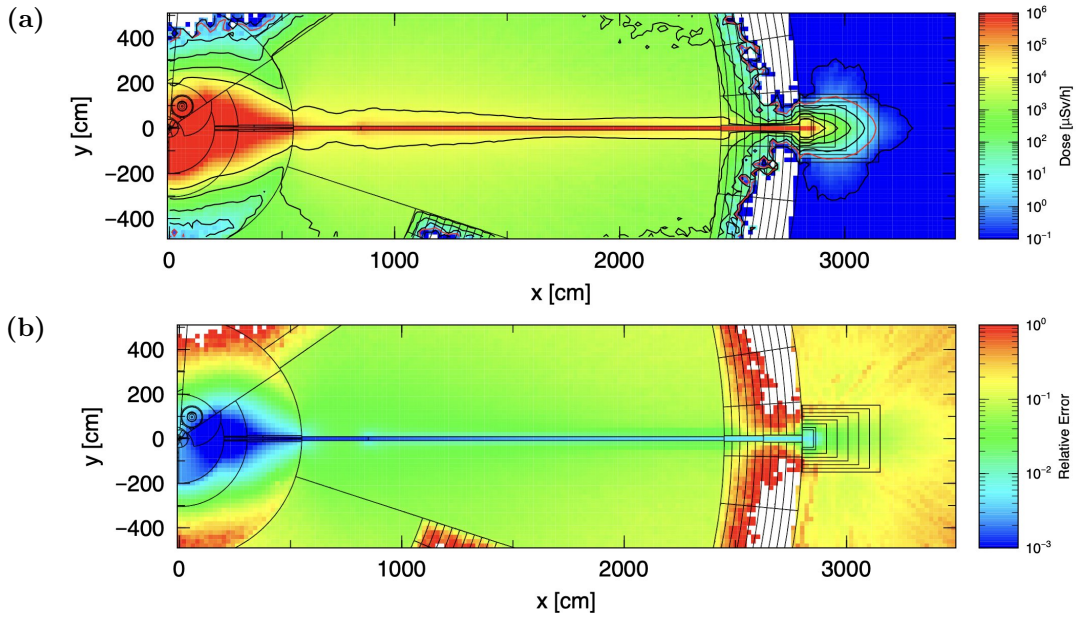

Figure 45: Panel (a): Dose map in the xy-plane for Configuration 3. The 1.5 µSv/h dose rate threshold is indicated by a red contour. **Panel (b)**: Statistical uncertainties associated with Panel (a).

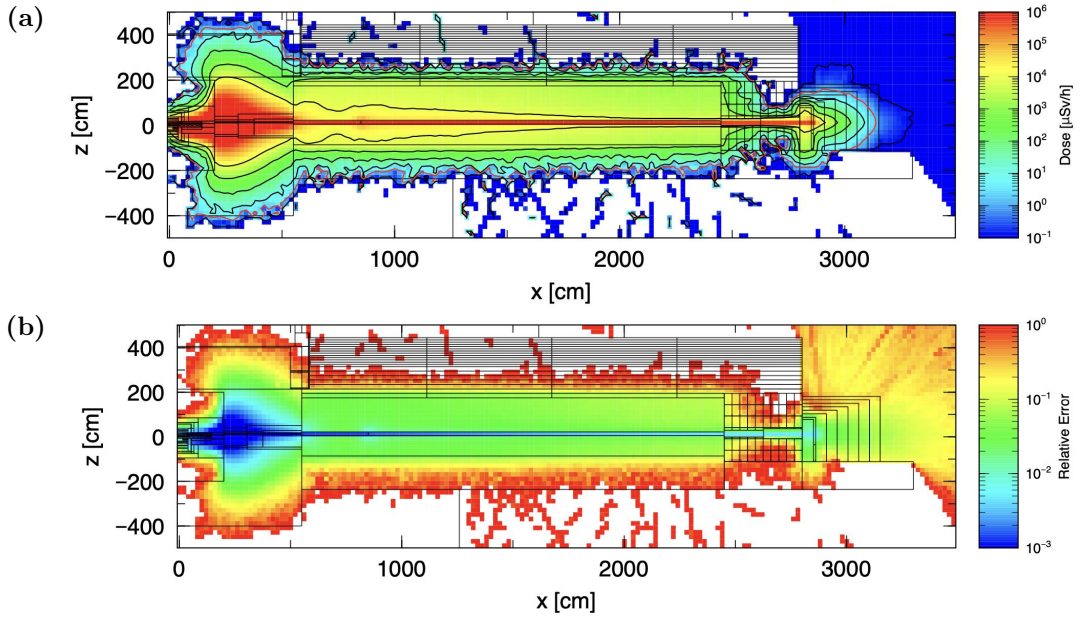

Figure 46: Panel (a): Dose map in the xz-plane for Configuration 3. The 1.5 µSv/h dose rate threshold is indicated by a red contour. **Panel (b)**: Statistical uncertainties associated with Panel (a).

Configuration 4

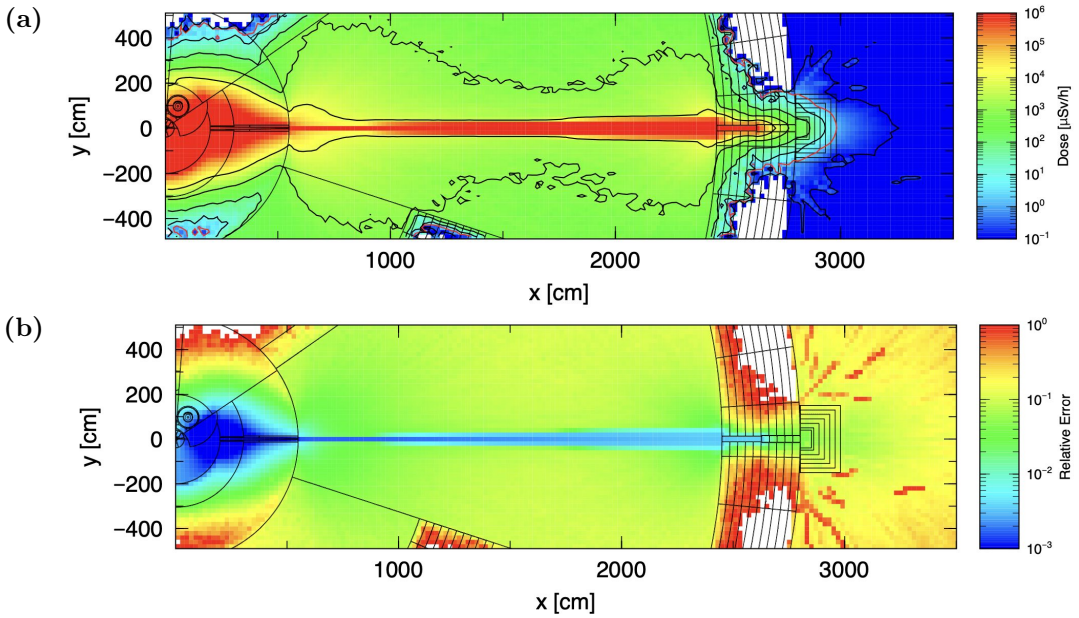

Figure 47: Panel (a): Dose map in the xy-plane for Configuration 4. The 1.5 µSv/h dose rate threshold is indicated by a red contour. **Panel (b)**: Statistical uncertainties associated with Panel (a).

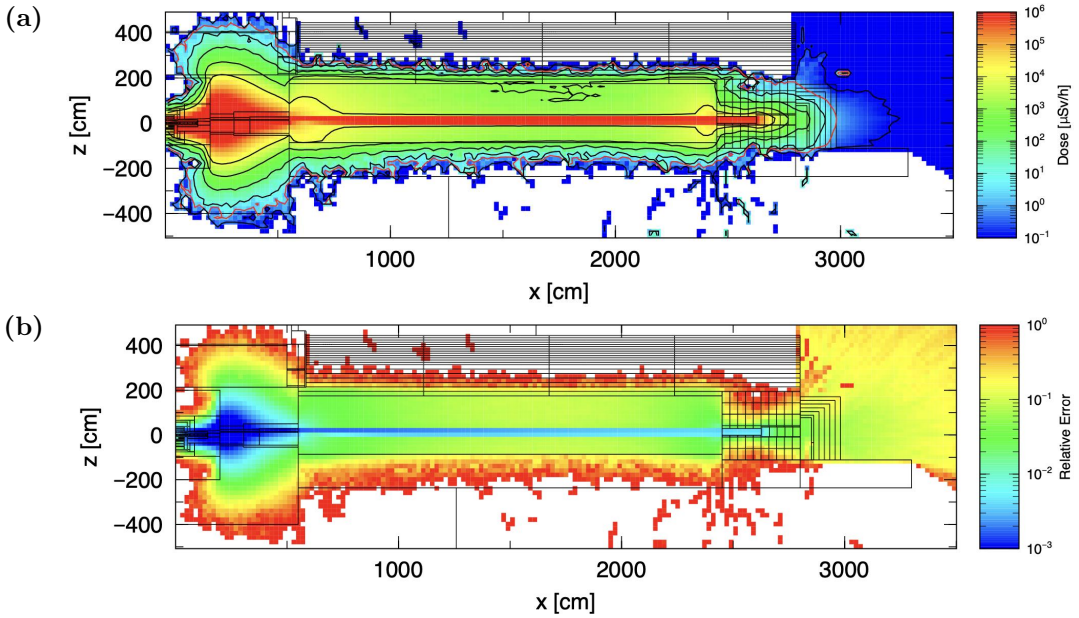

Figure 48: Panel (a): Dose map in the xz-plane for Configuration 4. The 1.5 µSv/h dose rate threshold is indicated by a red contour. **Panel (b)**: Statistical uncertainties associated with Panel (a).

Configuration 5

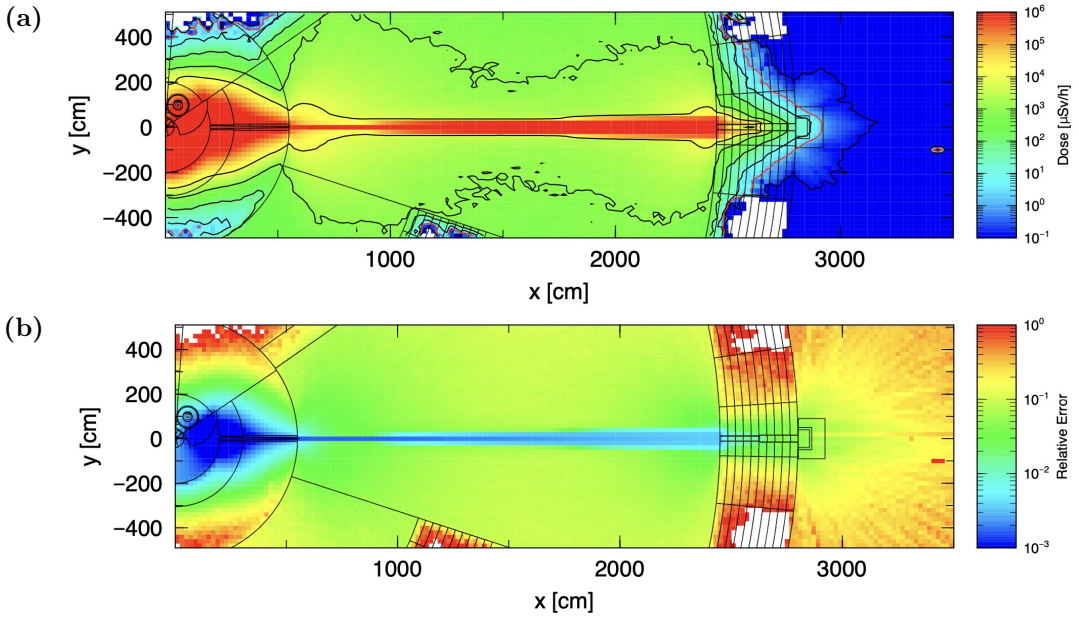

Figure 49: Panel (a): Dose map in the xy-plane for Configuration 5. The 1.5 μSv/h dose rate threshold is indicated by a red contour. **Panel (b)**: Statistical uncertainties associated with Panel (a).

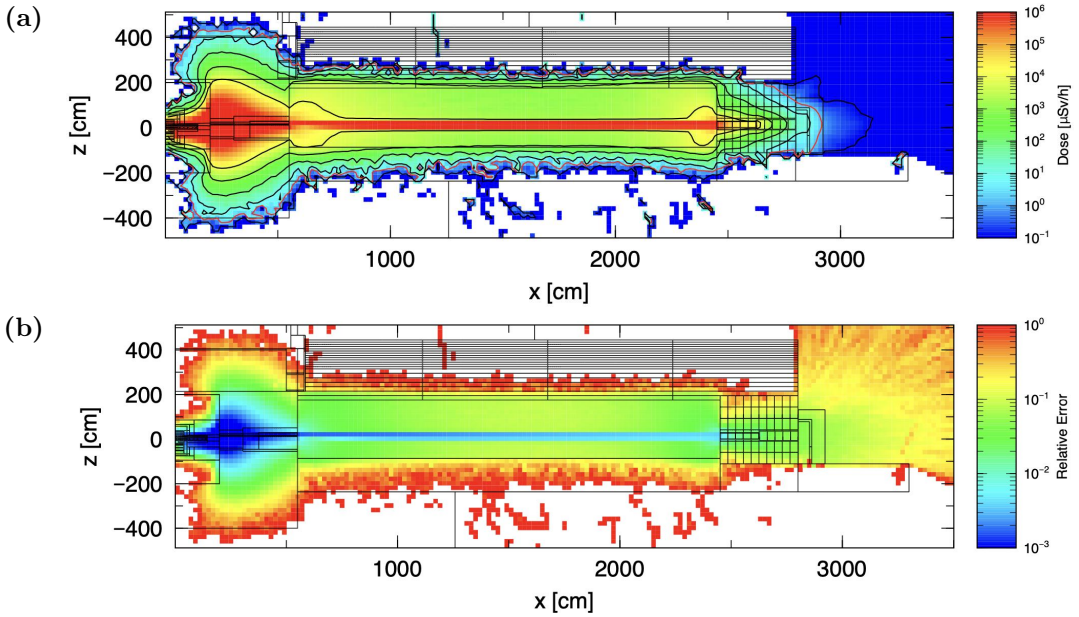

Figure 50: Panel (a): Dose map in the xz-plane for Configuration 5. The 1.5 μSv/h dose rate threshold is indicated by a red contour. **Panel (b)**: Statistical uncertainties associated with Panel (a).

C Extended HIBEAM shielding simulation results

In this appendix, the results of Section 5.3 are supplemented with dose maps separating the contribution from neutrons and photons. We can note that most of the statistical uncertainty is associated with the neutron dose. This is because the flux of high-energy neutrons is lower (fewer events) than the flux of photons outside the shielding, although the neutrons typically bring a much higher dose rate, as reflected by Figure 17(a).

Figures 51-52 show the neutron dose rates obtained using the source term. The corresponding photon dose rates are given by Figures 53-54. Figures 55-56 show the neutron dose rates obtained using KDE resampling. The photon doses from this source are shown in Figures 57-58.

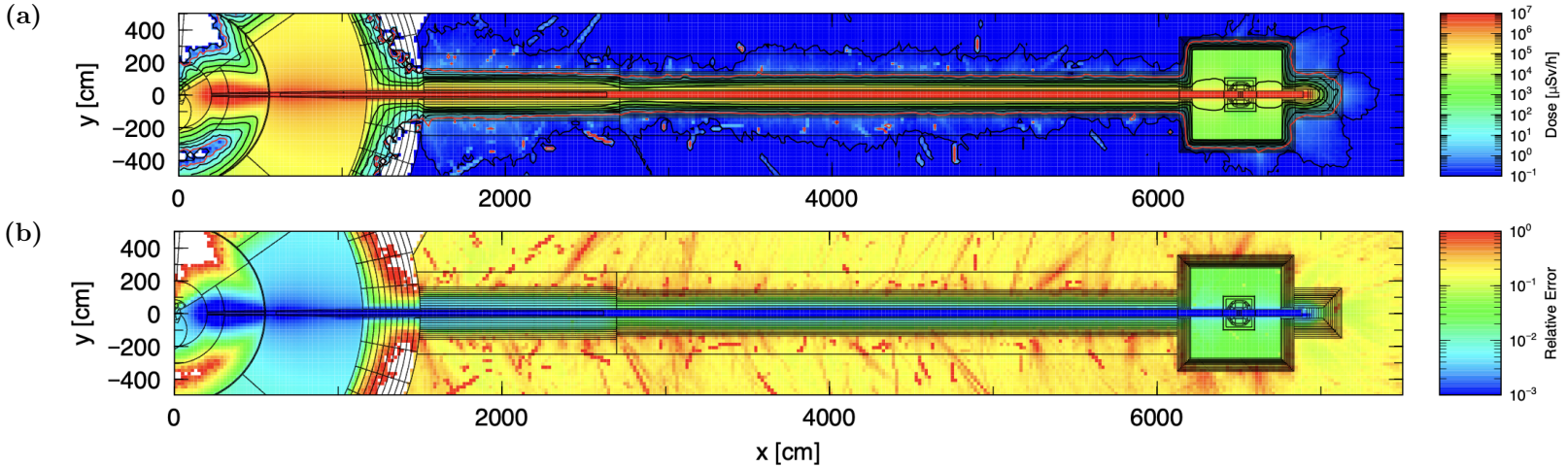

Figure 51: Panel (a): Neutron dose rate in the xy-plane with the neutron source term. **Panel (b)**: Statistical uncertainty associated with Panel (a).

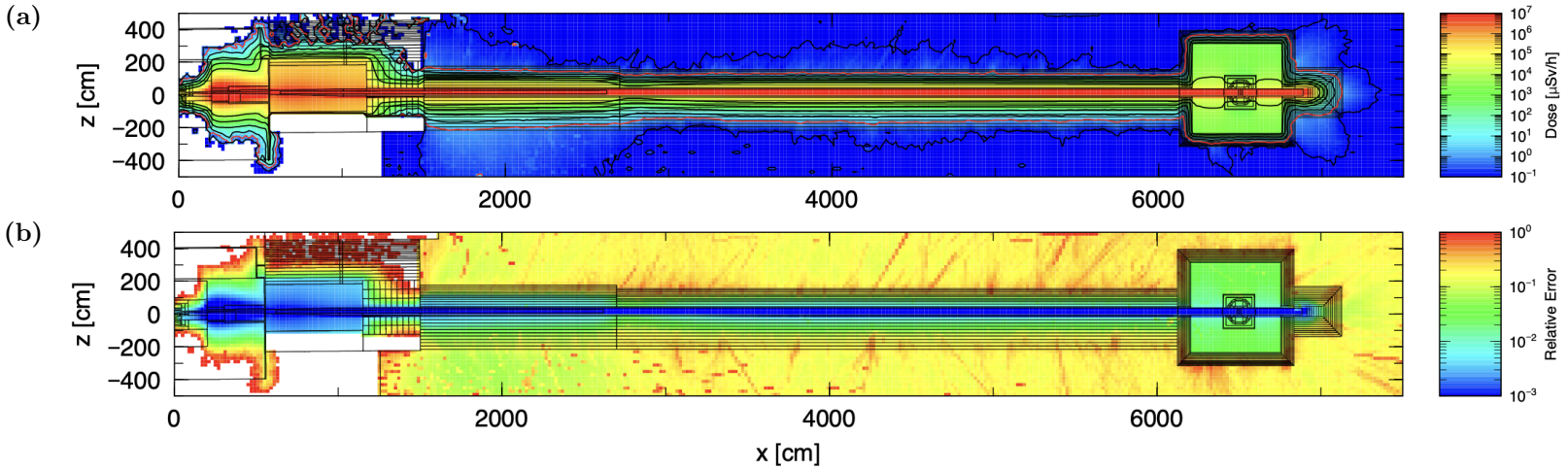

Figure 52: Panel (a): Neutron dose rate in the xz-plane with the neutron source term. **Panel (b)**: Statistical uncertainty associated with Panel (a).

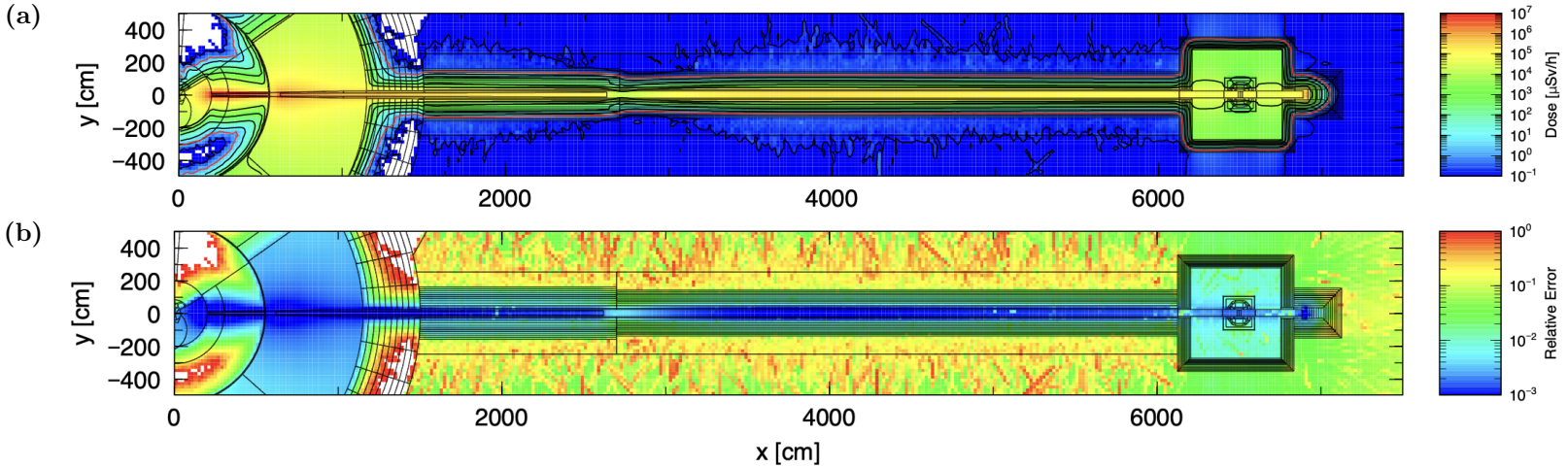

Figure 53: Panel (a): Photon dose rate in the xy-plane with the neutron source term. **Panel (b)**: Statistical uncertainty associated with Panel (a).

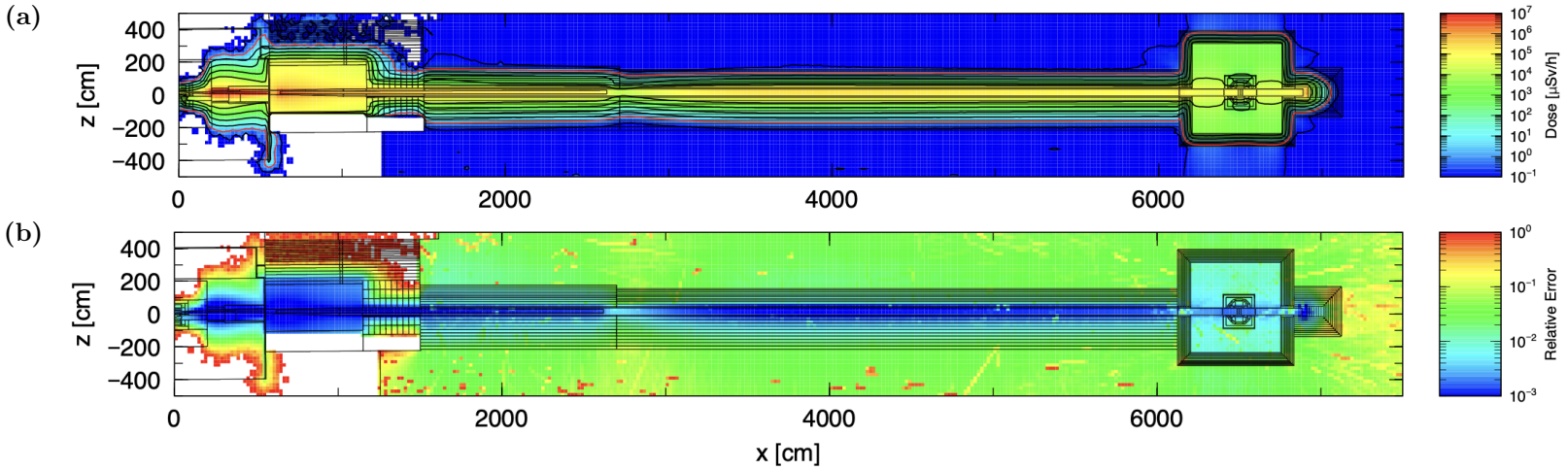

Figure 54: Panel (a): Photon dose rate in the xz-plane with the neutron source term. **Panel (b)**: Statistical uncertainty associated with Panel (a).

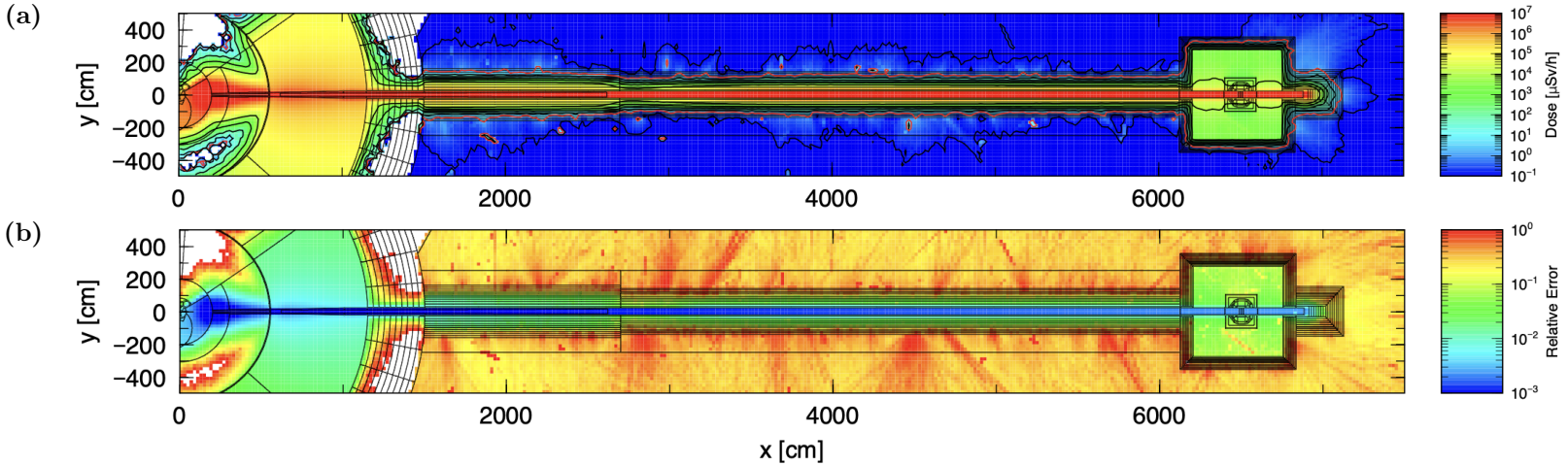

Figure 55: Panel (a): Neutron dose rate in the xy-plane with kernel density estimation. **Panel (b)**: Statistical uncertainty associated with Panel (a).

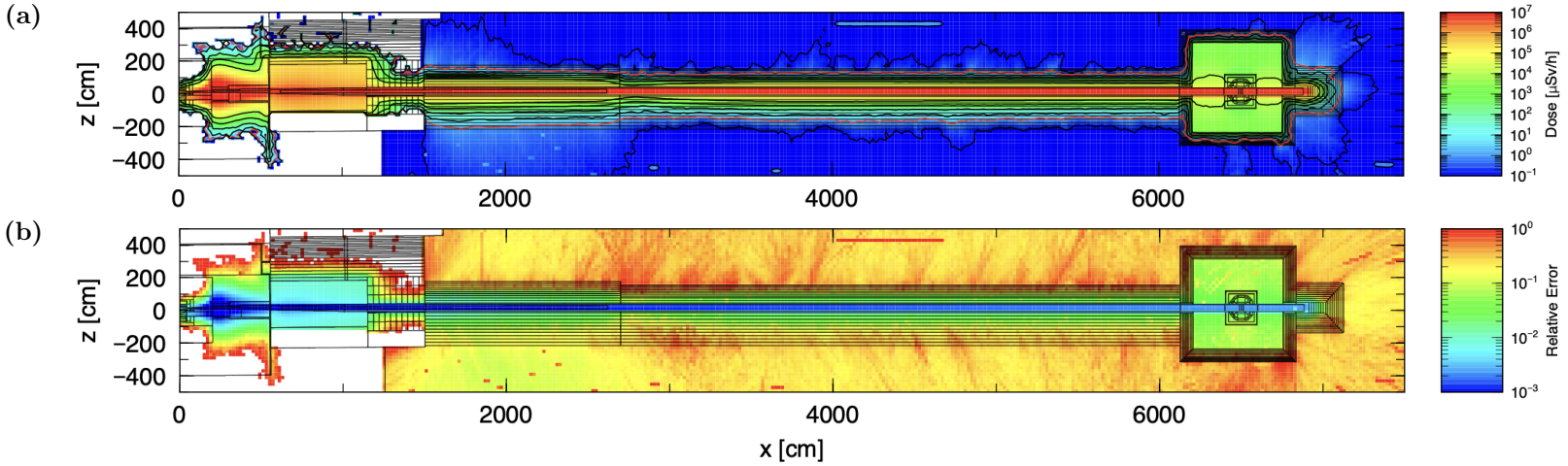

Figure 56: Panel (a): Neutron dose rate in the xz-plane with kernel density estimation. **Panel (b)**: Statistical uncertainty associated with Panel (a).

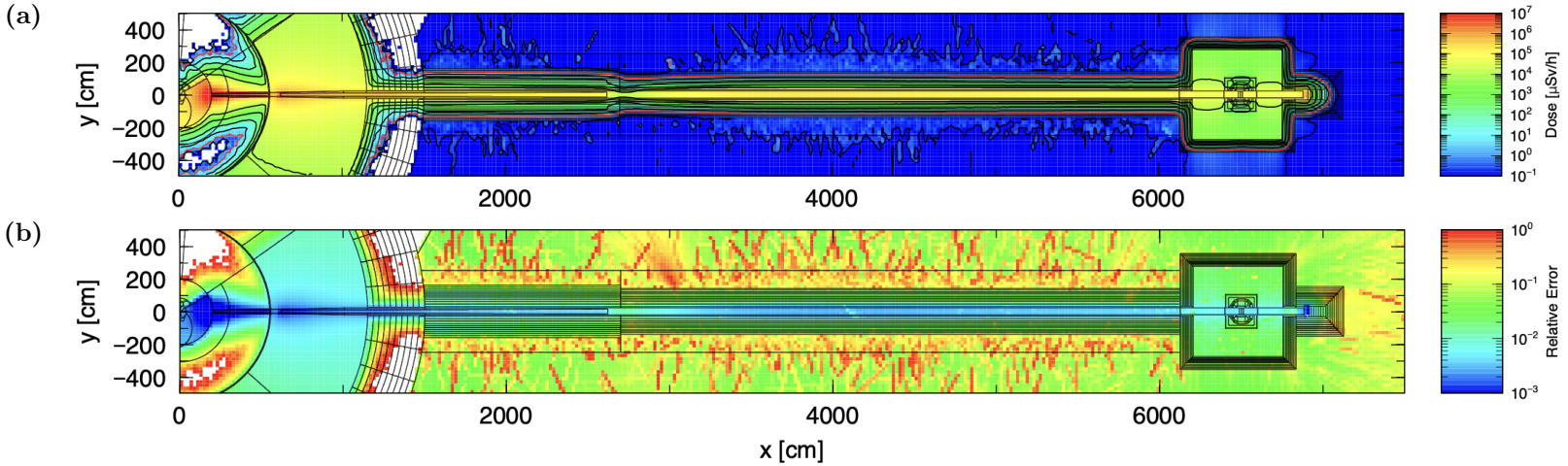

Figure 57: Panel (a): Photon dose rate in the xy-plane with kernel density estimation. **Panel (b)**: Statistical uncertainty associated with Panel (a).

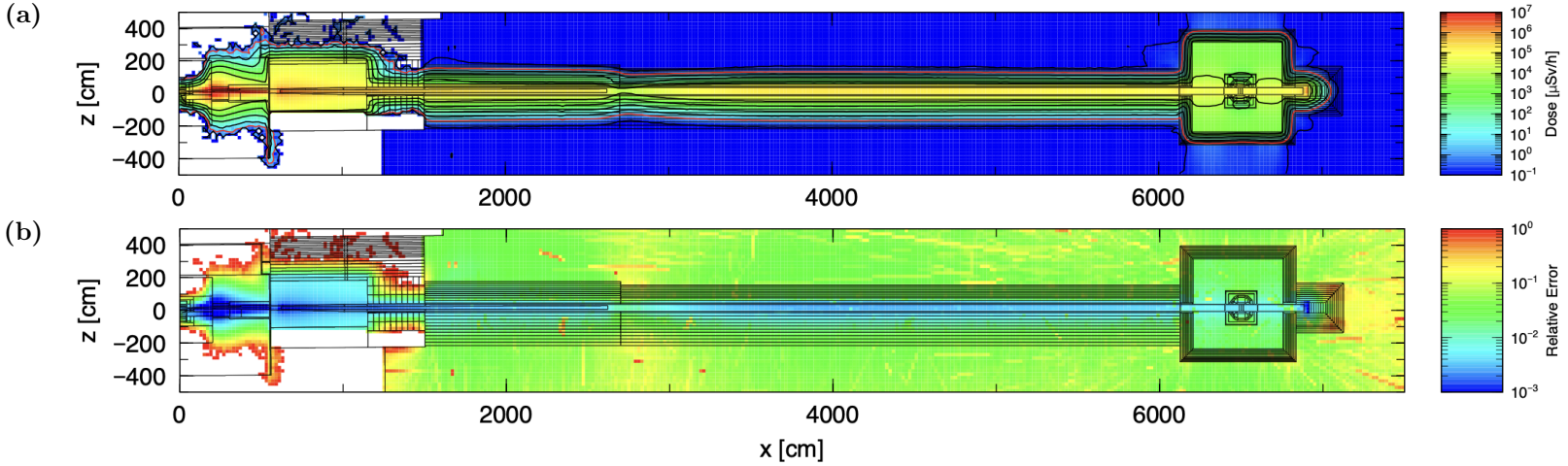

Figure 58: Panel (a): Photon dose rate in the xz-plane with kernel density estimation. **Panel (b)**: Statistical uncertainty associated with Panel (a).